Measurement of the Top Quark Mass using Dilepton Events and a Neutrino Weighting Algorithm with the DØ Experiment at the Tevatron (Run II)

Dissertation

zur

Erlangung des Doktorgrades (Dr. rer. nat.)

der

Mathematisch-Naturwissenschaftlichen Fakultät

der

Rheinischen Friedrichs-Wilhelms-Universität Bonn

vorgelegt von

Jörg Meyer

aus

Koblenz

Bonn 2007

Angefertigt mit Genehmigung der Mathematisch-Naturwissenschaftlichen Fakultät der Rheinischen Friedrich-Wilhelm-Universität Bonn

1. Referent: Prof. Dr. Norbert Wermes
2. Referent: Prof. Dr. Ian Brock

Angenommen am: 12.06.2007

I would like to thank Prof. Norbert Wermes for giving me the chance to work on a very exciting field of particle physics and for supporting and advising me. Thank you to Prof. Ian Brock for reviewing this thesis. Very special thanks to my two supervisors Arnulf Quadt and Christian Schwanenberger for helping me a lot and for a lot of fun. Many thanks to Akın Wingerter who has always been a good friend and who thought me many concepts of physics. Thank you to all friends, who studied physics together with me at Bonn University like Jong Soo Kim, Alexander Klitz, and Patrick Vaudrevange. I want to thank the whole (former) Bonn DØ group: Oleg Brandt, Volker Büscher, Tobias Golling, Marc Hohlfeld, Markus Klute, Su-Jung Park, Marc-André Pleier, Olav Mundal, Arnulf Quadt, Christian Schwanenberger, and Norbert Wermes. This thesis would not have been possible without this group and the great people and friends I met at Fermilab: Cano Ay, Philippe Calfayon, Jochen Cammin, Gabriele Garzoglie, Alexander Grohsjean, Petra Haefner, Hendrick Hoeth, Carsten Hensel, Matthias Kirsch, Thorsten Kuhl, Carsten Magass, Arnd Meyer, Björn Penning, Yvonne Peters, Thorsten Schliephake, Ingo Torchiani, Maren Vaupel, Peter Wagner, Gernot Weber, Daniel Wicke and many others.
Last but not least I would like to thank my parents for all the support during my studies, my sister Anja, and my girlfriend Julia Borissova for nice times without physics.

Contents

Chapter 1

Introduction

1.1 Motivation

Elementary particle physics raises questions that are several thousand years old. What are the fundamental components of matter and how do they interact? These questions are linked to the question of what happened in the very first moments after the creation of the universe. Modern physics systematically tests nature to find answers to these and other fundamental questions. Precise theories are developed that describe various phenomena and at the same time are reduced to a few basic principals of nature. Simplification and reduction have always been guiding concepts of physics. The interplay between experimental data and theoretical descriptions led to the Standard Model of elementary particle physics. It summarizes the laws of nature and is one of most precise descriptions of nature achieved by mankind.
Despite the great success of the Standard Model it is not the ultimate theory of everything. Models beyond the Standard Model try to unify all interactions in one grand unified theory. The number of free parameters is attempted to be reduced. Gravity is attempted to be incorporated. Extensions to the Standard Model like supersymmetry address the so-called hierarchy problem. Precision measurements are the key for searches of new particles and new physics.
A powerful tool of experimental particle physics are particle accelerators. They provide tests of the Standard Model at smallest scales. New particles are produced and their properties are investigated. In 1995 the heaviest known elementary particle, called top quark, has been discovered at Fermilab. It differs from all other lighter quarks due to the high mass and very short lifetime. This makes the top quark special and an interesting object to be studied. A rich program of top physics at Fermilab investigates whether the top quark is really the particle as described by the Standard Model. The top quark mass is a free parameter of the theory that has been measured precisely.
This thesis presents a precise measurement of the top quark mass by the DØ experiment at Fermilab in the dilepton final states. The comparison of the measured top quark masses in different final states allows an important consistency check of the Standard Model. Inconsistent results would be a clear hint of a misinterpretation of the analyzed

data set.
With the exception of the Higgs boson, all particles predicted by the Standard Model have been found. The search for the Higgs boson is one of the main focuses in high energy physics. The theory section will discuss the close relationship between the physics of the Higgs boson and the top quark.

1.2 Organization of the Thesis

In the following, an overview over the thesis is given with the contents of each chapter.

Chapter 2: Theoretical Aspects

This chapter briefly introduces the Standard Model of elementary particles. The physics of hadron collisions is described. Finally, the discovery of the top quark is discussed and measurements of properties of the top quarks are presented.

Chapter 3: The Experimental Setup

The top quark mass is measured with the DØ experiment. The accelerator facility at Fermilab and the DØ detector are described. The main sub-detectors are presented, and the performance is discussed.

Chapter 4: Event Simulation and Reconstruction

This chapter deals with the simulation and reconstruction of events at the DØ experiment. The different parts of the simulation are described and the chain of software reconstructions is detailed. A subsection focuses on the data reprocessing in 2005. The last part gives the identification criteria for the following physics objects: jets, electrons, muons, and missing transverse energy.

Chapter 5: Measurement of the Top Quark Mass

This is the main chapter presenting several top quark mass measurements in the dilepton final state. After presenting the event selections, the event kinematics of dilepton events is discussed. The so-called Neutrino Weighting method is introduced to extract the top quark mass. Several approaches of this method are presented and compared. DØ preliminary results of the top quark measurement are given. The results enter in the combined world average of the top quark mass.

Chapter 6: Conclusion

The conclusion summarizes the results and gives an outlook.

Chapter 2

Theoretical and Experimental Aspects

2.1 The Standard Model of Elementary Particles

The Standard Model (SM) [1–3] of elementary particles successfully describes fundamental particles and their interactions. It has been tested experimentally with high accuracy at scales down to $\sim 10^{-16}$ cm. With the exception of neutrino oscillations all observations so far are compatible with its predictions.
This section briefly summarizes the main components of the SM: the constituents of matter, the gauge interactions, and the Higgs mechanism [4, 5]. Details can be found in [6] and elsewhere.

Constituents of Matter. The constituents of matter are six leptons and six quarks. The leptons are the electron, muon, and tau, and their weak isospin partners electron neutrino, muon neutrino, and tau neutrino. The six quarks are the up, down, charm, strange, top, and bottom quark. They are grouped in three generations:

$$\text{Leptons:} \quad \begin{pmatrix} \nu_e \\ e \end{pmatrix} \quad \begin{pmatrix} \nu_\mu \\ \mu \end{pmatrix} \quad \begin{pmatrix} \nu_\tau \\ \tau \end{pmatrix}$$

$$\text{Quarks:} \quad \begin{pmatrix} u \\ d \end{pmatrix} \quad \begin{pmatrix} c \\ s \end{pmatrix} \quad \begin{pmatrix} t \\ b \end{pmatrix}$$

Each generation has an identical structure, i.e. particles of different generations have the same quantum numbers, but they differ in their mass. For each particle there is an antiparticle with the same properties, but reversed inner quantum numbers like electrical charge. Leptons and quarks are spin 1/2 particles, i.e. they are fermions.

Gauge Interactions. There are four fundamental interactions between particles, the strong, weak, electromagnetic, and the gravitational interaction. Gravity is not described by the SM, but due to its very weak coupling, its impact on elementary particles is

interaction	gauge bosons
electroweak	γ, W^+, W^-, Z
strong	8 gluons

Table 2.1: Fundamental interactions and their mediating gauge bosons.

negligible. The other interactions are described by gauge interactions. The gauge group is:

$$\mathrm{SU}(3)_C \times \mathrm{SU}(2)_L \times \mathrm{U}(1)_Y,$$

where the indices C, L, and Y refer to the color quantum number of quarks, the third isospin component of left-handed particles, and hypercharge, respectively. The electromagnetic and weak interaction are unified to the electroweak interaction. The interactions are mediated by gauge bosons with spin one. The strong interaction is mediated by eight massless gluons and the electroweak interaction is mediated by the massive W^+, W^-, and Z bosons and the massless photon. Gauge interactions are renormalizable [7], which allows to obtain finite answers from the theory for observables.

Higgs Mechanism. Local gauge symmetries introduce massless gauge bosons. However, experimentally it is known that the W^+, W^-, and Z bosons are massive. In the SM the mass is generated by spontaneously breaking the $\mathrm{SU(2)_L \times U(1)_Y}$ gauge group to the $\mathrm{U(1)_Q}$ group via the Higgs mechanism. Q denotes the electrical charge. The introduced Higgs field is a complex isodoublet field. After the spontaneous symmetry breaking, three of its degrees of freedom lead to masses of the W^+, W^-, and Z bosons, and one degree of freedom leads to the mass of the scalar Higgs boson, which has spin zero.
Fermions are endowed with mass by the Yukawa coupling to the Higgs ground state. The coupling is proportional to the fermion masses and hence strongest for the top quark.
The Higgs boson is the only particle predicted by the SM that has not been discovered, yet.

2.2 Hadron Collisions

Hadron colliders are built to achieve high center-of-mass energies. The degrees of freedom of perturbative QCD are quarks and gluons. Protons and anti-protons are described by the non-perturbative parton model. They consist of three valence-quarks, gluons, and sea-quarks. The hard interaction in a proton-anti-proton collision takes place between partons inside the proton and anti-proton. Each parton carries a momentum fraction x of the total momentum of the proton or anti-proton, respectively. x is called Bjorken x. If x_1 is the Bjorken x of the parton of a proton with energy-momentum p_1 and x_2 is the Bjorken x of the parton of an anti-proton with energy-momentum p_2, the center-of-mass energy of the parton interaction will be $\sqrt{\hat{s}} = \sqrt{(x_1 p_1 + x_2 p_2)^2}$. Figure 2.1 shows the

parton density distributions (PDF) for partons inside protons at a momentum transfer $Q^2 = (175\ \text{GeV})^2$ [1]. Hereby, $xf(x, Q^2)$ is the probability to find a parton with a momentum fraction in the range $x, x + dx$ inside the proton. The factorization theorem of QCD [8] allows to separate the long distance and short distance interactions. Long distance interactions below the factorization scale μ_F are described by PDFs while the short distance hard interactions with an energy scale above μ_F are calculated perturbatively. The production cross-section of a process $p\bar{p} \to X$ is given by a convolution of the PDFs and the parton cross section $\hat{\sigma}$:

$$\sigma(p\bar{p} \to X) = \sum_{i,j=q,\bar{q},g} \int dx_i dx_j f_{i,p}(x_i, \mu_F^2) f_{j,\bar{p}}(x_j, \mu_F^2) \cdot \hat{\sigma}_{i,j}(ij \to X; \hat{s}, \mu_F^2). \tag{2.1}$$

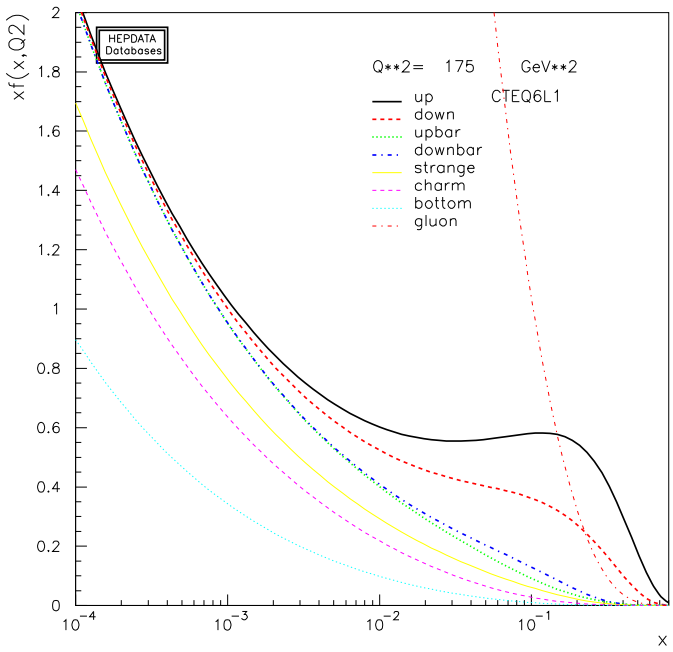

Figure 2.1: CTEQ6L1 parton density functions for up, down, charm, strange, bottom, anti-up, anti-down quarks, and gluons at $Q^2 = (175\ \text{GeV})^2$.

2.3 The Top Quark

The top quark is the heaviest known elementary particle. Due to its high mass top quarks have at present only been observed at the $p\bar{p}$ collider Tevatron. The first data taking period is called Run I and lasted from 1992 until 1996. During Run I the Tevatron was operating at a center-of-mass of 1.8 TeV. In 1995 the top quark was discovered by

[1] Throughout the thesis, natural units with $\hbar = c \equiv 1$ are used.

the CDF and DØ collaboration [9, 10]. The combined Run I result for the top quark mass is [11]:

$$m_{\text{top}} = 178.0 \pm 2.7(\text{stat.}) \pm 3.3(\text{syst.})\text{GeV}. \tag{2.2}$$

After Run I the accelerator and both experiments, CDF and DØ, were upgraded. In 2001 Run II started data taking at a center-of-mass energy of 1.96 TeV. One of the main goals of both experiments is a precise investigation and measurement of properties of top quarks. The results will confirm that the discovered particle is really the SM top quark or will give hints to new physics. At the beginning of 2007 about 1 fb^{-1} of Run II data are analyzed by each experiment. The next sections summarizes theoretical and experimental results on top quarks.

2.3.1 Top Quark Properties

The top quark is the isospin partner of the bottom quark. Its mass is a free parameter of the SM. In March 2007 the world average of the top quark mass is found to be [12]:

$$m_{\text{top}} = 170.9 \pm 1.1(\text{stat.}) \pm 1.5(\text{syst.})\text{GeV}. \tag{2.3}$$

It is about 35 times heavier than the bottom quark, which is the second heaviest quark. Due to the large mass, the top quark has a very short lifetime of:

$$\tau_{\text{top}} \approx 0.5 \times 10^{-24}\text{s}. \tag{2.4}$$

Therefore, top quarks decay before they can form bounded states in contrast to all lighter quarks. The hadronization takes place on a time scale given by $\Lambda^{-1}_{\text{QCD}} \approx (200\ \text{MeV})^{-1} \approx 3 \cdot 10^{-24}$ s that is larger than τ_{top}. The information on the top quark spin is conserved in the decay products of the top quark, i.e. it is the only quark that can be investigated as a "bare" quark.
According to the SM the top quark has electric charge $2e/3$. The DØ experiment excludes an exotic quark with electric charge $|q| = 4e/3$ at 92% C.L. using 370 pb^{-1} of collected data. The measurement is consistent with the expected electric charge of $|q| = 2e/3$ [13].
The Yukawa coupling of the top quark is about unity:

$$y_t = \sqrt{2}\frac{m_{\text{top}}}{v} \approx 1, \tag{2.5}$$

where $v = (\sqrt{2}G_F) = 246$ GeV is the vacuum-expectation value of the Higgs field that is fixed by the Fermi coupling G_F. Hence the high mass of the top quark seems quite natural. However, since all other quarks are much lighter this might be a hint that the top quark plays a fundamental role in the understanding of the electroweak symmetry breaking [14].

2.3.2 Top Quark Production

Top quarks can be produced in pairs via the strong and singly via the electroweak interaction. The production cross sections are of the same order, however, due to the final state signatures it is much more challenging to extract the electroweak single top signal out of the background than to extract strongly produced $t\bar{t}$ pairs.

Strong production Figure 2.2 shows the leading order Feynman diagrams for the $t\bar{t}$ pair production. At the Tevatron 85% of the $t\bar{t}$ pairs are produced by quark-antiquark annihilation and 15% are produced by gluon-fusion. The $t\bar{t}$ production cross section is

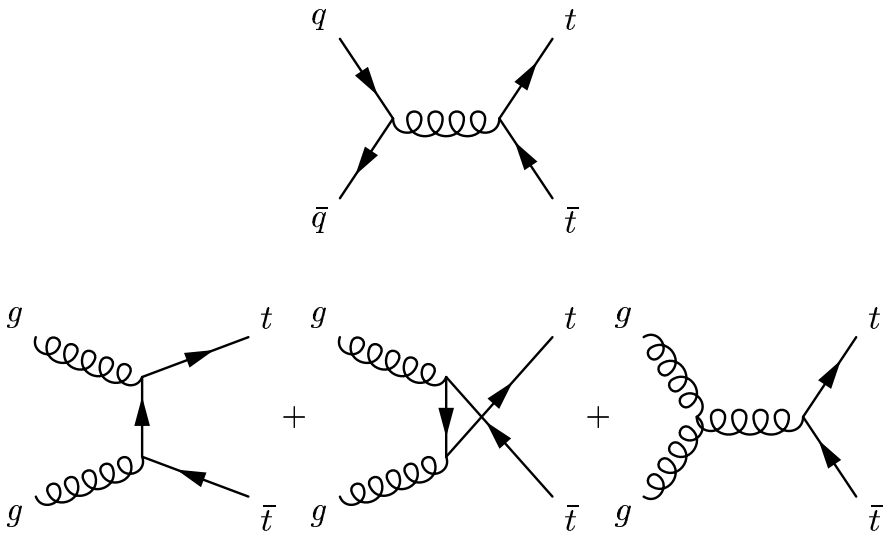

Figure 2.2: Leading order Feynman diagrams for top quark pair production via the strong interaction.

measured in various channels and different types of analyses. Figure 2.3 summarizes the results of DØ and CDF. The measurements are compared to the next-to-next-to-leading (NNLO) and next-to-next-to-next-to-leading-logarithmic (NNNLL) calculation [15, 16]:

$$\sigma^{\text{theo}}_{\text{toppair}}(p\bar{p} \to t\bar{t} + X) = 6.8^{+0.6}_{-0.5} \text{ pb}. \tag{2.6}$$

Electroweak production Evidence for the electroweak single top production was found by the DØ collaboration in December 2006. The measured single top production cross sections is [17]:

$$\sigma^{\text{measured}}_{\text{single top}}(p\bar{p} \to tb + X, tqb + X) = 4.9 \pm 1.4 \text{ pb}, \tag{2.7}$$

which is in good agreement with predictions calculated through next-to-next-to-next-to-leading order (NNNLO) at next-to-leading logarithmic (NLL) accuracy at $m_{top} =$

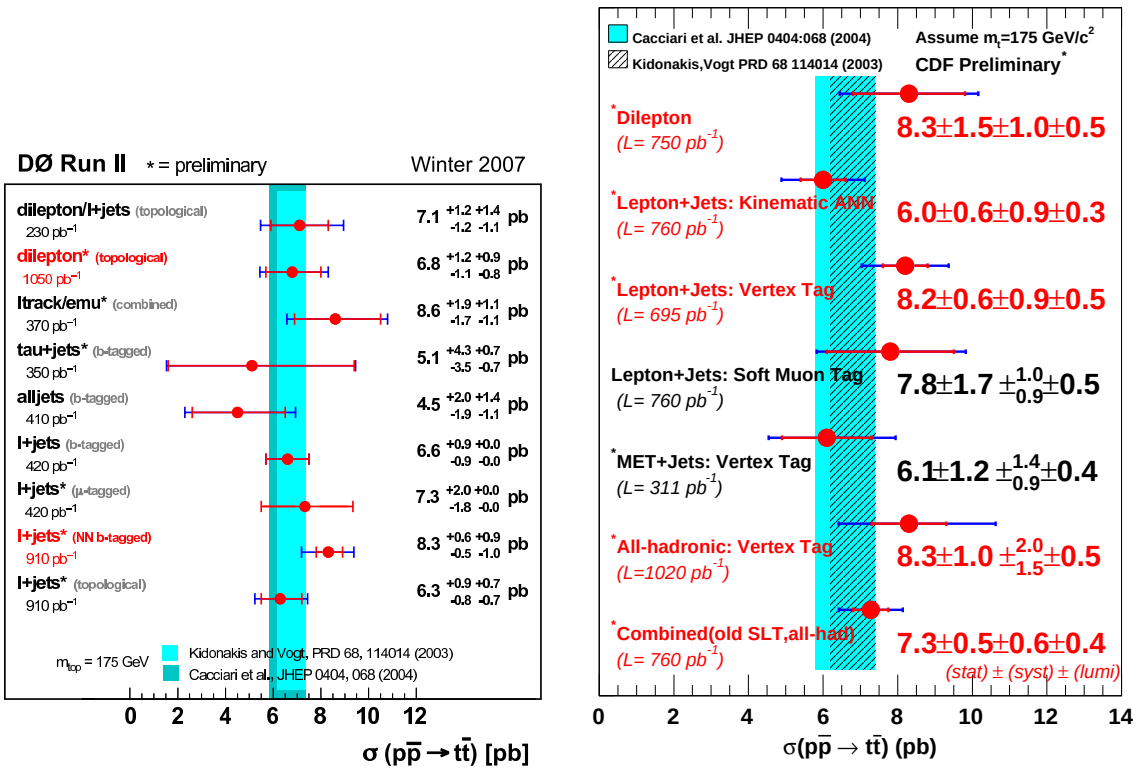

Figure 2.3: Results for the measurement of the $t\bar{t}$ cross section by the DØ (left) and CDF (right) experiment.

175 GeV
[18]:

$$\sigma^{\text{theo}}_{\text{single top}}(p\bar{p} \to tb + X, tqb + X) = 3.21 \pm 0.21 \text{ pb}. \tag{2.8}$$

2.3.3 Top Quark Decay

The leading order Feynman diagram for the top quark decay is shown in Figure 2.4. The CKM matrix element V_{tb} occurs as a factor at the decay vertex. Top quarks decay to almost 100% to a W boson and a b quark. This is due to the fact that V_{tb} is very close to unity [19]:

$$V_{tb} = 0.999100^{+0.000034}_{-0.000004}. \tag{2.9}$$

V_{tb} has been determined indirectly using unitary constraints of the CKM matrix. The first direct measurement of V_{tb} without making assumptions on the CKM matrix unitary and the number of quark families finds [17]:

$$0.68 < |V_{tb}| \leq 1 \quad \text{at } 95\% \text{ C.L.} \tag{2.10}$$

The final state of top pair events are determined by the decay modes of the two W

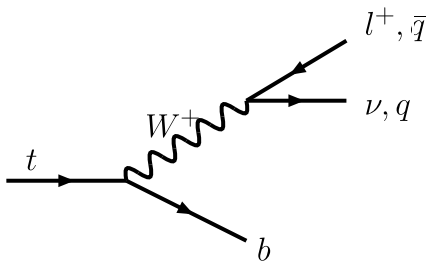

Figure 2.4: Leading order Feynman diagram of the top quark decay.

bosons. If both W bosons decay hadronically the final state is called "all jets"channel, if one W boson decays leptonically it is called "lepton + jets" channel, and if both W bosons decay leptonically it is called "dilepton" channel. Figure 2.5 gives the theoretical branching ratios of all final states of $t\bar{t}$ decays. The all jets channel has the highest branching ratio, but it has the disadvantage of a high background originating from multi-jet production. The dilepton channel has a small branching ratio, but a very clean signature with two isolated leptons with high transverse momentum. The lepton + jets channel is in between with a medium branching ratio and with a clear signature. The main background of the lepton + jets channel comes from W boson production associated with jets. Throughout this thesis the term dilepton channel will only include the $e\mu$, ee, and $\mu\mu$ channels. These channels include leptonically decaying τ leptons, while hadronically decaying τ leptons are not considered.

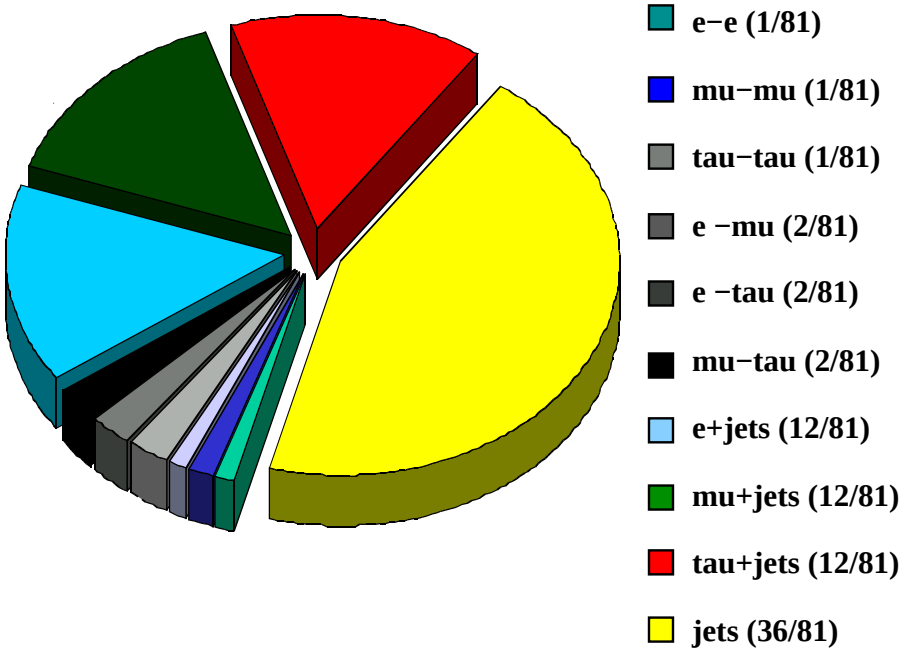

Figure 2.5: All decay channels and theoretical branching rations of $t\bar{t}$ pairs.

2.3.4 Top Quarks in Radiative Corrections

Virtual top quarks significantly contribute to many radiative corrections within the SM and in models beyond the SM. Figure 2.6 shows Feynman diagrams for the one loop corrections to the W boson mass. It is given by [20]:

$$M_W^2 = \frac{\frac{\pi\alpha}{\sqrt{2}G_F}}{s_W^2(1-\Delta r)}, \tag{2.11}$$

where Δr contains a correction depending on m_{top}:

$$(\Delta r)_{\text{top}} \approx -\frac{3G_F m_{\text{top}}^2}{8\sqrt{2}\pi^2 \tan^2\theta_W}, \tag{2.12}$$

and a correction depending on the Higgs boson mass, M_H:

$$(\Delta r)_{\text{Higgs}} \approx \frac{11 G_F M_Z^2 \cos^2\theta_W}{24\sqrt{2}\pi^2} \ln\frac{M_H^2}{M_Z^2}. \tag{2.13}$$

Figure 2.6: One-loop corrections for the W boson mass.

The dependence on m_{top} is quadratic while the dependence on M_H is only logarithmic. The top quark mass has been predicted as a function of a Higgs mass hypothesis with the help of precision measurements of the W boson mass and the electroweak mixing angle $\sin\theta_W$, as all quantities are related via loop corrections. Figure 2.7 shows fits of the top quark mass to electroweak data [21]. The indirect measurements are in good agreement with the direct measurements of m_{top}. Using the direct measurement of m_{top} as input, the Higgs boson mass can be predicted. Figure 2.8 shows the top quark mass versus the W boson mass [22]. The center of the dashed ellipse indicates the direct measurements of m_{top} and m_W. The dashed ellipse marks the uncertainties of the measurements. The solid curve shows the results of indirect measurements. The Higgs boson mass is constant along the diagonal lines. Higgs boson masses below 114.4 GeV are excluded at 95% C.L. by the LEP experiments [23]. There is no overlap between the ellipse and the diagonal lines, which restricts the range for SM Higgs masses. Further reductions of the uncertainties on the top quark mass and the W boson mass will provide better constraints to the SM and better predictions of the Higgs boson mass.

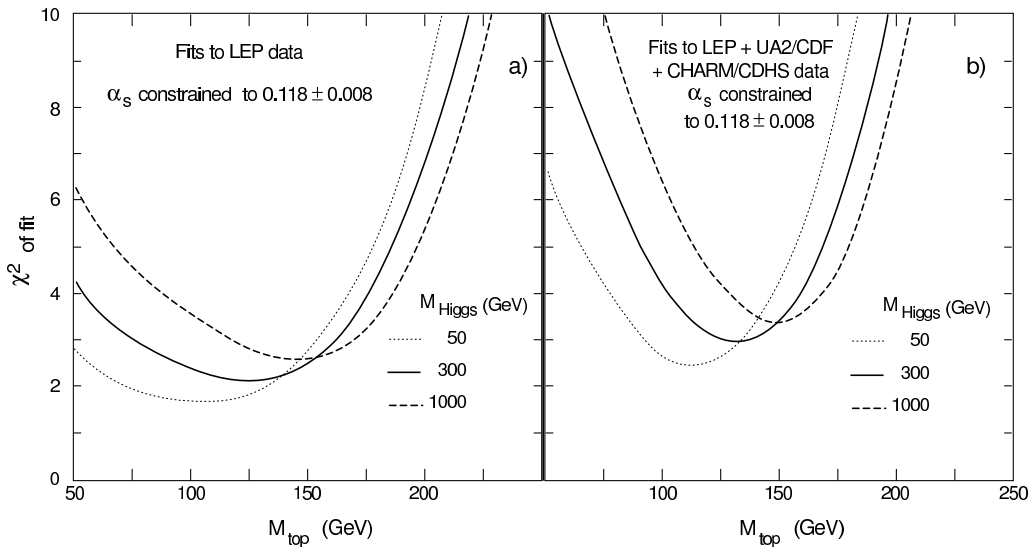

Figure 2.7: χ^2 of the fit to electroweak precision data vs. m_{top} for different Higgs boson masses. The minima are indirect measurements of m_{top} [21].

2.3.5 Top Quarks in Models beyond the SM

Models beyond the SM provide additional motivation for precise measurements of the top quark properties. One candidate for extensions of the SM is Supersymmetry [24]. At present, no evidence that nature is supersymmetric on the electroweak scale is found. However, signatures of the $t\bar{t}$ production could also arise from supersymmetric scenarios. In such scenarios, the pure SM interpretation of the data would lead to a slightly enlarged production cross section and different top quark masses for the different top decay channels [25].
Independent measurements of the top quark mass for each decay channel test the consistency of the SM and provide limits or hints for new physics beyond the SM.

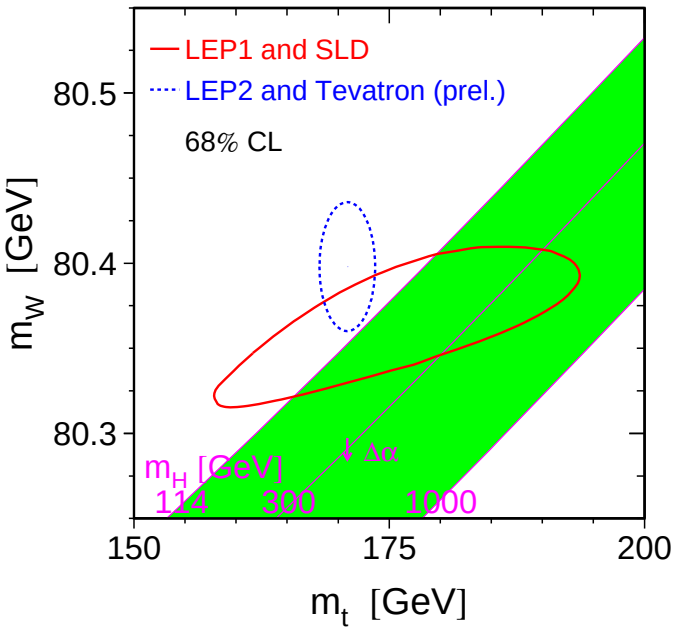

Figure 2.8: Top quark mass versus W boson mass with lines of constant Higgs boson mass. The dashed ellipse shows the results of direct measurements and the solid curve indirect measurements [22].

Chapter 3

The Experimental Setup

The Tevatron located at Fermilab in Batavia, Illinois is the highest-energy hadron collider to date[1]. Protons and antiprotons collide at two interaction points at the centers of the two experiments CDF and DØ. During Run I (1992-1996) both experiments, CDF and DØ, collected about 125 pb^{-1} of data each. After Run I the center-of-mass energy of the Tevatron was increased from 1.8 TeV to 1.96 TeV. In addition, the instantaneous luminosity was increased and both experiments were fundamentally upgraded. In March 2001 Run II started operating.
This chapter gives an overview of the Fermilab accelerator facility and the DØ experiment.

3.1 The Tevatron

The proton and antiproton beams are produced and then accelerated in a series of several accelerators. Figure 3.1 shows a sketch of the Tevatron and its pre-accelerators. A detailed description can be found in [26].

H^- ions with an energy of 18 keV are used as source of protons. They are accelerated in an electrostatic field of a Cockcroft-Walton pre-accelerator to an energy of 750 keV. The energy of the ions is further increased to 400 MeV by the Fermilab Linac, a linear accelerator with a length of 146 meters. Energies of several hundred MeV can only be reached by alternating radiofrequency fields and not by electrostatic fields. The next stage of acceleration is the Booster, a small synchrotron. Before the injection the electrons of the H^- ions are stripped off, i.e. the Booster accelerates the remaining protons. After reaching an energy of 8 GeV the protons are injected in the Main Injector, a larger synchrotron, where the protons are further accelerated to an energy of 150 GeV before they are injected in the Tevatron. The Tevatron has a radius of one kilometer. The proton and antiproton beam share the same beam pipe. They reach an energy of 980 GeV. There are twenty-four electrostatic separators along the ring so that $p\bar{p}$ collisions take only place at the CDF and DØ experiment.

[1]This will be true until the Large Hadron Collider at CERN will start operating at a center-of-mass energy of $\sqrt{s} = 14$ TeV beginning of 2008.

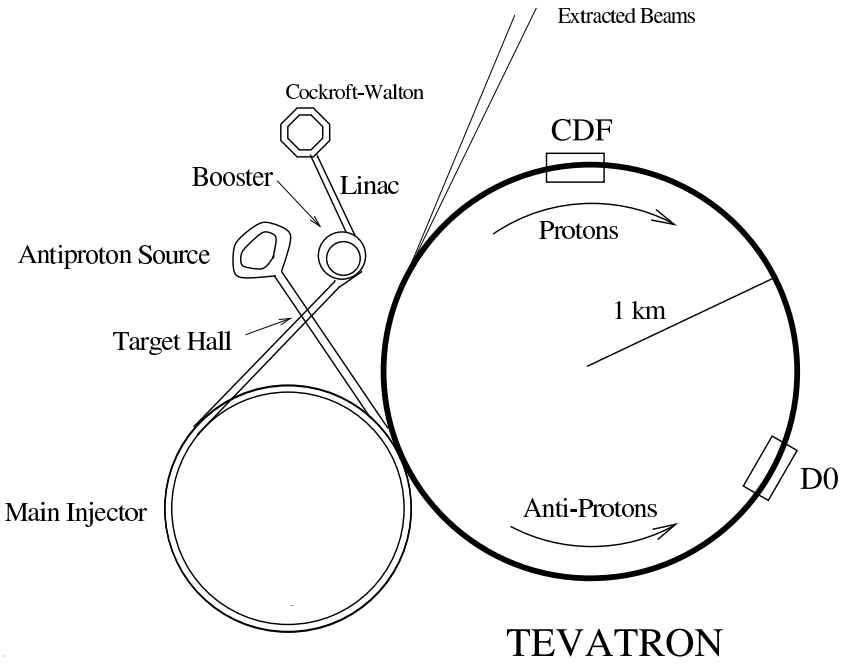

Figure 3.1: The Fermilab accelerator complex and the position of the two experiments CDF and DØ.

Antiprotons first have to be produced and condensed. They are produced in collisions of 120 GeV protons delivered by the Main Injector as described before, and a nickel target. Antiprotons are produced at a rate of 1-2 per 100, 000 collisions. A lithium collection lens focuses them and a pulsed dipole field separates them from other produced particles. In the Debuncher ring the transverse momenta of the antiprotons are reduced by stochastic cooling before they are stored in the Accumulator or Recycler ring. The Recycler ring is a second storage ring located below the Main Injector. In October 2005, electron cooling for the antiprotons was added to the Recycler. The antiprotons are accelerated in the Main Injector and injected in the Tevatron, the same way as the protons. Figure 3.2 shows the peak luminosity of the Tevatron as a function of time. Several upgrades led to higher and higher instantaneous luminosities.

3.2 The DØ Detector

The DØ detector is a multi-purpose detector consisting of several sub-systems. It is designed for the precise reconstruction of high energetic charged leptons, jets, and missing transverse energy produced in $p\bar{p}$ collisions. A detailed description of all components of the Run II DØ detector can be found in [28].
DØ uses a right-handed coordinate system with the z-axis along the proton-beam axis. Typically, the radius r and the polar angle φ in the transverse plane, and the pseudo-rapidity η are used to specify a three-dimensional space point. The relations to Cartesian

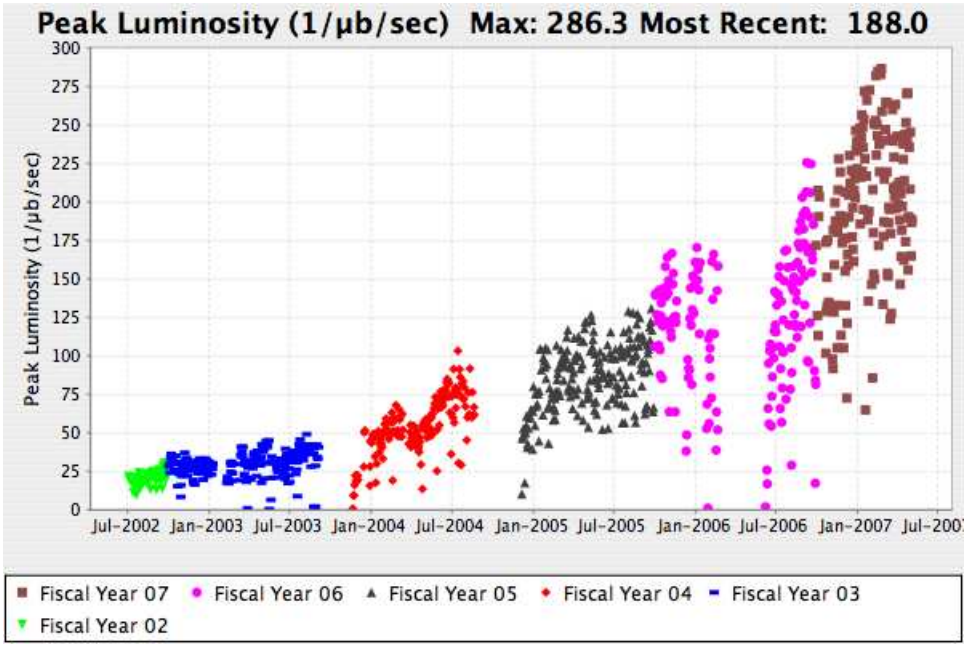

Figure 3.2: Peak luminosity of the Tevatron from July 2002 until June 2007 [27].

coordinates (x, y, z) are given by:

$$r = \sqrt{x^2 + y^2} \tag{3.1}$$

$$\varphi = \arctan \frac{y}{x}, \quad \varphi \in [0, 2\pi), \tag{3.2}$$

$$\eta = -\ln \tan \frac{\theta}{2}, \quad \theta = \arctan \frac{r}{z}, \tag{3.3}$$

where θ denotes the azimuthal angle to the z-axis. In the limit of massless particles or high energies $\frac{m}{E} \to 0$ the pseudo-rapidity equals the rapidity y defined as:

$$y = \frac{1}{2} \ln \frac{E + p_z}{E - p_z}. \tag{3.4}$$

Rapidity distributions $\frac{dN}{dy}$ are invariant under Lorentz transformations along the z-axis. The production rate of high energetic particles by the stong interaction is roughly constant as a function of η. Pseudo-rapidity coordinates are given with respect to the position of the primary vertex of an event. The η coordinate with respect to the detector center is referred to as "detector η", in contrast to the true η taken from the actual collision point. The region with high pseudo-rapidity coordinates ($|\eta| \gtrsim 2$) is called forward region. Cone sizes and spatial matching sizes ΔR are defined as $\Delta R = \sqrt{\Delta\eta^2 + \Delta\varphi^2}$ or as $\Delta R = \sqrt{\Delta y^2 + \Delta\varphi^2}$ in case of the jet reconstruction algorithm.
Figure 3.3 shows a cross-sectional view of the DØ detector. The central tracking system is displayed in Figure 3.4. The following sections describe the main components of the DØ detector.

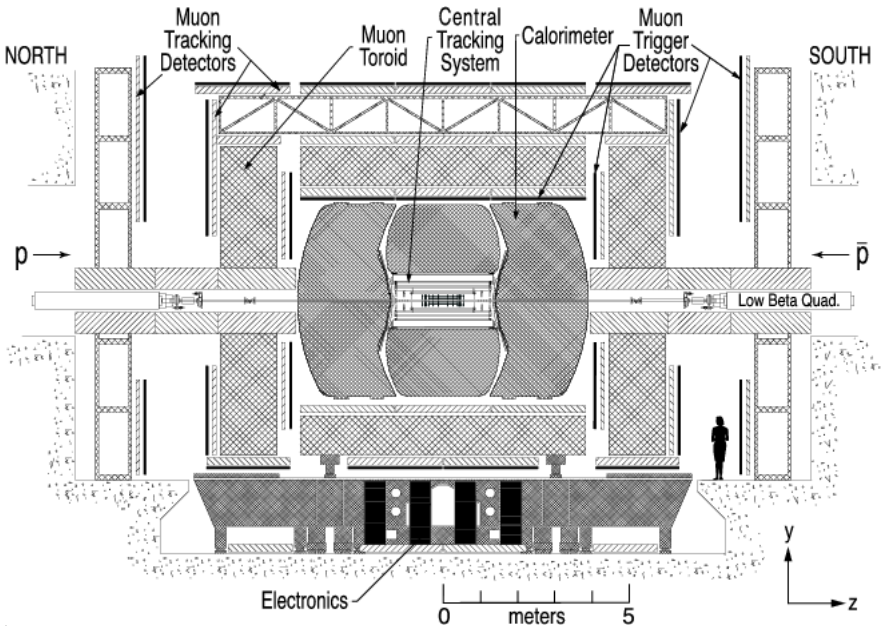

Figure 3.3: Cross-sectional view of the DØ detector from inside the Tevatron ring.

3.2.1 Inner Tracking System

In the central tracking system tracks of charged particles are reconstructed. The tracks are bent in a two Tesla solenoidal field allowing measurements of transverse momenta

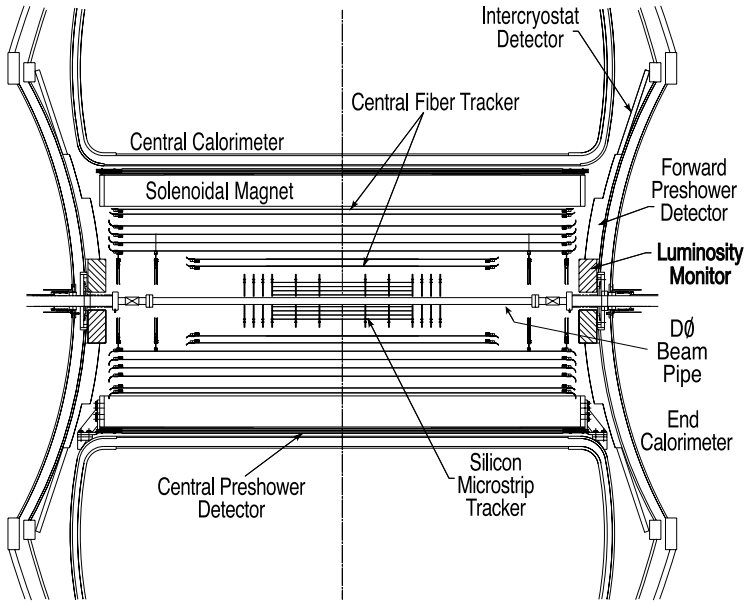

Figure 3.4: Cross-sectional view of the central tracking system.

p_T. The innermost detector is the silicon microstrip tracker (SMT). It surrounds the beryllium beam pipe that has an outer diameter of 38.1 mm. Between SMT and the solenoid there is the central fiber tracker (CFT) consisting of scintillation fibers.
The resolution of the z-coordinate of the primary vertex is about 35 μm. The impact parameter resolution in the transverse $r-\phi$-plane is better than 15 μm for central tracks ($\eta = 0$) with a transverse momentum larger than 10 GeV.

Silicon Microstrip Tracker. The SMT provides high resolution reconstructions of tracks and vertices. A hybrid design consisting of barrel detectors and disks is chosen to cover a large $|\eta|$ range up to about 3. The SMT measures three dimensional space points of charged tracks. The barrel detectors primarily measure $r-\varphi$ coordinates of vertices and low η tracks. The disk detectors measure the $r-z$ and $r-\varphi$ coordinates of vertices and forward tracks with high η. Figure 3.5 shows the SMT design. There are six barrels in the central region. Each barrel has four silicon readout layers. A silicon module of the barrel detectors is called ladder. Layer one and two consist of twelve ladders each, while layers three and four consist of 24 ladders each. In total there are 432 ladders. The barrels are interleaved with disk detectors. The disk separation must be kept small to minimize extrapolation uncertainties, however, each disk represents a geometrical acceptance gap of about 8 mm between the barrels. There are twelve disks called F-disks and four external large diameter disks called H-disks. F-disks consist of twelve double-sided wedge detectors. Altogether, the SMT has 912 readout modules with 792, 576 channels. The main readout chip is the SVXIIe chip.

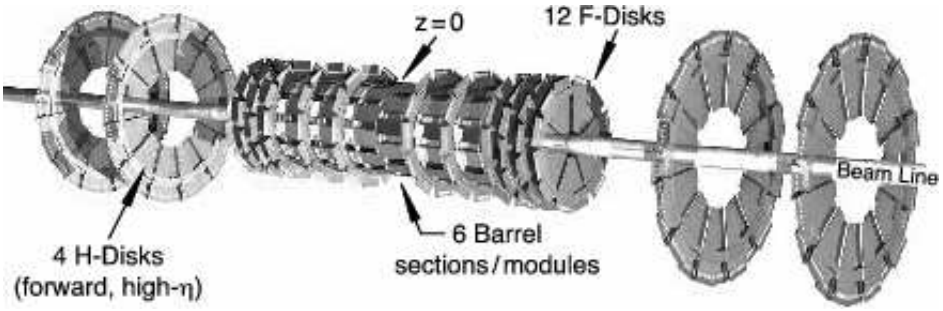

Figure 3.5: Schematic view of the barrels and disks of the SMT.

During an upgrade in April 2006 a new inner layer of the SMT was installed. It is called layer 0 and consists of 48 silicon sensors mounted on 6 facets on a 1.68 m long, 1.6 cm radius carbon fiber support structure. Layer 0 improves the impact parameter resolution by about a factor of two. The data analyzed in this thesis are taken before this upgrade. Details on the new silicon layer can be found in [29].

Central Fiber Tracker. The CFT consists of scintillating fibers mounted on eight concentric support cylinders. The radii of the cylinders are in the range 20 cm to 52 cm. The fiber length of the two innermost cylinders is 1.66 m, the other cylinders have a

fiber length of 2.52 m. A range of $|\eta| \lesssim 1.7$ is covered by the outer cylinders. Each of the eight cylinders supports two double layers of fibers. The first double layer is an axial layer with fibers parallel to the z-axis. The second double layer is a stereo layer with an stereo angle of $+3°$ or $-3°$. A picture of a double layer of fibers can be seen in Figure 3.6.

Charged particles traversing the scintillating fibers produce light. The ends of the

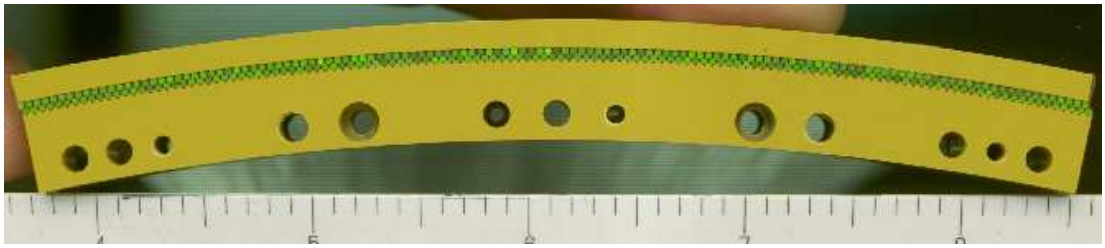

Figure 3.6: Picture of a double layer of scintillating fibers of the CFT.

fibers are coupled to clear fiber wave guides that carry the light to visible light photon counters (VLPC). The wave guides have a length of $7.8 - 11.9$ m.
The scintillating fibers have a diameter of 835 μm including two different claddings each of size 25 μm. The spacing between the centers of two adjacent fibers varies between $928 - 993$ μm. This will leads to an inherent double layer resolution of about 100 μm, if the location of the fibers is known with a precision better than 50 μm.
The fibers are made of polystyrene which is doped with organic fluorescent dye paraterphenyl and which contains a low concentration of 3-hydroxyflavone. The paraterphenyl emits light with a wavelength of $\approx$ 340 nm. The 3-hydroxyflavone absorbs it and re-emits green light with a wavelength of 530 nm, which can be transmitted through the polystyrene. The VLPCs transform the light signal into an electrical signal. They are impurity-band silicon avalanche photodetectors with the capability to detect single photons. The VLPCs are inside a liquid helium cryostat at a temperature of 9.00 ± 0.05 K to operate at a noise rate of less than 0.1%. They have a quantum efficiency of $\geq 75\%$ and a high gain of $22,000 - 65,000$. The bias voltage is in the range $6 - 8$ V.

Solenoidal Magnet. SMT and CFT are inside a homogeneous 2.0 T magnetic field of a superconducting solenoidal magnet. The solenoid has a length of 2.73 m and a diameter of 1.42 m. The current is 4749 A and the total stored energy is 5.3 MJ. The radiation length of the material of the solenoid is 0.87 X_0 at $\eta = 0$. After a shutdown in fall 2004 the solenoid failed to reach the full operation current. In order to stably operate the current was reduced to 4550 A, which corresponds to a magnetic field of 1.92 T.

3.2.2 Preshower Detector

Central Preshower Detector. The central preshower detector (CPS) is attached outside of the solenoid magnet in a 5 cm gap to the calorimeter. Its purpose is to detect showers starting in the material in front of the calorimeter, i.e. the tracking system, the solenoid, and support structures. This information helps identifying electrons offline and at trigger time, and to correct calorimeter shower energies. The radius of the CPS is between $71.8 - 74.2$ cm, the pseudorapidity is in the range $|\eta| < 1.3$. It consists of three layers of triangular strips of scintillators. As for the CFT the scintillator light is guided to VLPCs via clear fibers. Between the solenoidal magnet and the CPS scintillators there is a lead radiator of thickness 0.56 cm with a radiation length of 1 X_0. The first CPS layer is axial, while the second and third layer have a stereo angle.

Forward Preshower Detector. The forward preshower detector (FPD) is made of scintillator strips. There are two layers in front of and behind a lead-stainless-steel absorber. The first two layers cover the region $1.65 < |\eta| < 2.5$. The layers behind the absorber cover $1.5 < |\eta| < 2.5$. The absorber is $2X_0$ thick and causes the evolution of showers. The scintillation light is guided to VLPCs similar to the CPS.

3.2.3 Calorimetry

In the calorimeter photons, electrons, and jets are identified and their energies are measured. The DØ detector consists of three so-called liquid argon sampling calorimeters, the central calorimeter (CC), and two end cap calorimeters (EC). The CC covers a region up to $|\eta| \lesssim 1$ and the EC extends the coverage up to $|\eta| \approx 4$. Figure 3.7 is an isometric view of the three calorimeters. The innermost part is the electromagnetic calorimeter (ECal). Around the ECal there is the hadronic calorimeter (HCal) with the fine hadronic section and the coarse hadronic section. Figure 3.9 shows a scheme of a quarter of the calorimeter highlighting the transverse and longitudinal segmentation. The shading pattern indicates groups of cells combined together for signal readout. The CC and each of the two ECs are inside their own cryostat filled with liquid argon with a temperature of about 90 K. The argon acts as active material of the sampling calorimeter. The ECal uses 3 mm and 4 mm thick absorber plates made of depleted uranium. The absorber plates in the fine hadronic section of the HCal are 6 mm thick and also made of uranium, but with an 2% alloy of niobium. The coarse hadronic section uses copper in the CC and stainless steel in the EC as absorber material. The plates are 46.5 mm thick. The smallest unit of the calorimeter is a cell consisting of an absorber plate and the active liquid argon gap as shown in Figure 3.8. Electromagnetic and hadronic showers evolve in the calorimeter and deposit their energy. Ionization of charged particles is collected in an electrical field produced by a voltage of typically 2 kV between the passive metal plates and the signal boards. The granularity of the calorimeter in $\Delta\eta \times \Delta\varphi$ is $0.1 \times 2\pi/64 \approx 0.1 \times 0.1$. The Ecal consists of four layers in the CC and EC. It was designed under the assumption that the shower maximum of electromagnetic showers are located at the third layer, which has a finer granularity

of 0.05×0.05. In the CC the layers are approximately 1.4, 2.0, 6.8, and 9.8 X_0 thick, and in the EC they are approximately 1.6, 2.6, 7.9, and 9.3 X_0 thick. In total the calorimeter has $55,000$ readout channels.
In the region between CC and EC there is the intercryostat detector (ICD). It recovers reconstruction inefficiencies caused by the gap between the calorimeters. The ICD is attached to the exterior surfaces of the end cryostats and covers the region between $1.1 < |\eta| < 1.4$. It consists of scintillating tiles divided in subtiles enclosed in aluminum boxes. The subtiles are of size 0.1×0.1 in $\Delta\eta \times \Delta\varphi$. Clear fibers guide the scintillator light to photomultiplier tubes. The intercryostat detector has 378 readout channels.

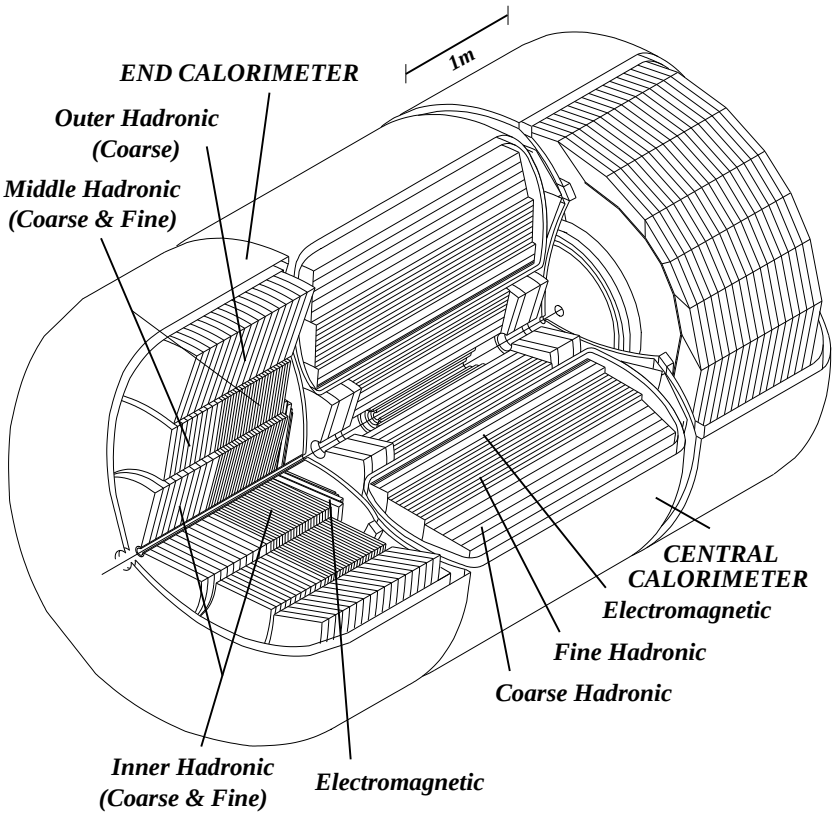

Figure 3.7: Isometric view of the central and two end calorimeters.

The resolution of the calorimeter has been measured with test beam data. Equation 3.5 gives the parametrization of the calorimeter resolution. The results from the electron and pion test beam are listed in Table 3.2.3 [30, 31]. The resolution of the calorimeter degraded in Run II compared to Run I due to the increased material in front of the calorimeter.

$$\frac{\Delta E}{E} = C \oplus \frac{S}{\sqrt{E}} \oplus \frac{N}{E} \tag{3.5}$$

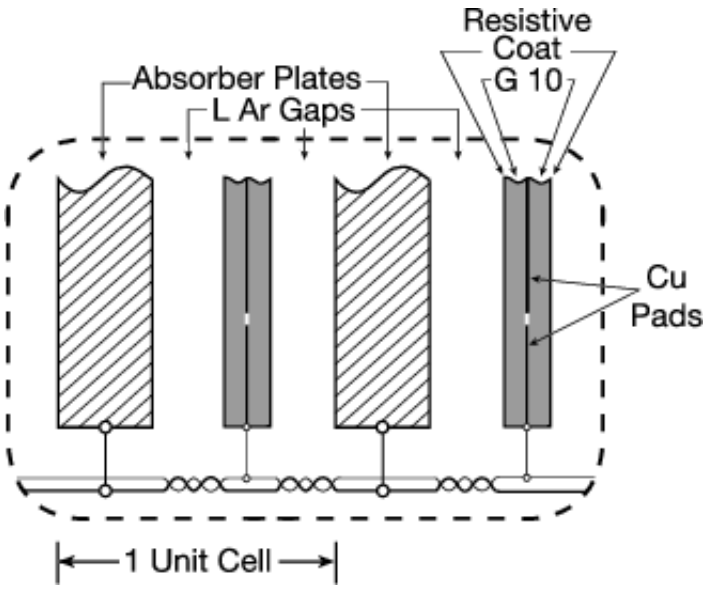

Figure 3.8: Schematic view of a calorimeter cell.

	C	S	N
e	$0.0115^{+0.0027}_{-0.0036}$	$0.135 \pm 0.005\sqrt{\text{GeV}}$	0.43 GeV
π	0.032 ± 0.004	$0.45 \pm 0.04\ \sqrt{\text{GeV}}$	0.975 GeV

Table 3.1: Parameters of the calorimeter resolution.

3.2.4 Muon System

The outer-most subdetector is the muon system. Muons are the only charged particles reaching the muon system, because electrons, photons, and hadrons cannot pass through the calorimeter. The central muon system detects muons up to $|\eta| \approx 1$. The forward muon system covers the region up to $|\eta| < 2$. There are three layers (A, B, and C) of drift tubes, as can be seen in the exploded view in Figure 3.10. The drift tubes in the central region are called Proportional Drift Tubes (PDTs). They were already used in Run I. PDTs have a size of 2.8×5.6 m^2. A single drift cell is of size 10.1×5.5 cm^2. The innermost A-layer consists of four decks, while the B- and C-layer consist only of three decks. The drift tubes in the forward muon system are smaller and therefore called Mini Drift Tubes (MDTs). A MDT consists of eight cells each of size 9.4×9.4 mm^2. In total, there are 6624 PDTs and 6080 MDTs. In addition to the drift tubes there are scintillation counters in each layer. The fast scintillators are used for Level 1 triggering, to reject cosmic muons, and to associate drift tube hits to the appropriate bunch crossing. There are 630 counters in the central and 4214 counters in the forward region. The scintillator light is detected by photomultiplier tubes.
Between the A- and B-layer, there is toroidal magnet at a distance of 317.5 cm from

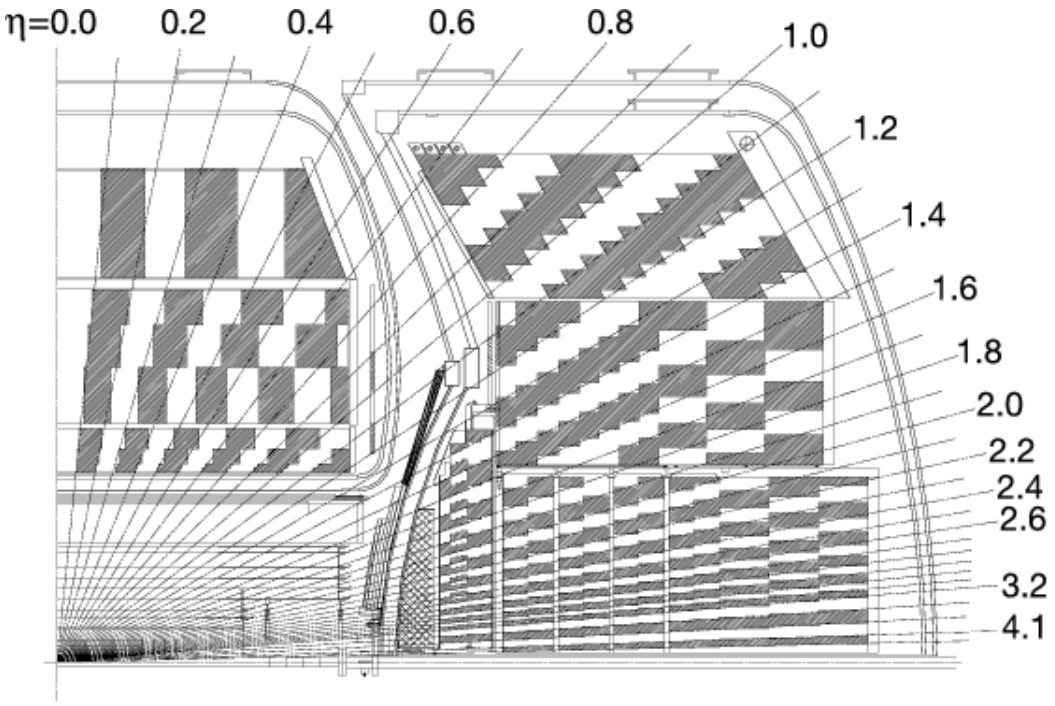

Figure 3.9: View of a quarter of the calorimeter showing the transverse and longitudinal segmentation.

the beam axis. A current of 1500 A generates a magnetic field of about 1.8 T. The toroidal field allows a stand-alone momentum measurement for muons. This improves the matching of muon tracks to central tracks and increases the momentum resolution of high p_T muons. The transverse momentum resolution of a muon with $p_T = 40$ GeV, with SMT hits, and with a detector $\eta < 1.6$ is measured to be $\Delta p_T/p_T = 9.6 \pm 0.3\%$. After the shutdown in fall 2004, the resolution degraded due to the reduced solenoid field. It is found to be $\Delta p_T/p_T = 11.0 \pm 0.3\%$ [32].

3.2.5 Luminosity Monitor

The Luminosity Monitor (LM) measures the average number of inelastic $p\bar{p}$ collisions $\tilde{N}_{LM}$ in the pseudo-rapidity range $2.7 < |\eta| < 4.4$. The instantaneous luminosity $\mathcal{L}$ is given by $\mathcal{L} = \frac{f\tilde{N}_{LM}}{\sigma_{LM}}$, where f is the beam crossing frequency, and σ_{LM} is the effective cross section including acceptance and efficiency of the LM. The average $\mathcal{L}$ is determined for each data taking time of about 60 s, called luminosity block. $\mathcal{L}$ is effectively constant for each luminosity block. The LM consists of plastic scintillation counters located at $z = \pm 140$ cm, as shown in Figure 3.4 and 3.11. Photomultipliers detect the scintillator light. The LM also allows to monitor the beam halo, and to measure the z-position of the interaction vertex very fast.

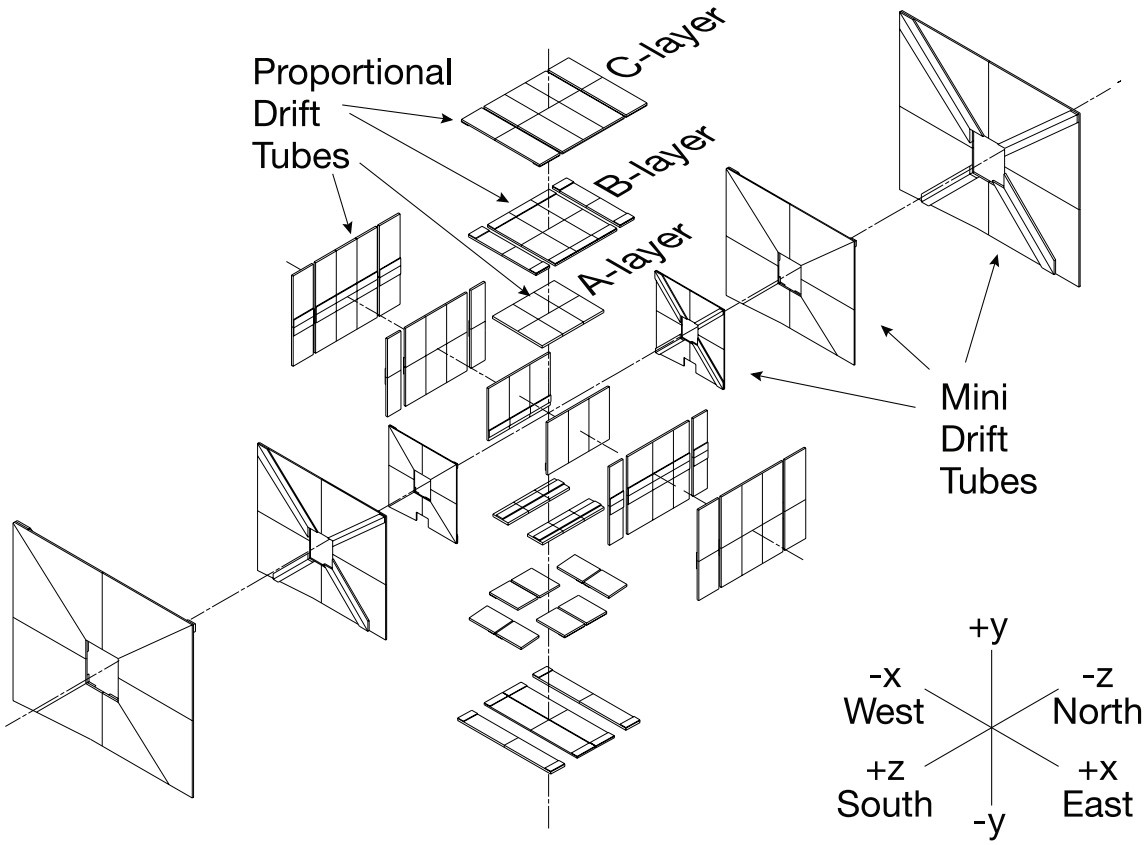

Figure 3.10: Exploded view of the drift tubes of the muon system.

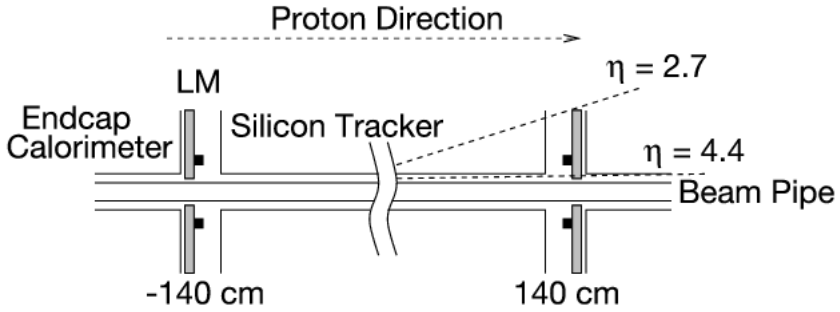

Figure 3.11: Position of the Luminosity Monitor in front of the two end cap calorimeters.

3.2.6 Forward Proton Detector

The forward proton detector (FPD) measures $p\bar{p}$ scattering processes at very small angles on the order of 1 mrad. A description of the FPD can be found in [28].

3.2.7 Trigger System and Data Acquisition

The purpose of the trigger system is to recognize interesting events, which will be recorded, and to reject most of the events. The decisions are taken in three distinct stages called Levels. Figure 3.12 gives an overview of the trigger system that is highly related with the data acquisition (DAQ). The Level 1 and Level 2 buffers are important to minimize the decision dead times of the triggers. The package COOR controls the overall coordination. The following paragraphs describe the three trigger Levels. From Level to Level more and more events are rejected based on decisions with increased complexity.

Level 1. The Level 1 trigger consists of hardware trigger elements. They look for interesting features of events and accept events at a rate of ≈ 2 kHz. The decision time is less than 3.5 μs.

Level 2. Hardware engines and embedded microprocessors take the Level 2 decisions. The rate is reduced by a factor of two to 1 kHz. Information on specific subdetectors are passed to a global processor that fires the trigger based on individual objects and event-wide object correlations. The Level 2 decision takes about 200 ms.

Level 3. The events passing the first two stages of the trigger are reconstructed on the Level 3 farm. The reconstruction software is similar to the offline software. The Level 3 trigger decision is based on completely reconstructed physics objects, and their relationships in the event. It takes about 200 ms per event. The trigger selection enriches the physics samples and reduces the rate to an acceptable level of 50 Hz. Events passing Level 3 are recorded on tape for the offline reconstruction.

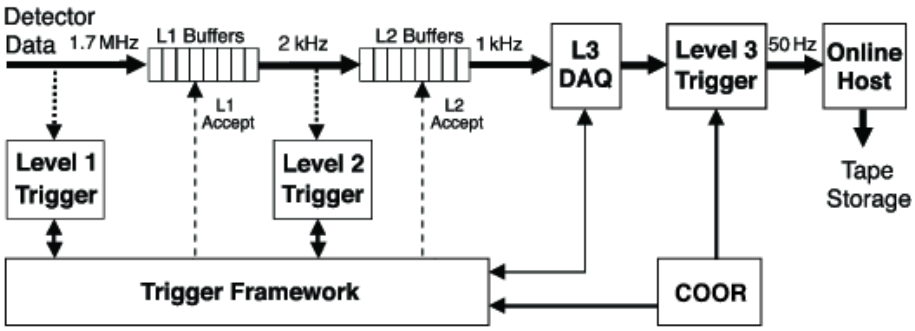

Figure 3.12: Overview of the trigger system and the data acquisition.

Chapter 4

Event Simulation and Reconstruction

4.1 Event Simulation

Event Generators. Event generators simulate all classes of processes in $p\bar{p}$ scattering, starting from the collision and the physics process, to the radiation of photons and gluons, the fragmentation of hadrons, and the decay of unstable particles. A simulated event is a list of particles with four-momenta, particle type (ID), and origin. The phase space according to the SM is populated randomly. That is why simulated events are sometimes referred to as Monte Carlo events. For the top quark mass analyzes the event generators PYTHIA [33] and ALPGEN [34, 35] are used.
The hard interaction between partons inside the proton and antiproton is calculated with perturbative quantum field theory, i.e. leading order Feynman diagrams. The parton momenta are taken from the parton density distribution CTEQ 6L1, see Section 2.2. The radiation of hard gluons can be calculated perturbatively. However, QCD is collinear and infrared divergent leading to many mainly soft gluons radiated at a small angle. The calculation of each single process is complicated or impossible at higher orders. At lower energy scales the perturbative series is less well-behaved due to the running of the strong coupling α_s. This is why the initial and final state radiation is simulated by parton showers based on empirical models. They rely on given probabilities for particles to radiate photons or gluons with a certain momentum. The parton shower simulates all radiated particles at once, thus not every single process has to be considered.
The fragmentation describes the formation of hadrons out of quarks and gluons. PYTHIA uses the string-fragmentation model, which is explained in [33, 36]. ALPGEN only calculates the hard interactions. The parton showering and fragmentation is done by PYTHIA. Since extra jets in an event can be calculated explicitly by Feynman diagrams or created by the parton shower there can be a double counting in determining the $X + n$ jets cross section. X is an arbitrary final state and n denotes the inclusive jet multiplicity. This problem is solved in ALPGEN by the so-called MLM-matching [34, 35]. Samples for each exclusive parton multiplicity are generated separately, the parton shower is simulated,

and then the jets are matched to the initial partons. The jets are found by a simple jet cone algorithm. Events will be rejected, if the parton multiplicity does not match the jet multiplicity. In the end the samples with different exclusive jet multiplicities are combined to one $X + n$ jets sample. A weight is assigned to each event to take into account the relative cross sections for processes with different parton multiplicity and to account for the different number of simulated events in each sub sample. This way of generating $X+n$ jets samples is useful to simulate high statistics $X+N$ partons samples with large N, even though the $X + 1$ partons cross section might be larger orders of magnitude than the $X + N$ parton cross section.

Detector Simulation, Digitization, and Underlying Event The next stage in the event simulation is the simulation of the detector. Interactions of particles with the DØ detector and its response are determined with the program D0GSTAR [37], a GEANT [38] simulation of the total geometry of the DØ detector within the DØ software framework.
An alternative to the standard GEANT simulation is a fast simulation called PMCS (Parameterized Monte Carlo Simulation) [39, 40]. Physics objects from the event generator are just smeared according to their known resolutions. PMCS does not simulate the interaction of particles with the detector. The simulation needs to be tuned to match the results from GEANT simulations or data. For the top quark measurements it is only used for studies of systematic uncertainties.
The program D0SIM uses the D0GSTAR output as input and does the digitization for each detector component.
Hits in the detector originate not only from particles produced in the hard interaction. In addition there are interactions between the proton and antiproton remnants. There can be residual energy from the previous bunch crossing. This effect is called pile-up. At very high instantaneous luminosities several hard interactions are likely to take place during the same bunch crossing. Finally, each detector component or their electronics produce noise hits. The uranium calorimeter for instance can produce hits caused by radiation of uranium decays. All these effects not coming from the hard scattering are summarized by the term underlying event. They all need to be implemented in the simulation. The effects of pile-up and noise are measured in zero-bias data events. These are events without any trigger conditions. The hits and energy depositions of the simulated events and zero-bias events are overlayed.

4.2 Event Reconstruction Chain

d0reco. The recorded raw data contain hits, energies, and trigger information. They need to be analyzed to reconstruct central tracks, electromagnetic clusters, hadronic clusters, missing transverse energy, and muon tracks. This is done by the program D0RECO. The final physics objects like electrons, muons, and jets are defined by identification criteria that will be described in Section 4.4.2 and following. D0RECO is the main

reconstruction software. The data taken at DØ are directly processed at the Fermilab computing farm.

d0correct. The package D0CORRECT calls all the post processing codes to do corrections and certifications for electromagnetic, muon, jet, and missing transverse energy objects.

Skimming. The Common Sample Group produces so-called skims, i.e. very loose preselected samples of all data by several skimming criteria [41]. Usually, analyzers produce their own sub-skims of the Common Sample Group-skims.

tmbanalyze. A further stage in the software chain is the program TMBANALYZE. It produces ROOT trees in a Common Analysis Format (CAF). ROOT is an object-oriented data analysis framework that is commonly used in high energy physics [42]. The trees can be analyzed in the analysis framework CAFE.

Cafe Packages. The CAFE framework provides standard tools for example to apply final corrections to leptons, apply the jet energy scale, and to calculate the fully corrected missing transverse energy. Differences in simulated lepton identification efficiencies compared to data are corrected by applying scale factors. The analysis specific skims and event selections are also done within CAFE.
The top quark mass measurement in the dilepton final state presented in this thesis is the first approved analysis of the top quark performed with this new analysis framework.

4.3 Data Reprocessing at Distributed Farms

The reconstruction software is continuously enhanced and improved. Based on studies with data, new calibrations become available, new reconstruction algorithms are developed, and the reconstruction software needs to be adopted to deal with for example an increased instantaneous luminosity. To take advantage of all these changes from time to time the complete set of raw data is reprocessed, i.e. reconstructed with a newer release of D0RECO. In 2005 a huge computing effort was made to reprocess 470 pb^{-1} of Run II DØ data. The main motivation is a new calibration of the electromagnetic calorimeter [43]. Table 4.1 illustrates the effort. Because the Fermilab computing farm continued to process the newly taken data, most of the reprocessing was accomplished by remote farms distributed all over the world. The raw data needed to be shipped to the farms and the output of the reconstruction needed to be shipped back to Fermilab. D0RECO produces two types of output, so-called DST files containing all the information of the event reconstructions, and so-called thumbnails (TMBs), which is a compressed file format with reduced information sufficient for most analyzes. The requirements on the remote reprocessing is to have a uniform software environment and a precise bookkeeping about all jobs and data transfers. This is enabled by the use of grid computing

software. The Fermilab grid project SAM-GRID [44] is composed of three functional blocks. It manages the job handling, the data handling, and the monitoring and information service. The job handling uses the standard grid technologies CONDOR-G [45] and the GLOBUS TOOLKIT [46]. SAM provides the data handling, a database for all data events and simulated events with access via meta data [47]. Grid computing stands for the job submission to several computing farms via a uniform interface. The SAM-GRID software has been installed and maintained at the Grid Computing Center Karlsruhe (GridKa) [48] and has been used for the reprocessing for six month. In parallel to the reprocessing, remote farms are used to simulate millions of events per week via grid computing.

Luminosity	470 pb^{-1}
Events	$1 \cdot 10^9$
Raw data 250 kB/event	250 TB
DSTs 150 kB/event	150 TB
TMBs 70 kB/event	70 TB
Time 50 s/event	20,000 months on 1 GHz Pentium III 6 months on 3400 CPUs

Table 4.1: Reprocessing effort in 2005.

4.4 Object Identification

4.4.1 Jets

Quarks and gluons form hadronic showers. They are reconstructed as jets in the hadronic calorimeter. Charged particles inside a jet are detected as tracks in the central tracker pointing to the hadronic cluster in the calorimeter. Jets without associated tracks are likely to be noise jets, i.e. non-physical jets with energy depositions originating from noise instead of particles. A jet reconstruction algorithm needs to be infrared and collinear safe. That means the result should be stable under the emission of a soft gluon and the exchange of a parton by two nearby partons of the same energy. The DØ Run II Cone Algorithm is designed with respect to these requirements. It is described in detail in [49,50]. The algorithm forms clusters in cones of size $\Delta R = 0.5$. Preclusters provided by a simple cone algorithm and midpoints between certain preclusters serve as seeds for clustering. The resulting proto-jets might overlap and share energy depositions. They need to be merged or split to avoid double counting of energy. Energy depositions that cannot be associated to a jet are called unclustered energy. The list of jet candidates still contains electrons, photons, and noise jets. To obtain a clean jet sample additional quality requirements are applied. Below, a list of all jet identification criteria is given [51]:

- *Hot Cell Removal.* Single calorimeter cells with energy depositions that are not related to events are called "hot cells". Energy clusters dominated by hot cells are partly removed by:

$$\frac{E_t(\text{leading cell})}{E_t(\text{next-to-leading cell})} \equiv \text{HotF} < 10$$

- *Hot Tower Removal.* Calorimeter towers are the combination of calorimeter cells with approximately the same η and φ. Hot towers consist mainly of hot cells. To remove hot towers the number of towers containing 90% of the jet energy, $n90$, needs to be larger than 1.

- *Electromagnetic Fraction.* The electromagnetic fraction f_{EM} of a cluster is the energy fraction that is deposited in the electromagnetic calorimeter. The maximum requirement $f_{EM} < 0.95$ discriminates jets from electrons or photons. A minimal f_{EM} helps to reject noise jets. This requirement is η-dependent since there is a gap in the electromagnetic calorimeter in the ICR region. Jets need to fulfill one of the following criteria:

$$f_{EM} > 0.05, \text{ or,}$$

$$||\eta_{\text{det}}| - 12.5| + \max(0, 40 \times (\sigma_\eta - 0.1))) < 1.3$$

$$f_{EM} > 0.03 \text{ and } 11.0 < |\eta_{\text{det}}| < 14.0$$

$$f_{EM} > 0.04 \text{ and } 2.5 < |\eta|.$$

  Here, η_{det} denote calorimeter cell coordinates with $\eta_{\text{det}} \approx 10 \times \eta$. σ_η is the width of a jet in η.

- *Coarse Hadronic Fraction.* The coarse hadronic fraction (CHF) is the energy fraction that is deposited in the coarse hadronic section, the outermost part of the hadronic calorimeter. Clusters with large CHF are mainly caused by calorimeter noise. To remove such jets, reconstructed jets are required to fulfill:

$$\text{CHF} < 0.4, \text{ or,}$$

$$\text{CHF} < 0.6 \text{ and } 8.5 < |\eta_{\text{det}}| \text{ (in the ECMH) and n90} < 20, \text{or,}$$

$$\text{CHF} < 0.44 \text{ and } |\eta| < 0.8, \text{ or,}$$

$$\text{CHF} < 0.46 \text{ and } 1.5 < |\eta| < 2.5.$$

- *Level1 Trigger Confirmation.* Jets need to be confirmed by the L1 trigger. The variable $L1_{\text{ratio}} = p_T^{\text{from L1 readout}}/p_T^{\text{from precision readout}}$ cross-checks that the energy read out with the precision readout and clustered into the jet roughly matches the energy visible in the L1 trigger readout. Good jets are required to fulfill one of the following criteria:

$$\text{L1}_{\text{ratio}} > 0.5, \text{ or,}$$

$$\mathrm{L1_{ratio}} > 0.35, \text{ and } \mathrm{p_T} < 15 \text{ GeV}, \text{ and } 1.4 < |\eta|, \text{ or,}$$

$$\mathrm{L1_{ratio}} > 0.1, \text{ and } \mathrm{p_T} < 15 \text{ GeV}, \text{ and } 3.0 < |\eta|, \text{ or,}$$

$$\mathrm{L1_{ratio}} > 0.2, \text{ and } \mathrm{p_T} \geq 15 \text{ GeV}, \text{ and } 3.0 < |\eta|.$$

A study of improvements of the L1 trigger confirmation can be found in [52].

Jet Energy Scale

The measured energy of a jet $E_{\mathrm{jet}}^{\mathrm{raw}}$ does not exactly correspond to the energy of the initial parton. Figure 4.1 shows in a sketch the evolution from a parton produced in the hard scattering process to a jet in the calorimeter. The jet energy scale (JES) corrects the measured jet energy, accounting for the cone algorithm, energy depositions of the underlying events, and the response of the calorimeter. The corrections are derived and applied successively. The corrected energy $E_{\mathrm{jet}}^{\mathrm{corr}}$ is calculated by:

$$E_{\mathrm{jet}}^{\mathrm{corr}} = \frac{E_{\mathrm{jet}}^{\mathrm{raw}} - O}{F_\eta \times R \times S}. \tag{4.1}$$

The first correction is the subtraction of the offset energy O. It is defined as calorimeter energy depositions inside the jet cone that are not associated with the hard scattering process. These contributions arise from the underlying event, as described in Section 4.1. The correction is measured as the average energy density deposited in each calorimeter tower in minimum bias events. Minimum bias events are events that are only triggered by the luminosity monitor and likely to be inelastic proton-antiproton collisions. It is assumed that minimum bias events are representative for the underlying events. The number of primary vertices is a measure for the instantaneous luminosity.
The second JES correction F_η calibrates the non-uniform calorimeter response as a function of the pseudo-rapidity. This correction is largest in the ICR region. It is measured using γ+jets and di-jets data. The relative response is related to the imbalance in the event between photon and probe jet, or between tag jet and probe jet, respectively. F_η is determined for data as well as for simulated events.
The absolute response correction R is the largest in magnitude of the correction factors with about 30%. Similar to the relative response it is measured using $\gamma +$ jet data. The photon is required to be opposite to the jet. This relates the hadronic response after offset and the relative response correction to the photon energy scale. The same method is applied to simulated events.
The last correction is the showering correction S. It evaluates energy leaking inside or outside the jet cone. Gluon emissions at a large angle are not considered as those gluons are regarded as independent partons or jets. Only instrumental effects like the shower development in the calorimeter and the bending inside the magnetic field are corrected for. The energy profiles of jets as a function of jet energy, η, and radius are investigated in data and in simulated events. The simulation at particle level yields the physical shower development without detector effects.

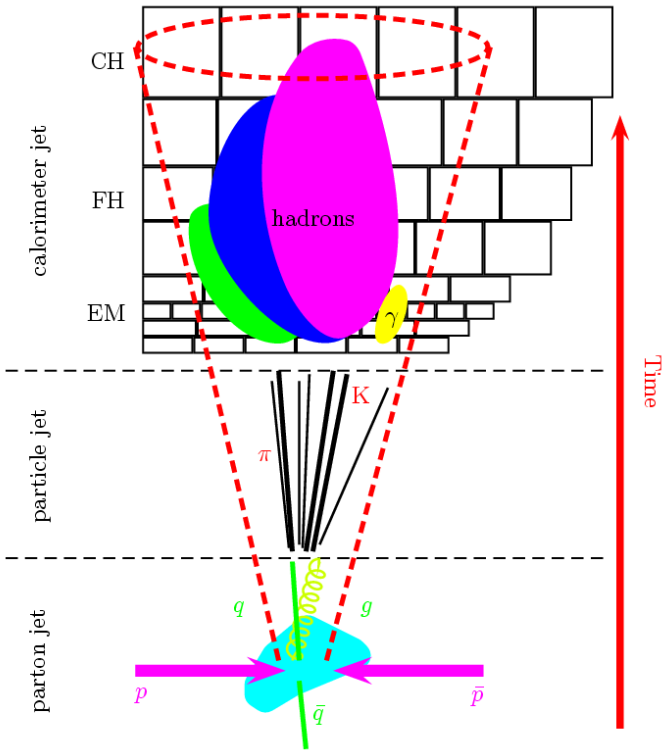

Figure 4.1: Sketch of the evolution of partons from the hard scattering process to a jet in the calorimeter.

Simulation of Jets

The jet identification and reconstruction efficiencies and the measured energies of the simulation are corrected to match the data. Simulated jet energies are smeared to degrade the resolution and the energies are shifted. Jets are randomly removed to account for a too high reconstruction efficiency. These corrections are applied after the jet energy corrections [53].

4.4.2 Electrons

Electrons are identified using information from the calorimeter, the preshower detector, and the inner tracking system. A detailed description of the electron reconstruction at DØ can be found in [54, 55]. The first step of identifying electrons is the clustering of calorimeter cells. Electromagnetic (EM) clusters are candidates for photons and electrons. To identify electrons further quality criteria are applied. Finally, good discrimination between electrons and background is achieved by an electron likelihood.

Electromagnetc Cluster Reconstruction

Cells with the same η and φ coordinates are grouped together to form towers. The energy of an EM tower is the sum of the energies measured in the four EM layers and the first hadronic layer of the calorimeter. An EM tower used for triggering is of the size 0.2×0.2 in $\Delta\eta \times \Delta\varphi$, and the readout tower is of size 0.1×0.1 in $\Delta\eta \times \Delta\varphi$. A simple cone algorithm is used to form EM clusters out of these towers. In the central calorimeter adjacent EM towers with at least 50 MeV transverse energy are added within a cone around the tower with highest transverse energy. The cone size is $\Delta R = 0.4$. In the endcap calorimeter adjacent cells are added together starting from a cell in the third EM layer with highest energy. The added cells must have a maximum distance to the initial cell of 10 cm. Clusters need to pass the following criteria:

- *Transverse Energy.* The minimum transverse energy of a cluster is 1.5 GeV.
- *Narrow Shape.* 40% of the cluster energy must be contained in the most energetic tower to enforce a narrow shape of the cluster.
- *Electromagnetic Fraction.* The electromagnetic fraction f_{EM} is the ratio of energy deposited in the electromagnetic calorimeter to the total energy deposited in the calorimeter. $f_{EM} \geq 0.9$.
- *Isolation.* $E_{EM}(\Delta R)$ is the energy that is deposited in a cone around the EM object of size ΔR in the EM layers and the first hadronic layer of the calorimeter. The isolation is defined as: $f_{\text{iso}} = (E_{EM}(0.4) - E_{EM}(0.2))/E_{EM}(0.2)$. EM clusters are required to fulfill: $f_{\text{iso}} \leq 0.2$.

EM clusters passing all the criteria above are candidates for photons and electrons. They are matched to clusters in the preshower detector by a spatial matching in $\Delta\eta \times \Delta\varphi$ of size 0.05×0.05.

Electron Quality Requirements

EM clusters come from photon, electrons, or background like pions. Additional quality requirements are necessary to select electrons with a high purity. All electrons used for the analyzes in this thesis fulfill the following quality criteria [55]:

- *Isolation.* The isolation requirement defined above is tightened: $f_{\text{iso}} \leq 0.15$.
- *Shower Shape.* Seven correlated observables are used for the analyzes of the shower shape of electromagnetic objects: four electromagnetic energy fractions, the total electromagnetic energy, the vertex z-position, and the transverse shower width in φ. The H-matrix is the inverse of the 7×7 covariance matrix of those variables [56, 57]. It is a measure of how similar the shower is to an electron shower. The χ^2 of the comparison of the observed H-matrix and an electron H-matrix is required to be less the 50.

- *Track match.* A track needs to be matched to the EM cluster in E/p.
- *Track p_T.* Track $p_T \geq 5$ GeV.
- *Likelihood.* Likelihood ≥ 0.85. Without this criteria electrons are called loose electrons, otherwise they are called tight electrons. The electron likelihood is described in the next section.

Electron Likelihood

A further reduction of background can be achieved by an electron likelihood. It is trained to separate electrons from photon conversions and hadronic overlaps. The following seven variables are used:

- Electromagnetic fraction f_{EM}, as defined above.
- H-matrix-χ^2, as defined above.
- The ratio of transverse energy and momentum E_T/p_T.
- The probability of the χ^2 of the spatial track match.
- Distance of closest approach (DCA). The DCA is the distance between the electron track and the primary vertex in the transverse plane.
- Number of tracks in a cone of size $\Delta R = 0.05$ around the candidate track, including the candidate itself.
- Total transverse track momentum.

4.4.3 Muons

Muons are identified in the muon system, the calorimeter, and the inner tracking system. Below, the identification and quality criteria for muons used for the analyses are given [32].

Muon Reconstruction in the Muon System. Muon tracks in the local muon system need to have hits in the A layer inside of the toroid and also hits in the B or C layer outside of the toroid. At least two A layer wire hits and at least one A layer scintillator hit is required. In the B or C layer at least two wire hits and one scintillator hit is required. The scintillator hit in the BC layer can be omitted, if there are less then four BC wire hits.

Muon Reconstruction in the Calorimeter. Muons are minimum ionizing particles and deposit about 3 GeV of their energy in the calorimeter. Due to the fine granularity of the DØ calorimeter those energy depositions can be seen as a track of calorimeter cells. This track is matched in $\Delta\eta$ and $\Delta\varphi$ to a central track that is extrapolated to the calorimeter. The muon reconstruction efficiency in the calorimeter is only about 50%, far less then for other muon signatures.

Central Muon Track. Muons that are reconstructed in the muon system are matched to a track in the inner tracking system. The inner track is required to have medium quality. That means the track fit needs to fulfill $\chi^2/d.o.f. < 4$, and the track needs to pass the *dca* (defined as for electrons) criteria: $|dca| < 0.02$ cm for tracks with SMT hits, or $|dca| < 0.2$ cm for tracks without SMT hits. If the track fit converged in the local muon system, the local track is matched to a central track, otherwise central tracks are matched to a local muon.

Muon Isolation. Muons coming from $t\bar{t}$ decays are expected to be isolated, in contrast to muons originating from jets, e.g. from semi-leptonic B meson decays. Isolated muons fulfill two isolation criteria. The first one is isolation in the central tracker:

$$\sum_{\text{tracks}} p_T/p_T(\mu) < 0.15, \tag{4.2}$$

where $\sum_{\text{tracks}} p_T$ is the sum of all transverse track momenta in a cone around the muon track of size $\Delta R = 0.5$. The second criteria is isolation in the calorimeter:

$$|\sum_{\text{cells}} E_T/p_T(\mu)| < 0.15, \tag{4.3}$$

where $\sum_{\text{cells}} E_T$ is the sum of all calorimeter cell energies in a hollow cone of size $0.1 < \Delta R < 0.4$ around the muon calorimeter-track.

Cosmic Veto. The cosmic veto rejects muons from cosmic rays using scintillator hit time information. Muon hits are only accepted within a ± 10 ns window around the expected muon arrivals in the A-, B-, or C-layer. Cosmic muons have random timing information. The *dca* quality criteria already reduce the cosmic muon background a lot.

4.4.4 Missing Transverse Energy

In the initial state of a $p\bar{p}$ collision, there is no transverse momentum, neglecting intrinsic transverse momenta of partons inside the proton or antiproton. As a consequence of momentum conservation there is a balance of the momenta of all particles of the event in the transverse plane, i.e. the sum of all transverse momenta equals zero. However, particles like neutrinos are not detected and therefore lead to an imbalance in the sum of measured momenta, which is called missing transverse energy $\not\!\!E_T$.
The $\not\!\!E_T$ is calculated from all calorimeter cells, except the coarse hadronic cells, because

those have the highest noise rate. Since good jets contain a physical coarse hadronic energy fraction, the $\not\!\!E_T$ is corrected for this energy fraction. Energy clusters belonging to good jets or EM objects are corrected by the jet energy scale or EM energy scale. This correction is also propagated to the $\not\!\!E_T$. Finally, $\not\!\!E_T$ is corrected for muons in the event. Muons are minimum ionizing particles, i.e. they deposit only very little of their energy in the calorimeter leading to fake $\not\!\!E_T$. The momentum measurement of muon tracks is added to the $\not\!\!E_T$ and the energy depositions in the calorimeter are subtracted using a GEANT-look-up table. Details of the $\not\!\!E_T$ calculation and all corrections can be found in [58].

Chapter 5

Measurement of the Top Quark Mass

In this chapter the measurement of the top quark mass is presented. First, the dataset and event selection is described. After a discussion of the dilepton event kinematics there is an introduction of the Neutrino Weighting Method to extract the top quark mass. Different approaches are presented to model probability density functions. The final results on the top quark mass including a discussion of systematic uncertainties are given.

5.1 The Data Samples

1.05 fb^{-1} of DØ Run II collider data collected in the period between April 2002 and February 2006 are analyzed in the $e\mu$, ee, and $\mu\mu$ final states. Top quark mass measurements are presented in all three channels. Earlier results of a data sub-sample of approximately 835 pb^{-1} in the $e\mu$ channel only are also presented. Different approaches of the mass measurements are described and compared. Three different methods are applied to the 835 pb^{-1} data sample, and one improved method arising from the previous methods is applied to the full 1.05 fb^{-1} dataset.

5.2 Event Selections

The selected events are required to pass a dielectron trigger, an electron-plus-muon trigger, or a combination of single muon triggers in the ee, $e\mu$, or $\mu\mu$ channel, respectively. Offline, all three channels require at least two high p_T jets, two high p_T charged leptons, and topological requirements. The following subsections present all criteria and control distributions for the three dilepton channels. In the $e\mu$ channel two almost identical selections are described, one being applied to the 835 pb^{-1} data sample, and the other one to the 1.05 fb^{-1} data sample. The main difference is a better understanding of the efficiencies of the applied triggers leading to better data-to-simulation agreement in the control sample with zero jets, as will be discussed in Section 5.9.

5.2.1 Signal Signatures and Backgrounds

Electron-Muon Channel. The $e\mu$ final state consists of an isolated electron and muon with high transverse momenta, two high p_T b-jets, and missing transverse energy due to the two neutrinos. The main background that mimics the same signature is $Z \to \tau\tau$[1] production associated with at least two jets. One τ lepton decays in a muon, the other one in an electron. Another background is diboson production, i.e. WW, WZ, and ZZ production associated with two or more jets. The signature of the production of two W bosons is closest to the signal as the charged leptons have a higher transverse momentum than the leptons originating from $Z \to \tau\tau$ decays. The WZ and ZZ production have smaller cross sections and the event yields are negligible for the top quark mass analysis. Another source of background are instrumental fakes of electrons. They can arise from multijet production with a jet faking an electron and a muon originating from a semi-leptonic decay, or a W boson decay.

Dielectron Channel. The ee channel has the same signature as the $e\mu$ channel with an electron instead of a muon. The main background source is the Z plus 2 jets $\to$ ee plus two jets production. Effective selection variables to suppress this background are the invariant dielectron mass and missing transverse energy, since there are no neutrinos in the final state of $Z \to ee$ boson production. Observed missing transverse energy is caused by energy misreconstruction. Z production with physical missing transverse energy comes from the process $Z \to \tau\tau \to ee$ plus neutrinos. Further backgrounds are diboson production, but with two electrons in the final state. Besides $Z \to ee$ events, there is a second type of instrumental background. One or two electrons can be faked by jets of multijet production.

Dimuon Channel. The $\mu\mu$ channel has two muons in the final state. Since high p_T muons have a worse momentum resolution than high p_T electrons, this channel has the worst missing transverse energy resolution. This makes it more difficult to reject the main $Z \to \mu\mu$ plus jets background. The other background processes are $Z \to \tau\tau \to \mu\mu$ plus neutrinos and jets, diboson production, and fake muon events. Fake muons are muons with a fake isolation. They originate for example from semi-leptonic B meson decays inside a b-jet. Given the muon identification criteria described in the previous chapter the number of misidentified muons, e.g. caused by punchthrough particles, is negligible.

5.2.2 Dilepton Selection

The dilepton selections are developed for top quark properties measurements as well as for top quark cross section measurements. Details of the selections can be found in [59] for the $e\mu$ channel, in [60] for the ee channel, and in [61] for the $\mu\mu$ channel.

[1] This notation is used as short form for the Drell-Yan process $Z/\gamma^* \to l^+l^-$

Common Selection. The three dilepton channels use common lepton identifications as defined in Sections 4.4.2 and 4.4.3. The same requirements on data quality, jets, and the primary vertex are applied:

- *Data Quality:* Only data with a fully operational detector are considered. Luminosity blocks marked as bad are removed.
- *Jets:* Two or more jets are required with $p_T(j) > 20$ GeV and $|\eta_{\text{det}}| < 2.5$.
- *Primary Vertex:* The z-position of the primary vertex should be well within the fiducial region of the silicon tracker: $|z_{\text{PV}}| < 60$ cm. At least three tracks need to be associated with the primary vertex. The distance in the z direction between the high p_T lepton tracks and the primary vertex is required to be: $|z_{\text{lep}} - z_{\text{PV}}| < 1$ cm.

The decay channel specific criteria are given below.

Electron-Muon Selection. Events in the $e\mu$ final state need to pass the following selection criteria:

- *Muon:* One isolated muon with a timing cut against cosmic muons is required. The transverse momentum and pseudorapidity criteria are: $p_T(\mu) > 15$ GeV and $|\eta| < 2$.
- *Electron:* Events need to have one isolated tight electron with a transverse momentum of $p_T(e) > 15$ GeV. The pseudorapidity of the electron is required to be in the region $|\eta| < 1.1$ or $1.5 < |\eta| < 2.5$. The electron must not have a common track with a muon. There is a veto against a second loose electron in the event.
- Electron and highest p_T muon in the event must have opposite charge.
- H_T: H_T is a topological variable defined as the scalar sum of the p_T of all jets in the event, and the p_T of the leading lepton. Background events with radiated gluon jets tend to have less H_T than signal events. The requirement for the selection of the 835 pb^{-1} data sample is: $H_T > 120$ GeV. For the 1.05 fb^{-1} data sample a new optimization is performed resulting: $H_T > 115$ GeV.

Figure 5.1 shows control distributions of kinematic variables for the selected data events, simulated signal, and the background model in the $e\mu$ channel. The agreement between data and simulation confirms a good understanding of the sample composition. Control distributions for the 835 pb^{-1} data sample can be found in Appendix B.

Dielectron Selection. The dielectron selection criteria are:

- *Electrons:* The two electrons need to be tight, with opposite charge, $p_T > 15$ GeV, and with pseudorapidities in the regions $|\eta| < 1.1$ or $1.5 < |\eta| < 2.5$.
- *Invariant Dielectron Mass:* Events with an invariant dielectron mass M_{ee} in the range 80 GeV to 100 GeV and $M_{ee} < 15$ GeV are rejected to suppress the $Z \to ee$ background.

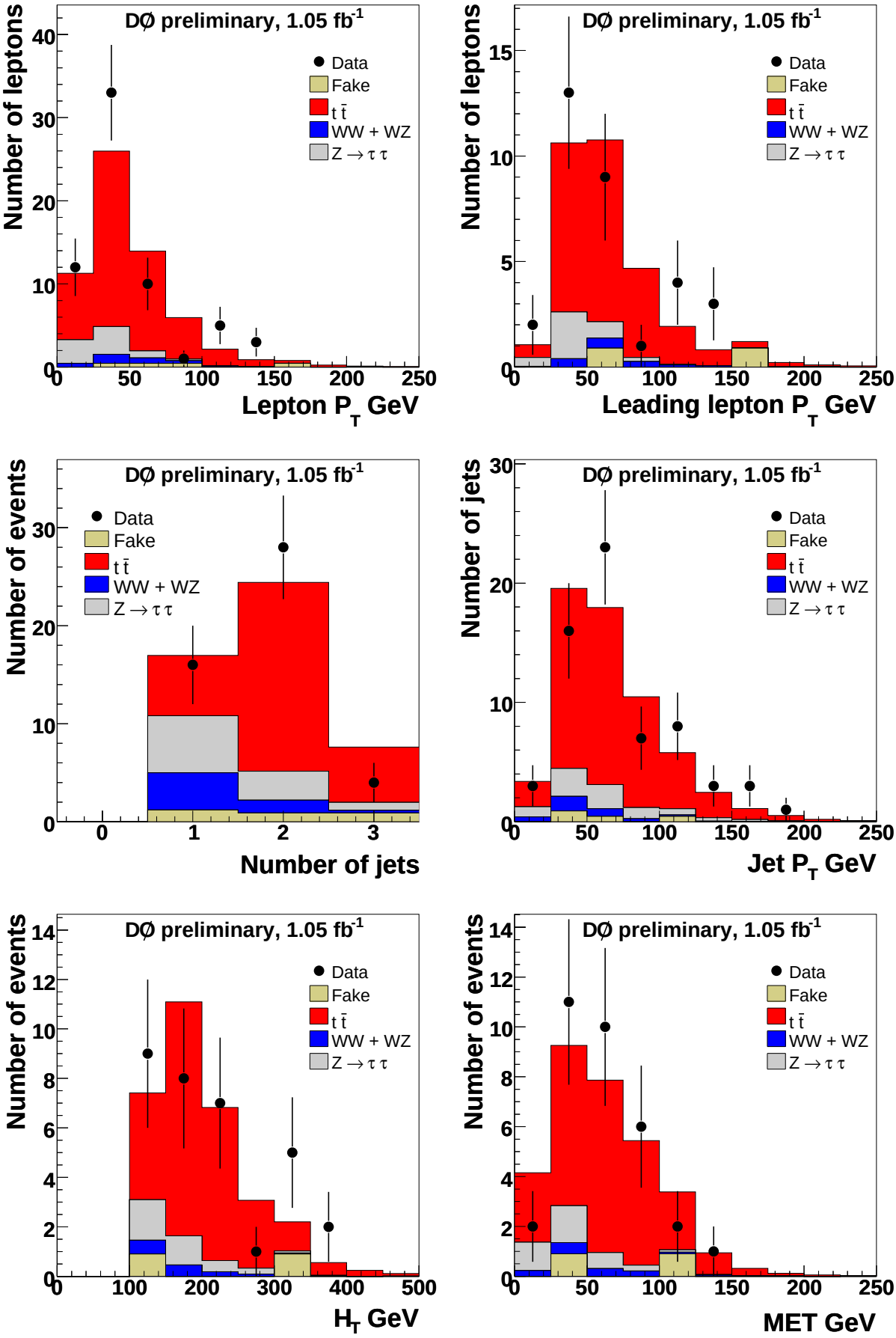

Figure 5.1: Control distributions of the $e\mu$ selection.

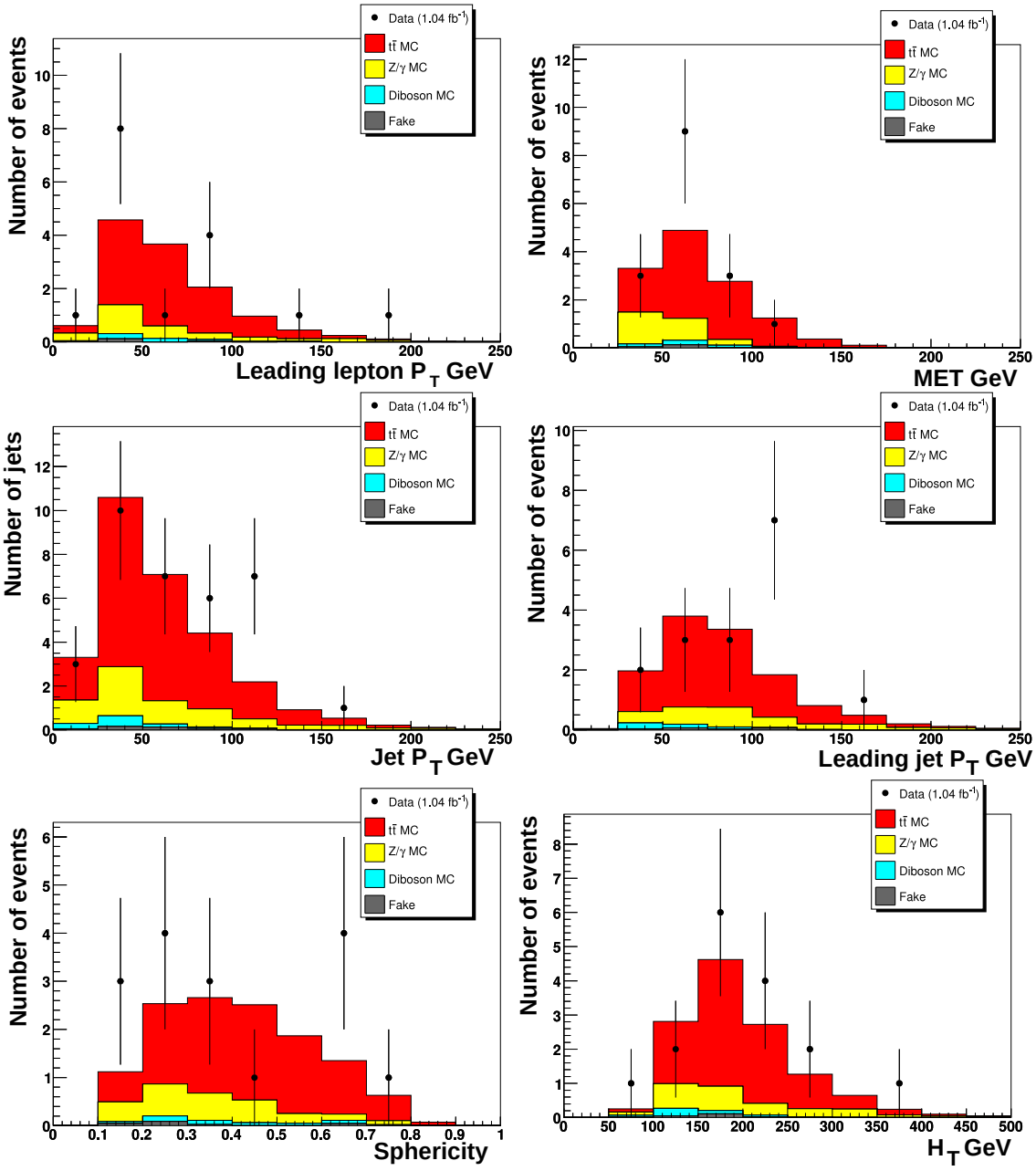

Figure 5.2: Control distributions of the dielectron selection.

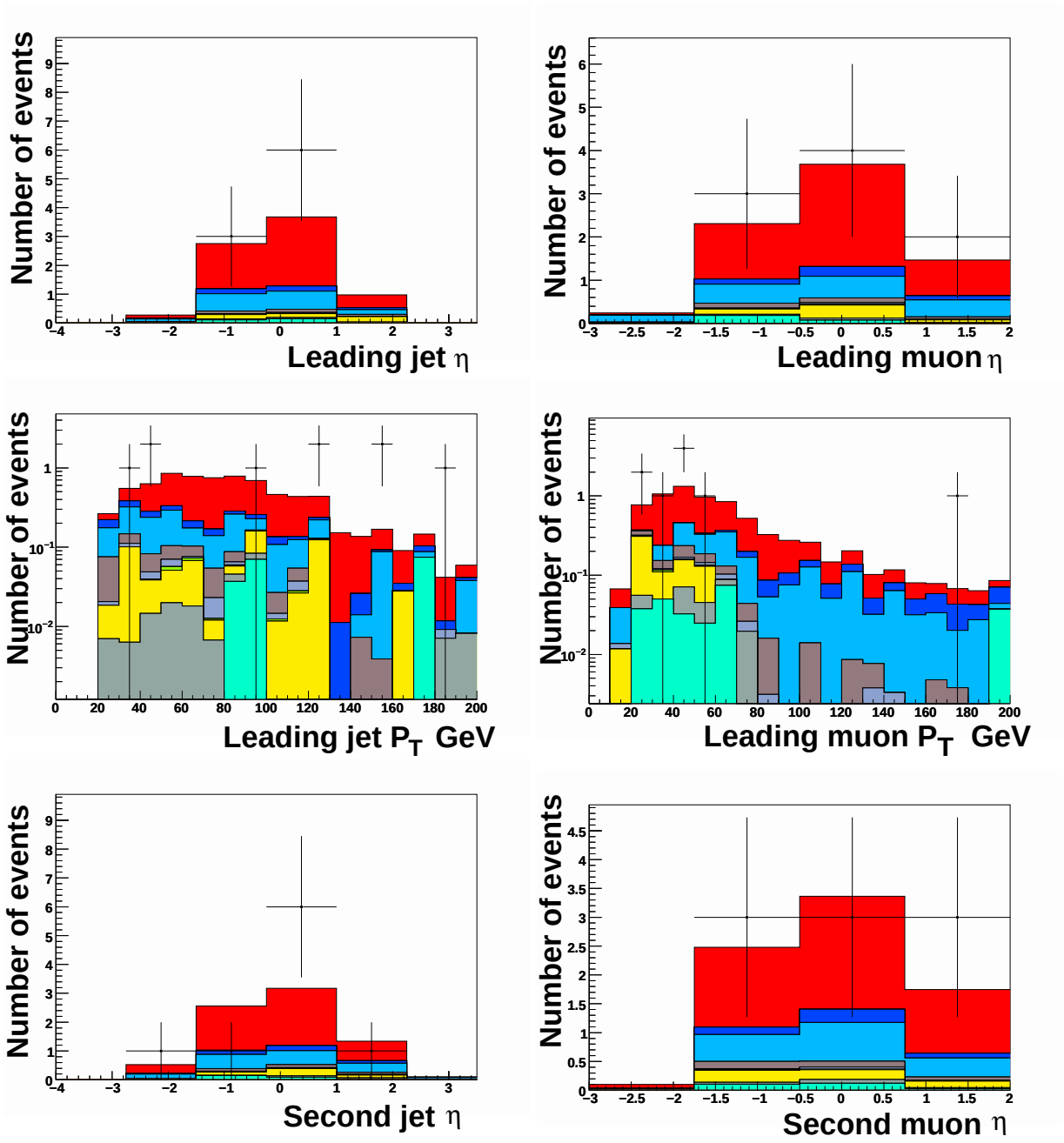

Figure 5.3: Control distributions of the $\mu\mu$ selection. The p_T spectra of the leading jet and leading muon are given in a logarithmic scale. The black entries show the data, the simulation of signal is red, $Z \to \mu\mu$ is blue, $Z \to \tau\tau$ is yellow, and diboson events are shown in grey.

- *Missing Transverse Energy:* The missing transverse energy criteria depends on M_{ee}. For $M_{ee} < 80$ GeV, events need to pass $\not\!\!E_T > 40$ GeV while for $M_{ee} > 100$ GeV events need to pass $\not\!\!E_T > 35$ GeV.

- *Sphericity:* The event topology can be described by the normalized momentum tensor, defined as:

$$\mathcal{M}_{ij} = \frac{\sum_o p_i^o p_j^o}{\sum_o |\vec{p^o}|^2}, \tag{5.1}$$

where the sum is taken over all objects o in the event, and i, j denote the Cartesian components of the momenta $\vec{p^o}$. The sphericity $\mathcal{S}$ is a measure of how spherical the objects are distributed in the event. Signal events tend to have greater sphericity values than background events. The sphericity is defined as $\mathcal{S} = \frac{3}{2}(\varepsilon_1 + \varepsilon_2)$, where ε_i is the i^{th} eigenvalue of $\mathcal{M}$. The selection criteria is: $\mathcal{S} > 0.15$. The sphericity distribution for signal and background events is shown in Figure 5.2 (bottom left).

The control distributions of kinematic variables in the *ee* channel can be seen in Figure 5.2. Within the given statistics there is a good agreement between observed and expected distributions.

Dimuon Selection Below the selection criteria for the dimuon channel are given:

- *Muons:* At least two isolated muons with $p_T > 15$ GeV and $|\eta_{\text{det}}| < 2$ are required. One pair of muons need to have opposite charge.
- There is a veto against loose electrons in the events.
- Events need to have a minimal invariant dimuon mass $M_{\mu\mu} > 30$ GeV to pass the selection.
- *Missing Transverse Energy:* The missing transverse energy needs to be at least 35 GeV.
- *Contour Cut:* The missing transverse energy requirement will be tightened, if the leading muon and the missing transverse energy point almost in the same direction or are back-to-back in the transverse plane.
- *Z-Fitter:* The invariant dimuon mass is a very effective variable to reject resonant $Z \to \mu\mu$ background. Instead of applying a simple cut criteria, a one dimensional fit is performed. It tests the hypothesis that an event is a $Z \to \mu\mu$ event given the momentum resolution of the leading two muons. A χ^2 is defined as:

$$\chi^2(p(\mu_1^{\text{fit}}), p(\mu_2^{\text{fit}})) = \left(\frac{1/p(\mu_1) - 1/p(\mu_1^{\text{fit}})}{\sigma_1(p(\mu_1), \eta(\mu_1))}\right)^2 + \left(\frac{1/p(\mu_2) - 1/p(\mu_2^{\text{fit}})}{\sigma_2(p(\mu_2), \eta(\mu_2))}\right)^2, \tag{5.2}$$

where $p(\mu_i)$ is the measured momentum of muon i, $p(\mu_i^{\text{fit}})$ are refitted muon momenta, and σ_i are the muon resolutions depending on the transverse muon momentum and pseudorapidity. The χ^2 is minimized with the constraint: $M_{\mu\mu} = 2p(\mu_1^{\text{fit}})p(\mu_2^{\text{fit}})(1 - \cos\sphericalangle(\mu_1, \mu_2)) = M_Z$. The Z boson mass M_Z relates $p(\mu_1^{\text{fit}})$ and $p(\mu_2^{\text{fit}})$. Events with $\chi^2 > 8$ are selected.

The dimuon selection yields the smallest number of candidates. Figure 5.3 shows control distributions. The p_T spectra of leading jet and the leading muon are given in a logarithmic scale.

5.2.3 Event Yields

In order to retain sufficient signal efficiency for an optimal cross section or properties measurement, the event selections allow significant background. The expected numbers of background and signal events in all three channels (assuming a top pair production cross section of 7 pb) are listed in Tables 5.1 to 5.4 along with the observed number of candidates. In the electron-muon channel with the highest branching ratio 32 events are observed. In the dielectron channel 16 candidates, and in the dimuon channel 9 candidates are selected. For the $e\mu$ selection of the 835 pb^{-1} sub-sample 28 candidates are obtained. The two $e\mu$ selections have 26 candidates in common.

Table 5.1: Expected and observed $e\mu$ event yield for signal and background processes, after all selection cuts are applied to the 835 pb^{-1} data sample.

$t\bar{t} \to e\mu$	WW	$Z \to \tau\tau$ ($\tau\tau \to e\mu$)	fake e	total	observed
20.2 ± 2.7	$1.24^{+2.2}_{-0.5}$	$2.7^{+1.5}_{-1.3}$	0.4 ± 0.2	$24.6^{+3.8}_{-3.0}$	28

Table 5.2: Expected and observed $e\mu$ event yield for signal and background processes after all cuts are applied to the 1.05 fb^{-1} data sample.

$t\bar{t} \to e\mu$	WW	$Z \to \tau\tau$ ($\tau\tau \to e\mu$)	fakes	total	observed
$28.58^{+2.12}_{-2.39}$	$1.37^{+0.59}_{-0.59}$	$3.57^{+0.67}_{-0.81}$	$0.30^{+0.17}_{-0.14}$	$35.31^{+2.82}_{-3.18}$	32

Table 5.3: Expected and observed ee event yield for signal and background processes after all cuts are applied to the 1.05 fb^{-1} data sample.

$t\bar{t} \to ee$	WW	$Z \to ee$ (fake $\not\!\!E_T$)	fake e	total	observed
9.75 ± 0.10	0.36 ± 0.04	1.12 ± 0.03	0.22 ± 0.07	12.87 ± 1.31	16

Table 5.4: Expected and observed $\mu\mu$ event yield for signal and background processes after all cuts are applied to the 1.05 fb^{-1} data sample.

$t\bar{t} \to \mu\mu$	WW	$Z \to \mu\mu$	$Z \to \tau\tau$ ($\tau \to \mu$)	fakes	total	observed
$5.80^{+0.38}_{-0.40}$	0.28 ± 0.12	$2.19^{+0.81}_{-1.56}$	$0.52 \pm ^{+0.22}_{-0.25}$	0.37 ± 0.13	$9.35^{+0.93}_{-1.63}$	9

5.3 Neutrino Weighting

Neutrino Weighting is the name of the method to extract the top quark mass in dilepton events. It was first applied in Run I [62–64].
This section starts with a discussion of kinematics in dilepton events, followed by an introduction to the method.

5.3.1 Kinematic Reconstruction

In the $t\bar{t}$ dilepton final states there are six particles: two b-jets, two charged leptons, and two neutrinos[2]. In total these are $6 \times 4 = 24$ degrees of freedom. The masses of all these particles are known. The momenta of the charged leptons and the jets are measured. The two neutrinos, however, cannot be detected. Only the sum of their momenta in x and y direction are reconstructed as missing transverse energy. This leaves four undetermined degrees of freedom. In addition, there are three kinematic constraints. The decays of the two W bosons yield:

$$M_{W_1}^2 = (E_{\nu_1} + E_{l_1})^2 - (\vec{p}_{\nu_1} + \vec{p}_{l_1})^2 \tag{5.3a}$$

$$M_{W_2}^2 = (E_{\nu_2} + E_{l_2})^2 - (\vec{p}_{\nu_2} + \vec{p}_{l_2})^2, \tag{5.3b}$$

where index '1' stands for the semi-leptonic pair, coming from the first W boson and index '2' stands for the semi-leptonic pair, coming from the second W boson. From the decay of the top pair follows:

$$m_{\text{top}} = (E_{\nu_1} + E_{l_1} + E_{b_1})^2 - (\vec{p}_{\nu_1} + \vec{p}_{l_1} + \vec{p}_{b_1})^2 = (E_{\nu_2} + E_{l_2} + E_{b_2})^2 - (\vec{p}_{\nu_2} + \vec{p}_{l_2} + \vec{p}_{b_2})^2, \tag{5.4}$$

where it is assumed that the masses of the top quark and of the antitop quark are equal. Without supplying further information, the kinematics is underconstrained by one degree of freedom. In the Neutrino Weighting approach, one assumes a top quark mass *a priori*. Then neutrino rapidities are chosen. The $\not\!\!E_T$ is ignored as a constraint, and is instead used to test the validity of these assumptions. The calculation to reconstruct the top quark mass can be found in Appendix A. The distribution of neutrino rapidities can be well-described by a Gaussian with a width that is weakly dependent on the top quark mass. Figure 5.4 (left) shows an example of a neutrino η^ν distribution for simulated $e\mu$ signal events with $m_{\text{top}} = 175$ GeV. The dependency of the width of the Gaussian on the top quark mass is parametrized as:

$$\eta^\nu(m_{\text{top}}) = 1.45 - (4.05 \times 10^{-3})\ m_{\text{top}} + (9.19 \times 10^{-6})\ m_{\text{top}}^2 \quad (e\mu \text{ channel}), \tag{5.5}$$

$$\eta^\nu(m_{\text{top}}) = 1.27 - (1.86 \times 10^{-3})\ m_{\text{top}} + (2.70 \times 10^{-6})\ m_{\text{top}}^2 \quad (ee \text{ channel}), \tag{5.6}$$

$$\eta^\nu(m_{\text{top}}) = 1.39 - (3.93 \times 10^{-3})\ m_{\text{top}} + (8.91 \times 10^{-6})\ m_{\text{top}}^2 \quad (\mu\mu \text{ channel}). \tag{5.7}$$

The parametrization can be seen in Figure 5.4 (right). The differences between the three channels arise from the different selection criteria.
The addition of three constraints from the top mass and neutrino rapidity assumptions, combined with the loss of two constraints from ignoring the measured $\not\!\!E_T$, results in a net addition of one constraint. This makes the problem solvable to obtain the momentum of each of the two neutrinos. These equations are quadratic for each neutrino, therefore one can have 0, 2 or 4 real solution combinations for each $t\bar{t}$ event. The top quark mass can then be reconstructed for each solution via:

$$m_{\text{top}}^2 = (E_\nu + E_l + E_b)^2 - (\vec{p}_\nu + \vec{p}_l + \vec{p}_b)^2. \tag{5.8}$$

[2]In the following, there is no distinction between particles and anti-particles in the text and formula, if not necessary.

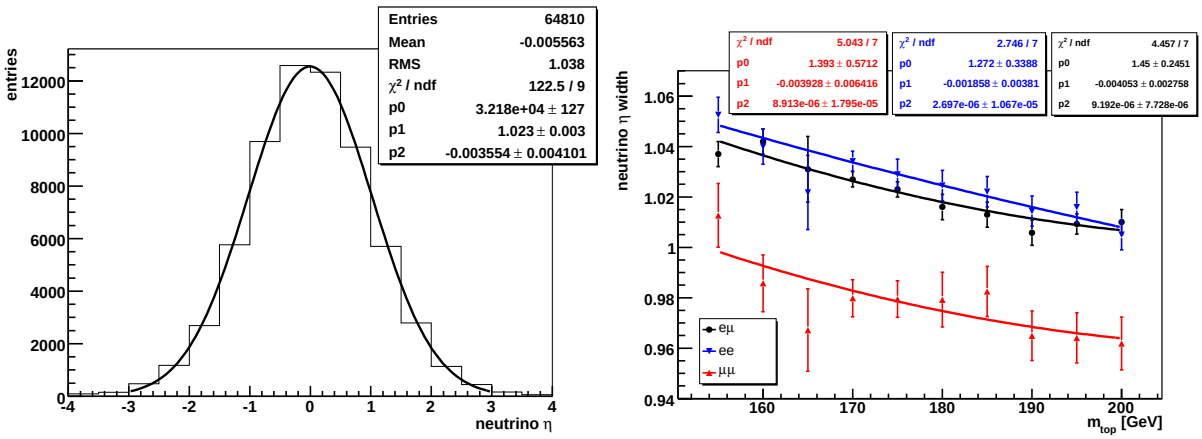

Figure 5.4: Example neutrino η distribution with Gaussian fit for simulated $e\mu$ events with $m_{\text{top}} = 175$ GeV (left) and parametrization of neutrino η width vs. m_{top} for all three channels (right).

5.3.2 Neutrino Weight

For each pairing of neutrino solutions, the expected missing transverse energy $\not{E}_x^{\text{calc}}$ and $\not{E}_y^{\text{calc}}$ can be calculated from the solved neutrino momenta. This is compared to the measured missing transverse energy $\not{E}_x^{\text{obs}}$ and $\not{E}_y^{\text{obs}}$ in the event by allowing for a Gaussian missing energy resolution σ_{E_x} and σ_{E_y}. A weight ω is calculated that will be greatest, if the observed and expected missing transverse energy match:

$$\omega = \sum_{i=1}^{N_{\text{iter}}} \exp\left(\frac{-(\not{E}_{x,i}^{\text{calc}} - \not{E}_x^{\text{obs}})^2}{2\sigma_{\not{E}_x}^2}\right) \exp\left(\frac{-(\not{E}_{y,i}^{\text{calc}} - \not{E}_y^{\text{obs}})^2}{2\sigma_{\not{E}_y}^2}\right). \tag{5.9}$$

If just the two leading jets are considered, there are two possible associations of jet and W boson to form each top quark. To calculate the neutrino weight the sum is taken over all permutations of jet assignments and neutrino momentum solutions of a particular choice of neutrino rapidity. The sum is also taken over all neutrino rapidity assumptions. For each top quark mass assumption the event kinematics is calculated for a grid of ten neutrino rapidities times ten antineutrino rapidities. The neutrino rapidities are chosen such that the same number of top events is expected for each of the η^{ν} ranges; that is, each η^{ν} value represents 10% of the top quark sample. This procedure is repeated for a range of assumed top masses from 80 GeV through 330 GeV, which results in a weight distribution versus a top quark mass hypothesis.

5.3.3 Detector Resolutions

The previous description of the weight curve calculation for a given event accounts for the detector resolution of the $\not{E}_T$ measurement, but it ignores the fact that jet and lepton energies may also be mismeasured. As a result, some configurations which are consistent with a top quark mass hypothesis are either not solvable at reconstruction

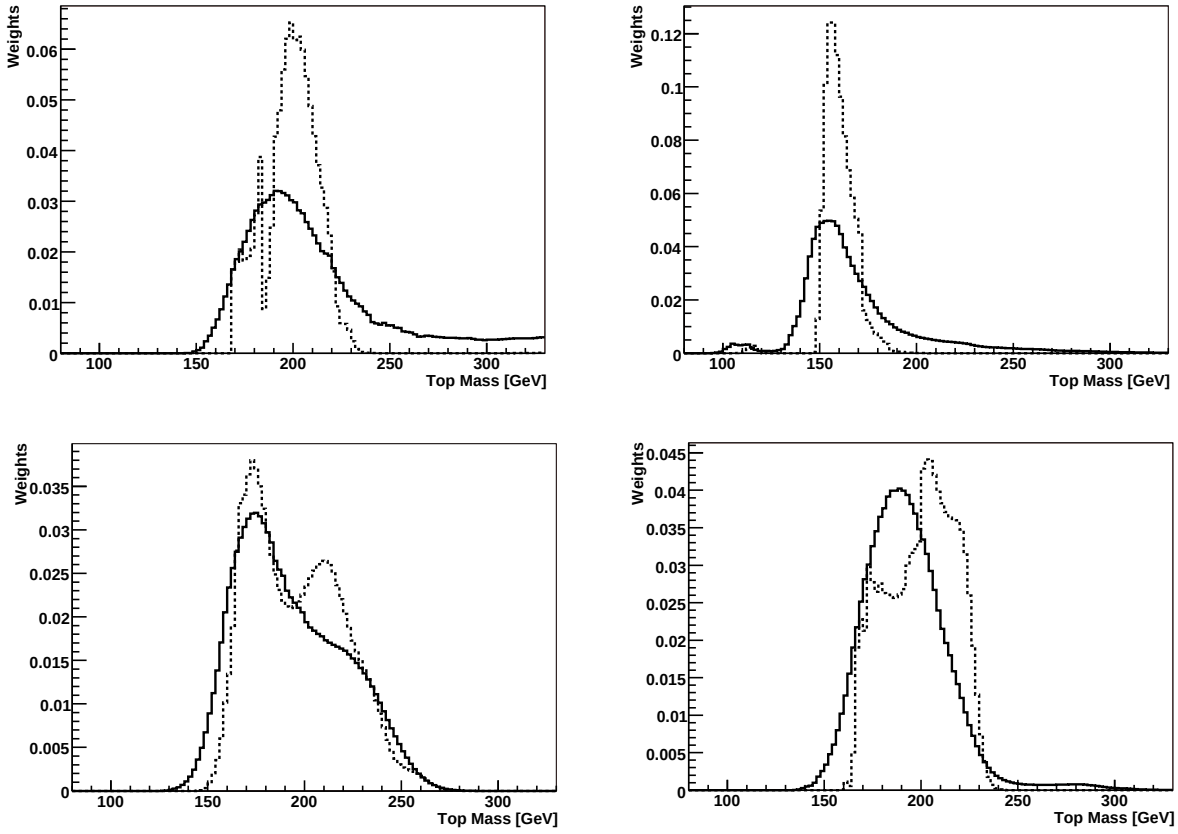

Figure 5.5: Normalized weight distributions for simulated example signal events with $m_{\text{top}} = 175$ GeV. The dashed distribution has no detector smearing, while the solid distribution has been smeared 150 times.

level or produce a weight that is incorrectly estimated. While this does not cause a change in the properties of weight distributions averaged over many events, it can have significant impact on single events. Detector resolutions are accommodated in the weight curve calculation in the following manner: for each configuration of each event attempted to be solved, 150 cases are calculated in which all jets and leptons are independently fluctuated according to their known resolutions. This way, 150 different samples of the event weight around the nominal jet and lepton measurements are obtained and summed. The effect can be seen for some example signal events in Figure 5.5. The weight curves become smoother and the range of top quark mass solutions increases. The number 150 was found to be sufficient to obtain stable and smooth weight curves as well as to have acceptable computation times. For data events, the number of smears is increased to 2000 to ensure that the result does not depend on fluctuations in the smearing.

Jet Resolution. The jet resolution in top quark events is taken from [65]. It is a function of transverse jet energy and detector η. There are separate parametrizations for light quark jets and b-jets.

Electron Resolution. The electron resolution is studied using $Z \to ee$ events [66]. The parametrization of the resolution depends on the electron p_T and rapidity. Different parametrizations are used for the central calorimeter and end cap calorimeter.

Muon Resolution. The resolution of muons is derived as a function of p_T and η. The parametrization can be found in [67].

Missing Transverse Energy Resolution. For each lepton or jet smearing the missing transverse energy is recalculated. For that reason, the smearing technique already accounts for missing transverse energy resolution effects coming from the resolution of the measured objects. In Equation 5.9 only remaining effects need to be considered with respect to the resolutions $\sigma_{\not E_x}$ and $\sigma_{\not E_y}$. These arise mainly from unclustered energy in the events. The resolution is measured in data and simulated events, and the dependency on unclustered energy is studied [68]. A $Z \to ee + 2$ jets data sample with high purity is selected. These events do not contain any neutrinos. The observed missing transverse energy is a measure for the resolution. The fraction originating from the unclustered energy $u\not E_T$ is calculated as the vector sum of $\not E_T$, the transverse electron momenta, and the jet momenta. Ideally, this sum would be zero. It is analyzed as a function of the square root of unclustered scalar transverse energy uSET defined as the scalar sum of the E_T of all calorimeter cells minus the fully corrected transverse electron and jet momenta. The result is shown in Figure 5.6. The data are compared to simulated $Z \to ee + 2$ jets events. The unclustered energy and resolution is well modeled. It is found that the resolution in x and y direction is the same. The dependency can be expressed in the following form:

$$\sigma_{\not E_x}(u\not E_x) = \sigma_{\not E_y}(u\not E_y) = 4.1 \text{ GeV} + 0.6(\sqrt{\text{uSET}} - 5.0 \text{ GeV}). \tag{5.10}$$

The resolutions $\sigma_{\not E_x}$ and $\sigma_{\not E_y}$ in Equation 5.9 are only parameters of the Neutrino Weighting method. They do not necessarily need to agree with the actual resolutions. Reasonably larger or smaller values still provide an unbiased top quark mass measurement, but with a different sensitivity. That is why there is no systematic uncertainty associated with it.
The analyzes with the smaller dataset used a constant missing energy resolution of 10.9 GeV based on earlier studies [69].

The neutrino weight distributions are normalized to unity, after the smearing of all objects is performed, because the integral over a weight distribution does not contain information on the top quark mass or whether the event is more signal or background like. This can be demonstrated by looking at weight distributions of simulated signal events that are derived using the truth information instead of the reconstructed objects. The resolution smearing is omitted. The integral over the neutrino weight distribution varies by several orders of magnitudes, even though, all events are signal and are of the same quality.
Figure 5.7 shows neutrino weight distributions averaged over several simulated events

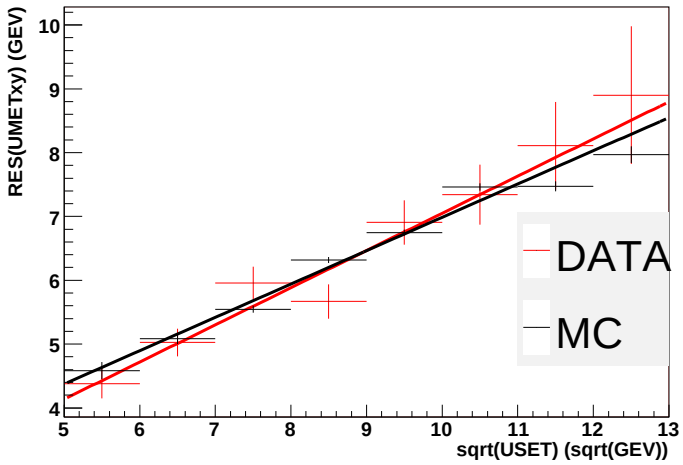

Figure 5.6: Dependence of resolution of unclustered missing energy on unclustered scalar missing energy for data and simulated $Z + 2$ jets events.

with top quark masses of 160 GeV, 175 GeV, and 190 GeV. Those distributions do not enter the analysis as such, but they illustrate the sensitivity of the weight distributions to the top quark mass. The peak and mean values of the distribution become larger with increasing top quark mass. Figure 5.8 shows the same distribution for two background processes. The peaks are at lower top quark masses and the distributions are much wider than for signal events, because the background is independent from the top quark mass.

Despite of the resolution smearing and testing of lots of η^{ν} and m_{top} hypotheses, not all signal events can be reconstructed by a valid kinematic solution as defined in Section 5.3.1, and obviously not all background events are consistent with the kinematics of a top quark event. The requirement that an event must fulfill at least one kinematical solution is in fact an additional selection criteria. The efficiencies for this requirement are given in Tables 5.5 to 5.7 for the different processes. The last column gives the observed efficiency in data. All data events have a kinematically allowed solution. These efficiencies are applied to the event yields when forming probability densities and ensembles. They are not included in the event yield tables of Section 5.2.3.

Table 5.5: Efficiencies for the requirement that an event must have a kinematical solution for the $e\mu$ channel.

$t\bar{t} \to e\mu$	WW	$Z \to \tau\tau \to e\mu$	observed
0.98 ± 0.01	0.95 ± 0.02	0.94 ± 0.02	1.0

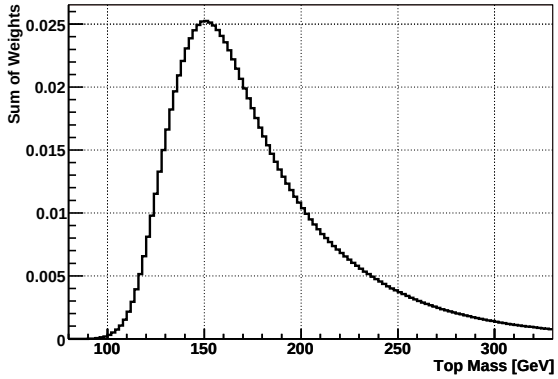

(a)

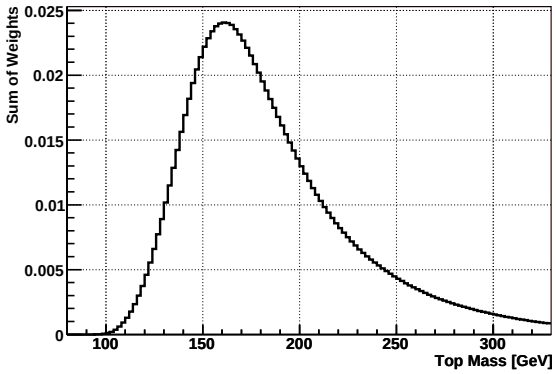

(b)

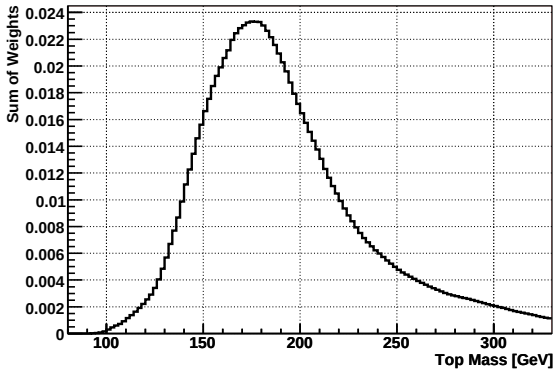

(c)

Figure 5.7: Averaged event weights for simulated $t\bar{t}$ samples of mass (a) 160, (b) 175, and (c) 190 GeV.

5.4 Probability Densities

The Neutrino Weighting algorithm provides for each event a weight distribution as a function of a top quark mass hypothesis. The higher the weight is, the better the re-

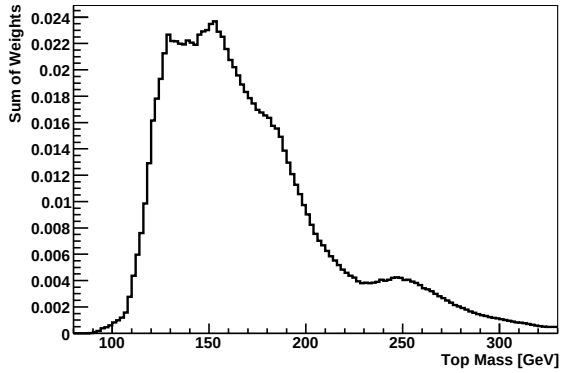

(a)

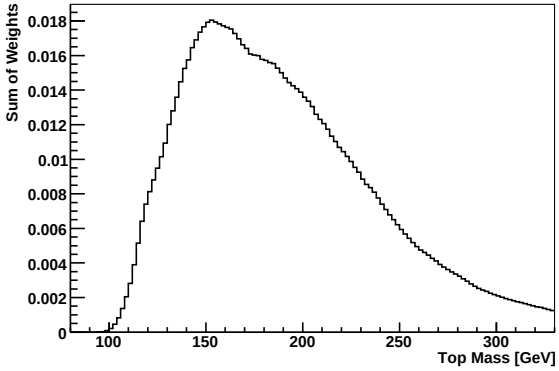

(b)

Figure 5.8: Averaged event weights for simulated $WW \to e\mu + \text{jets}$ samples (a), and $Z \to \tau\tau \to e\mu + \text{jets}$.

Table 5.6: Efficiencies for the requirement that an event must have a kinematical solution for the ee channel.

$t\bar{t} \to ee$	WW	$Z \to ee$	$Z \to \tau\tau$ $(\tau \to e)$	observed
0.98 ± 0.01	0.96 ± 0.03	0.86 ± 0.04	0.96 ± 0.01	1.0

Table 5.7: Efficiencies for the requirement that an event must have a kinematical solution for the $\mu\mu$ channel.

$t\bar{t} \to \mu\mu$	WW	$Z \to \mu\mu$	$Z \to \tau\tau$ $(\tau \to \mu)$	observed
0.98 ± 0.01	0.96 ± 0.04	0.90 ± 0.06	1.0	1.0

constructed event matches to a certain top quark mass hypothesis. Variables $\vec{w}$ that describe the shape of the weight distributions and are correlated to the top quark mass are used to form a signal probability density function $f_s(\vec{w}|m_{\text{top}})$. Accordingly, a back-

ground probability density function $f_b(\vec{w})$ is formed by applying the neutrino weighting algorithm to background samples. Both probability densities are normalized:

$$\int_{\text{phasespace}} \cdots \int f_s(w_1, \ldots, w_N, m_{\text{top}})\, d\text{w}_1 \ldots d\text{w}_N \equiv 1, \tag{5.11}$$

$$\int_{\text{phasespace}} \cdots \int f_b(w_1, \ldots, w_N)\, d\text{w}_1 \ldots d\text{w}_N \equiv 1, \tag{5.12}$$

where the dimension N of $\vec{w} = (w_1, \ldots, w_N)$ is the number of variables that describe the neutrino weight distributions. The integration is taken over the whole physically allowed region of the w_i.
In the following section the choice of these variables are discussed.

5.4.1 Choice of Variables

The maximum of the weight distribution and its mean are highly correlated with the top quark mass. The correlation is about 90%. Maximum and mean themselves are highly correlated, too, such that there is no gain by using both variables. Higher moments like the standard deviation, skewness, and so on have much smaller correlations with the top quark mass. The correlation of the standard deviation and the top quark mass is negligible. However, the resolution of the distribution of the mean variable is a function of the standard deviation variable. For a given top quark mass the correlation between mean and standard deviation is about 46%. The width of the mean distribution integrated over all standard deviation values is much wider than the width of the mean distribution for a certain standard deviation value. Therefore, by using the mean and the standard deviation the sensitivity to the top quark mass can be increased even though the standard deviation itself is not sensitive. I The correlation between maximum and standard deviation is much smaller, so that using the combination of maximum and standard deviation is less sensitive.
Instead of describing the shape by its maximum or its moments, the weight distribution can be described by N coarse bins. Since the weight distribution is normalized $N-1$ bins contain all the information on the shape. The higher N the more detailed the shape is described. But on the other hand N bins lead to a N-dimensional signal probability density $f_s(\vec{w}, m_{\text{top}})$, where the components of the $N-1$ dimensional vector $\vec{w}$ are the $N-1$ bins of the weight distributions. This N-dimensional space has to be filled by simulated events to model f_s and the calculation of f_s should be possible in a reasonable time. $N = 6$ is found to be a good value to have high sensitivity to the top quark mass and to keep the demand on the computation at a reasonable level.

5.4.2 Smoothing Techniques

Due to the limited available sample sizes of simulated events there are fluctuations in f_s and f_b that need to be smoothed out. An appropriate smoothing technique depends

on the distribution to be smoothed. The following two sections introduce two smoothing methods: a multi-dimensional fit and the "probability density estimation" (PDE) method [70].

Fitting Technique

The multi-dimensional fit method is illustrated by the example of using just the maximum of the neutrino weight distribution as sensitive information ($\vec{w}$ = maximum). In that case the signal probability density $f_s(\text{maximum}, \text{m}_{\text{top}})$ is two-dimensional. Figure 5.9 (left) shows the two-dimensional histogram of the obtained weight distribution maxima for generated top quark masses in the range between 155 GeV and 200 GeV. The histogram is normalized to respect Equation 5.11. It is smoothed by a two-dimensional fit that can be seen in Figure 5.9 (right). The fit function also respects Equation 5.11. The fitting technique is simple and results in a probability density function smoothed

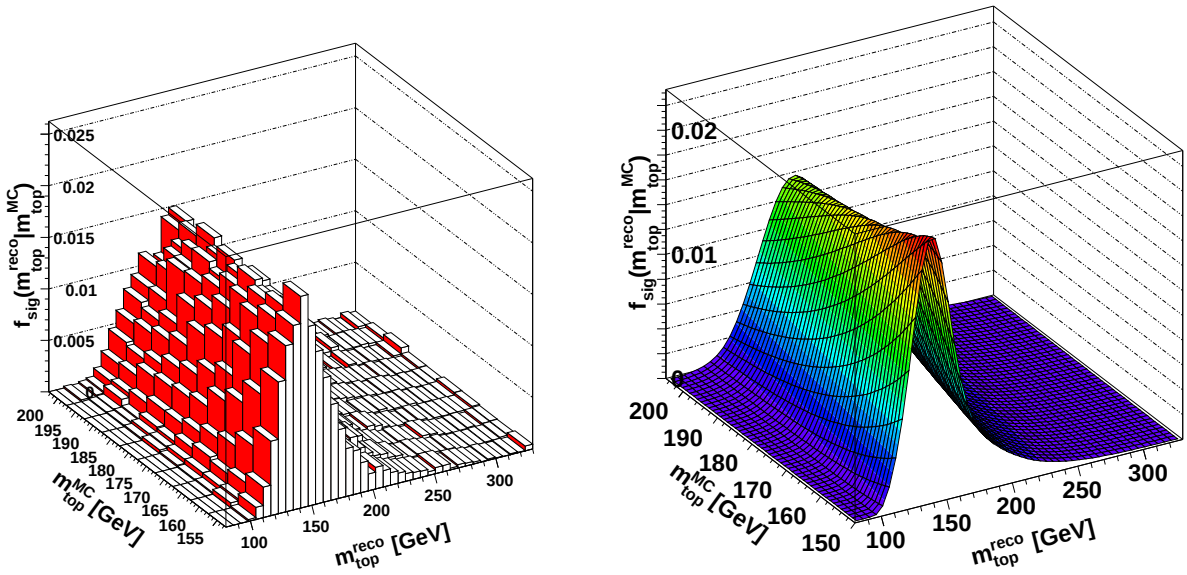

Figure 5.9: Signal probability density: Normalized distribution of maxima $m_{\text{top}}^{\text{reco}}$ of the Neutrino Weight distributions for different generated top quark masses $m_{\text{top}}^{\text{MC}}$ (left), and corresponding two-dimensional fitting result (right).

in both dimensions ($m_{\text{top}}^{\text{reco}}$ and $\text{m}_{\text{top}}^{\text{MC}}$). The normalization is intrinsically given by the fit function. However, this method can only be applied, if an appropriate fit function can be found, like in the example. In the general case, this is difficult and limits the method to be applicable only to low dimensional probability densities.
Figure 5.10 (left) shows a one-dimensional slice of f_s at a generated top quark mass of 170 GeV. Figure 5.10 (right) shows the one-dimensional fit to the maximum distribution of background events. Because there may be multiple backgrounds contributing to the background probability density, and because in general the number of simulated

background events for each background N_j^{MC} does not match the expected fractional contribution from the background $\bar{n}_{b,j}/\bar{n}_b$, the j^{th} background source is scaled by a weight factor b_j, given by:

$$\frac{b_j N_j^{\mathrm{MC}}}{\sum_{k=1}^{N_{\mathrm{sources}}} b_k N_k^{\mathrm{MC}}} = \frac{\bar{n}_{b,j}}{\bar{n}_b}. \tag{5.13}$$

The background probability density function $f_b(\mathrm{maximum})$ peaks at low top quark mass hypotheses. A detailed description of the top quark mass measurement using the maximum and the fitting technique can also be found in [69, 71]. In Section 5.8.1 the fitting technique is applied to a three-dimensional f_s.

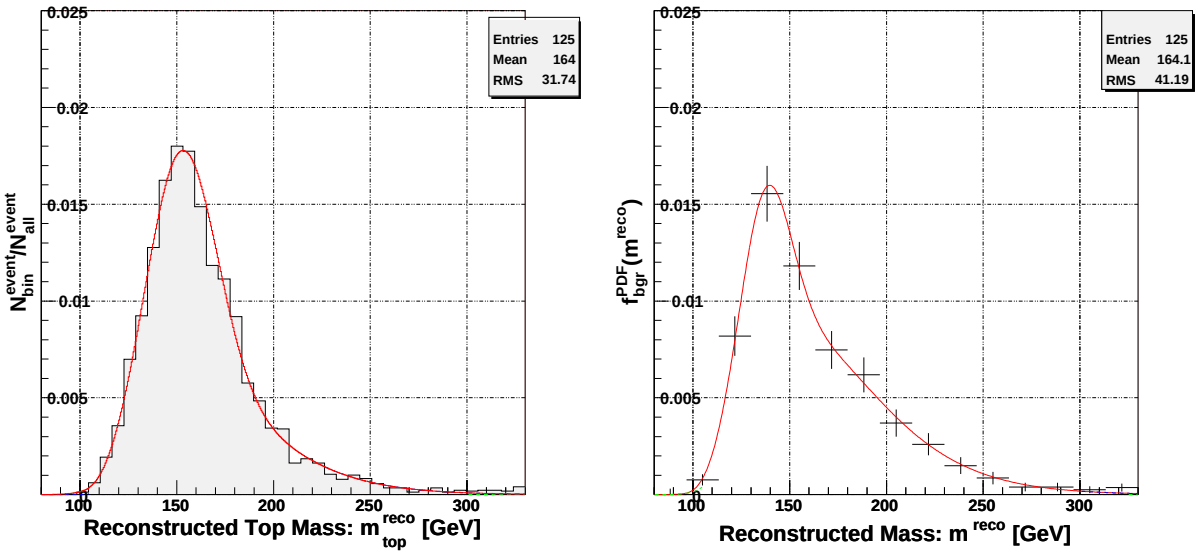

Figure 5.10: Slice of signal probability density: Normalized histogram and fit for the distribution of maxima $m_{\mathrm{top}}^{\mathrm{reco}}$ for a generated $m_{\mathrm{top}}^{\mathrm{MC}} = 170$ GeV (left). Background probability density: Normalized histogram and fit for the distribution of maxima $m_{\mathrm{top}}^{\mathrm{reco}}$ for background events (right).

Probability Density Estimation

PDE is a mathematical smoothing method [70] to estimate multivariate probability density functions based on distributions with a limited number of entries. An event is characterized by d variables that form a d-dimensional vector $\vec{w}$. A smoothed probability density function is obtained by replacing $\vec{w}$ of each simulated event by a Gaussian kernel function. Given a sample of $N^{\mathrm{MC}}(m_{\mathrm{top}})$ simulated events with the top quark mass m_{top}, the signal probability density function for an event with weight vector $\vec{w}_{\mathrm{ev}}$ can be

obtained by:

$$f_s(\vec{w}_{\mathrm{ev}}|m_{\mathrm{top}}) = \frac{1}{N^{\mathrm{MC}}(h\sqrt{2\pi})^d} \sum_{i=1}^{N^{\mathrm{MC}}(m_{\mathrm{top}})} \left[\prod_{j=1}^{d} \exp\left(-\frac{1}{2} \left(\frac{w_{\mathrm{ev}}^j - w_i^j}{h} \right)^2 \right) \right]. \tag{5.14}$$

The free parameter h is the width of the Gaussian kernel. The way h is chosen is described in the next subsection. The background probability density function is calculated similar to Equation 5.14. The relative scale factors b_j of the different background sources, defined in Equation 5.13, are included. The overall background probability density then reads:

$$f_b(\vec{w}_{\mathrm{ev}}) = \frac{1}{(h\sqrt{2\pi})^d} \frac{1}{\sum_{k=1}^{N_{\mathrm{sources}}} b_k N_k^{\mathrm{MC}}} \sum_{k=1}^{N_{\mathrm{sources}}} b_k \sum_{i=1}^{N_k^{\mathrm{MC}}} \left[\prod_{j=1}^{d} \exp\left(-\frac{1}{2} \left(\frac{w_{\mathrm{ev}}^j - w_i^j}{h} \right)^2 \right) \right]. \tag{5.15}$$

Choice of the Smoothness Parameter *h*. A good choice of the smoothness parameter h is essential for the PDE method. A too small h yields a not smooth probability density function. This leads to high fluctuations in the maximum likelihood function containing f_s and f_b. On the other hand with a too large value of h sensitivity for the measurement is lost.[3] The parameter h needs to be adapted depending on the availabe statistics of the simulated events and on the shape of the distributions which shall be smoothed. It is tuned empirically by performing ensemble tests and optimizing the agreement between measured and true quantity.

Normalization of the Probability Density Functions. Equations 5.14 and 5.15 are normalized to unity, as long as the components of the vector $\vec{w}$ are meaningful in the range $-\infty, \infty$. However, often there are boundary conditions limiting the physically allowed region. If for example the components of $\vec{w}$ are coarse bins of the normalized neutrino weight distribution, then $w_i \in [0, 1]$ will hold, because the neutrino weight distributions are normalized. If Gaussian kernel functions are used to describe the w_i distributions, then the tails of the Gaussian kernels will spill out of this interval and the normalization of the probability density function will be too small. Figure 5.11 gives a simple example. One entry at $w_i = 0.1$ is smoothed by a normalized Gaussian. A significant part of the function lies outside the interval $[0, 1]$ and would not be used for the normalization. This would dilute the result. A solution to obtain normalized probability densities is to use boundary kernels, as suggested in [72]. The tail in the not allowed region is mirrored at the boundary, and then added to the Gaussian. In the example, the boundary is at $w_i = 0$, and the mirrored area is marked as hashed area in the positive region. The normalized boundary kernel including the mirrored contribution is shown as a dashed curve. This method is applied to the neutrino weighting method the first time and has lead to an improvement of the sensitivity to the top quark mass [69].

[3] In the extreme case of $h \to \infty$ the resulting distribution is flat and does not contains any information on m_{top}.

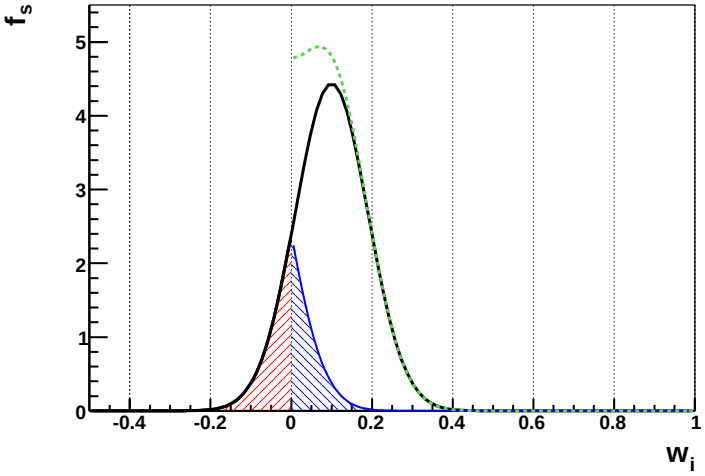

Figure 5.11: Example of the construction of boundary kernel functions (see text).

Correlation of Variables. The multidimensional Gaussian kernel does not reflect possible correlations between the variables w_i. In case of the choice of the coarse bins as w_i, there is a high correlation between adjacent bins. Either the kernel function, or the used variables can be transformed such that their correlations are the same. The second approach is simpler. In general the correlations of the w_i is different for signal and background events. But from linear algebra it is known that there always exists a unitary transformation that simultaneously diagonalizes the covariance matrices for signal and background. For the transformed variables w_i' an individual smoothing parameter h_i for each dimension i can be chosen that is proportional to the standard deviation of the distribution of the w_i'. The decorrelation of the w_i was studied, but found to not improve the results significantly. The construction of boundary kernels becomes more complex as the boundaries of the w_i' are transformed hyperplanes in the i dimensional space. Therefore, it was not used in the analysis.

5.5 Maximum Likelihood Method

After having modeled the signal probability density function $f_s(\vec{w}, m_{\text{top}})$ and background probability density function $f_b(\vec{w})$ with either of the smoothing techniques, the top quark mass is extracted using a maximum likelihood method, see for example [73]. The likelihood $\mathcal{L}$ consists of three parts. The first part is a constraint requiring that the sum of the number of signal events n_s and the number of background events n_b agree within Poissonian fluctuations with the number of observed events N:

$$\mathcal{L}_{\text{poisson}}(n_s + n_b, N) \equiv \frac{(n_s + n_b)^N e^{-(n_s+n_b)}}{N!}. \tag{5.16}$$

The second part is a Gaussian constraint introduced to require agreement between the number of background events n_b and the number of expected background events $\bar{n}_b$ within Gaussian fluctuations, where the sigma of the Gaussian is given by the uncertainty σ_b on $\bar{n}_b$:

$$\mathcal{L}_{\text{gaus}}(n_b, \bar{n}_b, \sigma_b) \equiv \frac{1}{\sqrt{2\pi}\sigma_b} e^{[-(n_b-\bar{n}_b)^2/2\sigma_b^2]}. \tag{5.17}$$

The third part contains the actual dependency on the top quark mass. The total likelihood is given by:

$$\mathcal{L}(\vec{w}_1, \ldots, \vec{w}_N, \bar{n}_b, N \mid m_{\text{top}}, n_s, n_b) = \\ \mathcal{L}_{\text{gaus}}(n_b, \bar{n}_b, \sigma_b) \times \mathcal{L}_{\text{poisson}}(n_s + n_b, N) \times \prod_{i=1}^{N} \frac{n_s f_s(\vec{w}_i, \mid m_{\text{top}}) + n_b f_b(\vec{w}_i)}{n_s + n_b}. \tag{5.18}$$

When performing a likelihood maximization, it is convenient to minimize the negative logarithm of the likelihood function, rather than maximizing $\mathcal{L}$ itself.
If f_s and f_b are described by a fit function, then $-\log\mathcal{L}$ will be given by an analytic expression. It can be minimized simultaneously with respect to m_{top}, n_s, and n_b. This is done by a C++ implementation of MINUIT [42,74]. The result of this minimization is the top quark mass estimate, $\hat{m}_{\text{top}}$. Its statistical uncertainty $\hat{\sigma}_{m_{\text{top}}}$ is given by half of the distance between the points at which the $-\log\mathcal{L}$ value is 0.5 units greater than its minimum value. This is also calculated by MINUIT.
If f_s and f_b are described by the PDE method the minimization has to be done in two steps, since f_s can only be evaluated at discrete generated top quark masses. In the first step, $-\log\mathcal{L}(\vec{w_1}, \ldots, \vec{w_N}, \bar{n}_b, N \mid m_{\text{top}}, n_s, n_b)$ is minimized with respect to n_s and n_b. This is done for each simulated signal sample with different m_{top} by MINUIT. The obtained $-\log\mathcal{L}(m_{\text{top}})$ points are plotted versus the top quark mass. The second step of the minimization is a quadratic fit to this plot. The minimum of the parabola yields the estimate $\hat{m}_{\text{top}}$ and the width of the parabola its statistical uncertainty $\hat{\sigma}_{m_{\text{top}}}$.
The combination of all three dilepton channels is done by multiplying the likelihoods of every channel. This is equivalent to adding up the negative log likelihoods of every channel:

$$-\log\mathcal{L} = \sum_c (-\log\mathcal{L}^c) \ , \tag{5.19}$$

where c denotes the dilepton channel: $c \in \{e\mu, ee, \mu\mu\}$. The combined negative log likelihood $-\log\mathcal{L}$ is minimized simultaneously with respect to seven variables: m_{top}, n_s^c and n_b^c.

5.6 Calibration and Ensemble Tests

The performance and precision of the method is tested in pseudo experiments also called ensemble tests. An ensemble is a set of simulated events of the same size as the selected dataset. The composition of signal and background events corresponds to the expected

composition in data. Ensembles are created by randomly drawing simulated events out of a large ensemble pool. The number of background events of each source is Poisson-fluctuated around the expected yields. The remaining events in the ensemble are filled up with signal events. This way there is no explicit use of the $t\bar{t}$ production cross section, which is a function of the top quark mass. Resampling is applied to make maximal use of the available statistics of the ensemble pools. This means events are drawn with replacement, allowing an event to occur in several ensembles, and more than once in the same ensemble. Ensemble tests simulate several hundred independent pseudo-experiments. They provide a calibration of the method and an estimate of the expected statistical uncertainty. A possible bias of the top quark mass estimator can be corrected for. The resampling technique provides no additional information on the mean of the estimator, compared to ensemble tests where each event is used just once. But the estimation of the average statistical uncertainty is improved. The correlation between different ensembles that share events leads to an underestimation of the statistical uncertainty. In the extreme case of two identical ensembles, no new information is added by the second ensemble, which is treated as an independent measurement. Ensembles containing two or more identical events lead to an overestimation of the statistical uncertainty. It can be shown that those two biases exactly cancel [75].
A calibration curve for the top quark mass estimator can be obtained, because the true top quark mass is known for ensembles. The generated input top quark mass $m_{\mathrm{top}}^{\mathrm{gen}}$ is parametrized as a function of the output top quark mass $\hat{m}_{\mathrm{top}}$. A linear curve is sufficient as parametrization for all applied methods:

$$\hat{m}_{\mathrm{top}} = (m_{\mathrm{top}}^{\mathrm{gen}} - 175\ \mathrm{GeV}) \cdot \mathrm{slope} + \mathrm{offset} + 175\ \mathrm{GeV}. \tag{5.20}$$

The data measurement is corrected for deviations of the slope from unity and a non-vanishing offset.
For each ensemble the statistical uncertainty $\sigma(m_{\mathrm{top}})$ is estimated. The correctness of the average estimate is cross checked by the pull distribution. The pull is defined as:

$$\mathrm{pull} = \frac{\mathrm{m_{top}} - \mathrm{m_{top}^{gen}}}{\sigma(\mathrm{m_{top}})}, \tag{5.21}$$

where $m_{\mathrm{top}} \pm \sigma(m_{\mathrm{top}})$ is the measured top quark mass and uncertainty after the calibration. The ideal pull distribution has a Gaussian shape with the mean at zero and a width of one. A pull width larger (less) than one indicates an underestimated (overestimated) statistical uncertainty. The uncertainty of the data measurement is corrected for deviations of the pull width from one.
The mean of the distribution of calibrated and pull-corrected statistical uncertainties yields the expected statistical uncertainty. From this distribution the probability for the observed statistical uncertainty of the data measurement can be obtained.

5.7 Analysis of the 835 pb^{-1} Dataset

In summer 2006 the top quark mass was measured with a dataset of size corresponding to 835 pb^{-1} in the electron-muon final state. Three approaches of the Neutrino Weighting

Method were applied that differ in the choice of variables for the probability densities, and in the smoothing technique:

- *Binned Method:* This approach uses five coarse bins of the neutrino weight distribution to form a six-dimensional signal probability density function $f_s(w_1, \ldots, w_5|m_{\text{top}})$. f_s and f_b are smoothed by the PDE method. This version of the analysis is similar to earlier DØ analyzes in Run I [62–64] and Run II [76–78].

- *Moments Method:* The Moments Method uses the mean and standard deviation (rms) of the neutrino weight distribution. The signal probability density is three dimensional: $f_s(\text{mean}, \text{rms}|\text{m}_{\text{top}})$. The smoothing is also done with PDE.

- *Maximum Method:* This method was developed in parallel to the other approaches to study systematic uncertainties of the modeling of probability densities with a simplified method that uses just one variable, the maximum, to describe the neutrino weight distribution. $f_s(\text{maximum}|\text{m}_{\text{top}})$ is smoothed by a two-dimensional fit, described in Section 5.4.2, and in [71].

5.7.1 Ensemble Tests and Calibration

Ensemble tests as described in the previous section are performed for all three approaches. The optimal smoothing parameter h for the Binned Method is found to be $h = 0.10$ for f_s, and $h = 0.15$ for f_b. For the Moments Method h is chosen to be 0.33 times the standard deviation of the mean or rms distribution for f_s and f_b.
All signal and background samples are generated by PYTHIA. Signal samples with generated top quark masses between 155 GeV and 200 GeV in steps of 5 GeV are available. For each method 500 ensembles are formed, each containing 28 events, according to Table 5.1. In Figure 5.12 randomly chosen examples of $-\log\mathcal{L}$ curves are given for the Binned Method with different generated m_{top}. Figure 5.13 shows examples for the Moments Method. The assigned error bars are constant and have no impact on the positions of the minima. The observed fluctuations of the entries of the $-\log\mathcal{L}$ distributions are a consequence of fluctuations in the probability densities, and not of the choice of ensembles. This is why there are patterns in the fluctuations. Different ensembles are evaluated with the same probability densities. The PDE method smoothes only fluctuations in the bin-, mean, or rms-variable, but there is no smoothing between samples of different top quark masses. The fitting technique does not have this restriction and therefore the likelihood curves of the Maximum Method are smooth without any fluctuations. The Maximum Method minimizes the $-\log\mathcal{L}$ distribution in two steps the same way as the methods smoothed by PDE, because the ensemble testing was initially developed for the PDE method. A cubic fit instead of a quadratic fit is applied.
The calibration curves for all three methods are shown in Figure 5.14. The plots on the left-hand side show the input versus the output top quark mass together with the linear fit given by Equation 5.20. The right-hand side shows the same calibration, but with the output minus the input top quark mass on the y-axis. This view enlarges the statistical fluctuations and error bars. The very first and very last entry at a top quark

mass of 155 GeV and 200 GeV are not included in the fit range. For these input top quark masses the $-\log\mathcal{L}$ fits perform worse, because there are only entries for one half of the parabola left ($\leq$ 200 GeV) or right ($\geq$ 155 GeV) from the expected minimum, respectively. All three methods provide an almost unbiased estimation of the top quark mass, i.e. the slope of the calibration is approximately one and the offset is approximately zero. The first two columns of Table 5.8 summarize the results of the linear fits.

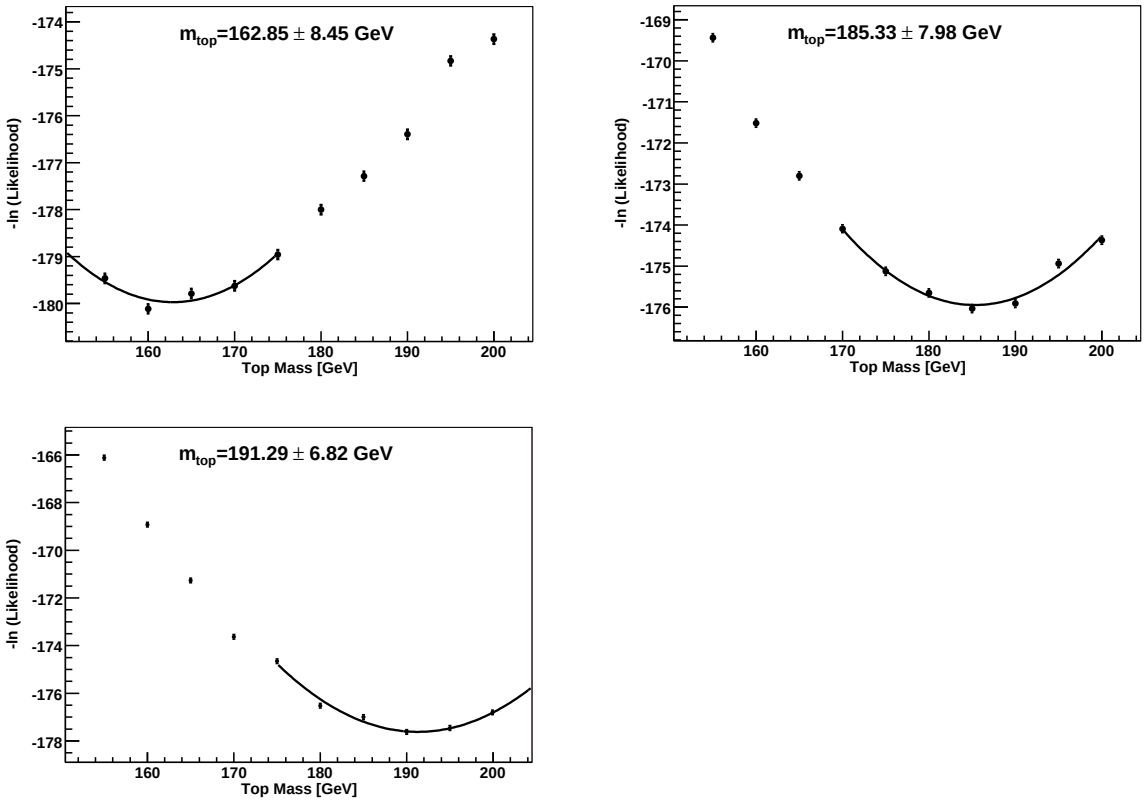

Figure 5.12: **Binned Method**: Example quadratic fits to the negative log likelihood distributions for ensembles with signal and background events. The generated top quark masses are 160 GeV (top left), 175 GeV (top right), and 190 GeV (bottom left).

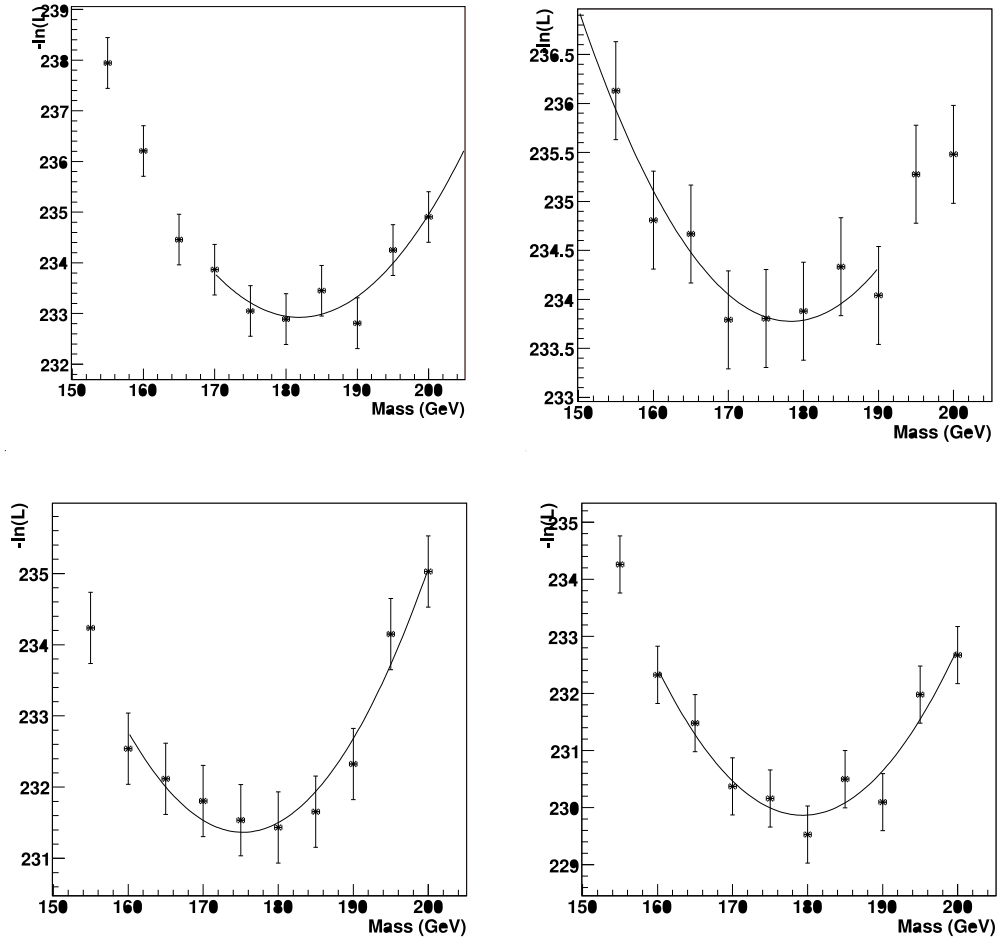

Figure 5.13: **Moments Method**: Example quadratic fits to the negative log likelihood distributions for ensembles with signal and background events. The generated top quark masses are 175 GeV.

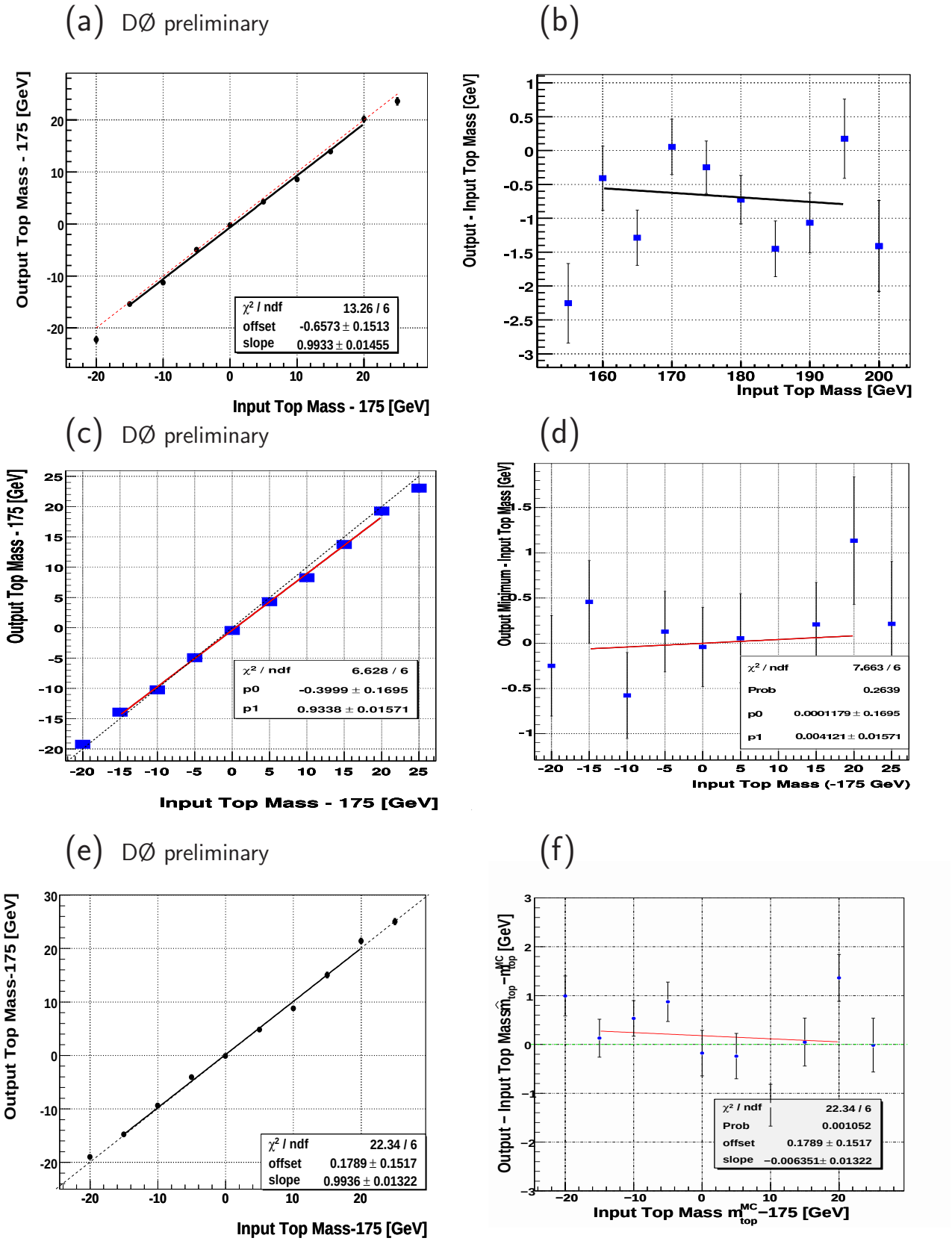

Figure 5.14: Calibration Curves: top quark mass estimate and top quark mass estimate minus the generated input top quark mass as a function of the generated input top quark mass for the **Binned Method** (a), (b), **Moments Method** (c), (d), and **Maximum Method** (e), (f).

Figure 5.18 (left) shows the pull distributions for $m_{\text{top}} = 175$ GeV for the three methods. On the right-hand side the fitted pull width as a function of m_{top} is shown. The average pull width is determined by a constant fit. The results are given in column three of Table 5.8. The Binned Method overestimates the statistical uncertainty. The small pull width of 0.86 (see Figure 5.18 (b)) results from the systematic fluctuations in the $-\log\mathcal{L}$ distributions. They lead to too wide-open parabolas. This effect is smaller for the Moments Method even though it also uses PDE.

5.7.2 Results for Binned, Moments, and Maximum Method

The three methods are applied to the 28 candidate data events. The results of the likelihood fits are shown in Figure 5.15. The top quark mass estimates and uncertainties are corrected to account for the calibration from ensemble tests and the non-unit pull widths.
The measured top quark mass after calibration for the three listed method yields:

$$\textbf{Binned Method :} \quad m_{\text{top}} = 173.6 \pm 6.7 \text{ (stat.) GeV} \tag{5.22}$$

$$\textbf{Moments Method :} \quad m_{\text{top}} = 171.6 \pm 7.9 \text{ (stat.) GeV} \tag{5.23}$$

$$\textbf{Maximum Method :} \quad m_{\text{top}} = 165.7 \pm 9.7 \text{ (stat.) GeV} \tag{5.24}$$

The observed statistical uncertainties are consistent with the expected ones, as can be seen in Figure 5.16. The distributions show the statistical uncertainties of 500 ensemble tests for all three methods. The arrows mark the observed uncertainty. The mean of the distributions is summarized in the last column of Table 5.8.
The statistical correlation between the Maximum Method and the Binned Method has been evaluated. For this purpose 200 pseudo-experiments with 28 events each, using identical event ensembles were analyzed with the two methods. For the sake of simplicity, pure signal events have been considered. On the left-hand side of Figure 5.17 a scatter plot of the output top masses before calibration for the both methods is displayed. As expected, the points are distributed in an elliptical cloud along the bisector. The right-hand side shows the difference between output top masses. The distribution has a standard deviation of 3.8 GeV and a mean consistent with zero. The correlation between the Maximum Method and the Binned Method is found to be 0.87.

The systematic uncertainties of the measurements are discussed in Section 5.9.

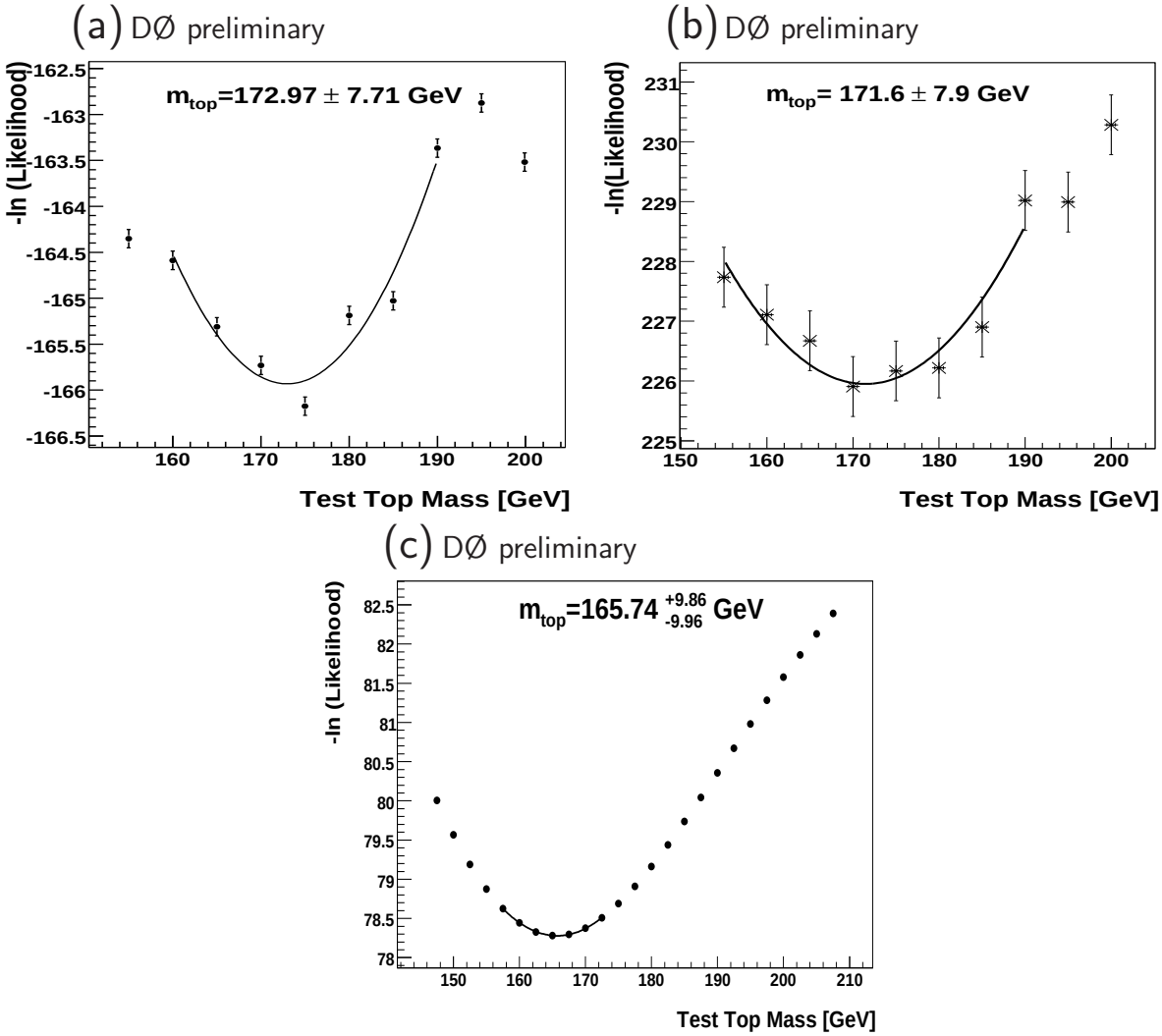

Figure 5.15: The negative logarithmic likelihood for the 28 data events in the $e\mu$ channel for the 835 pb^{-1} dataset for the **Binned Method** (a), **Moments Method** (b) and **Maximum Method** (c). The statistical uncertainties are given before calibration.

Method	slope	offset [GeV]	⟨pull width⟩	$\langle\sigma_{m_{\mathrm{top}}}\rangle$ [GeV]
Binned Method	0.99 ± 0.01	-0.66 ± 0.15	0.86 ± 0.01	8.2
Moments Method	0.93 ± 0.02	-0.30 ± 0.18	0.97 ± 0.01	9.2
Maximum Method	0.99 ± 0.01	0.18 ± 0.15	0.99 ± 0.01	8.8

Table 5.8: Slope and offset of the calibration curves in Figure 5.14, the pull width after calibration, and the mean value of the statistical uncertainty after calibration and correction for the pull width for the three methods.

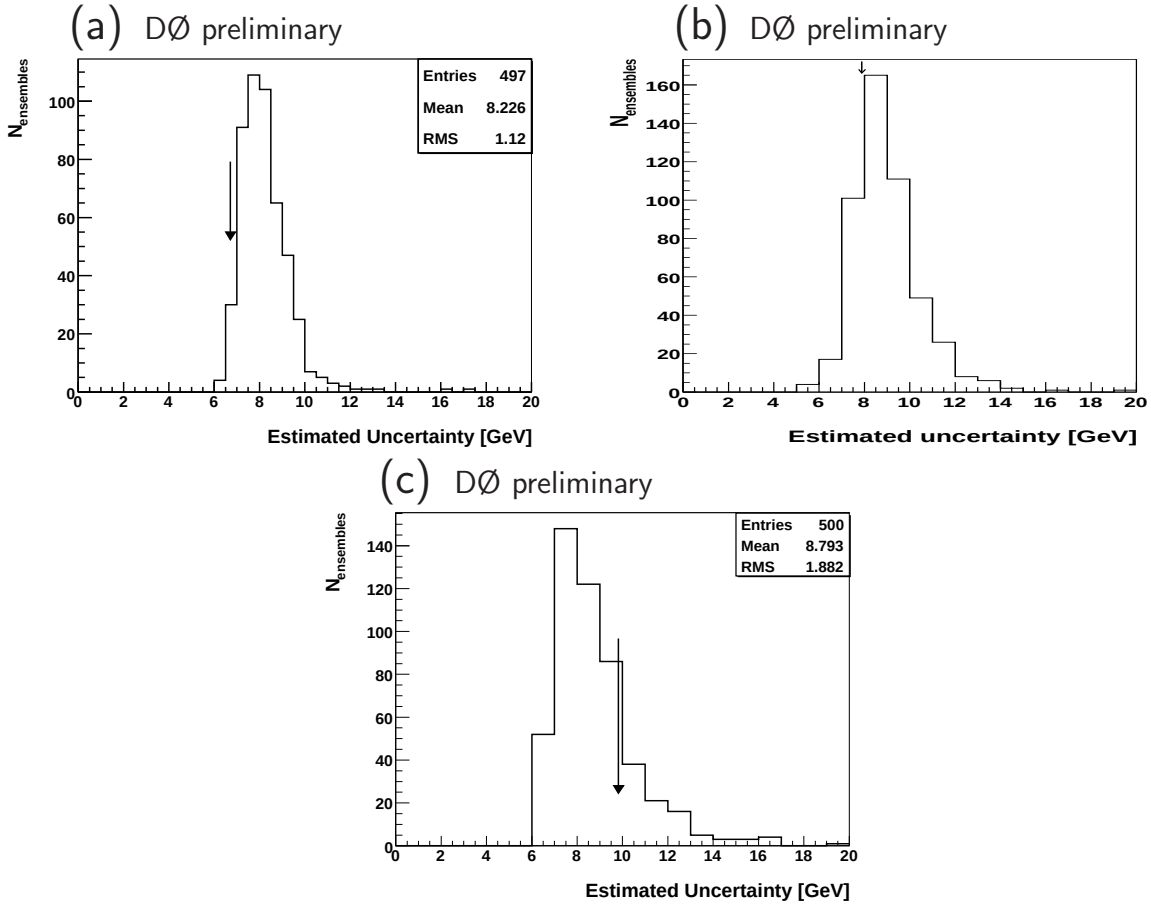

Figure 5.16: Distribution of statistical uncertainties after correcting for the pull width for m_{top}=175 GeV. Results are shown for the **Binned Method** (a), the **Moments Method** (b) and the **Maximum Method** (c).

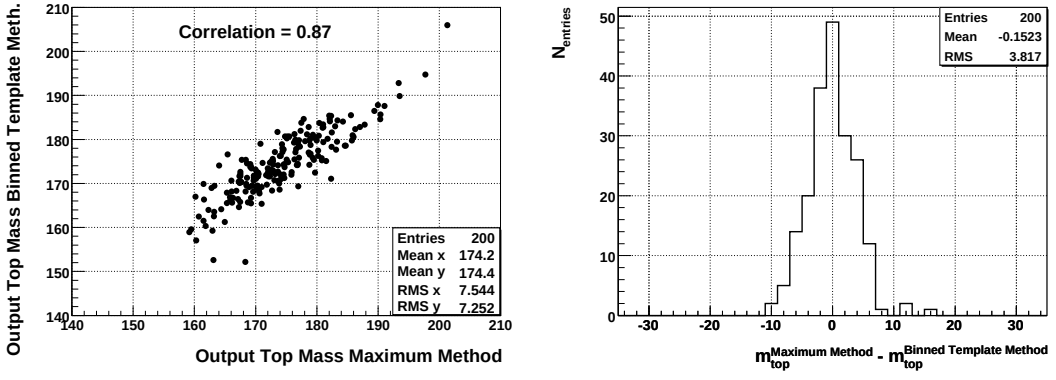

Figure 5.17: The statistical correlation between the Maximum Method and the Binned Method: on the left the output m_{top} of the Maximum Method versus the output m_{top} of the Binned Method is displayed, on the right their difference for the same pseudo-experiments. All mass results are before calibration.

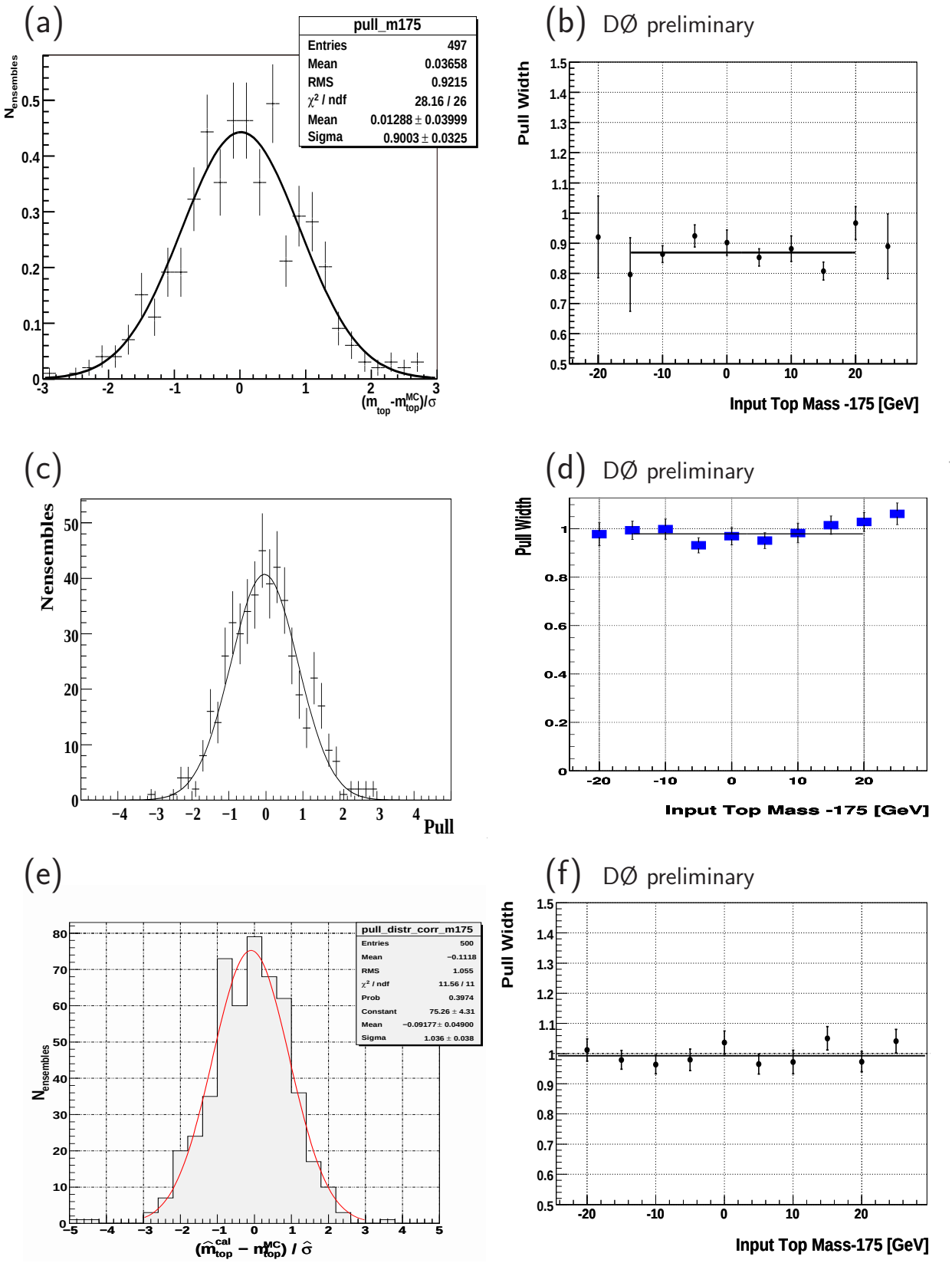

Figure 5.18: Pull distributions at $m_{\text{top}} = 175$ GeV for the **Binned Method** (a), **Moments Method** (c), and **Maximum Method** (e). Pull width distributions as a function of the generated m_{top} for the **Binned Method** (b), **Moments Method** (d), and **Maximum Method** (f).

5.7.3 Conclusions from Binned, Moments, and Maximum Method

All three methods provide top quark measurements with a comparable sensitivity. The results are limited by statistics. Main improvements are expected from analyzing more data and all dilepton channels, not just the electron-muon channel. The Binned Method yields the smallest expected and observed statistical uncertainty, as it uses five variables to describe the shape of the neutrino weight distributions. However, the sensitivity of the other two methods using just one or two variables is close to that of the Binned Method. The PDE technique introduces systematic fluctuations in the likelihood distributions. Those fluctuations are partly smoothed by the quadratic fit of the $-\log\mathcal{L}$ distribution. An average bias is corrected by the calibration curves, but for single ensembles there remains a systematic uncertainty that will play a role for measurements with smaller statistical uncertainties. The three methods are highly correlated, because the event selection and reconstruction of the kinematics by the neutrino weighting algorithm are identical.
All these considerations led to the development of a new method that has been applied to the dataset of 1.05 fb^{-1} available in winter 2007. The choice of variables is the same as in the Moments Method, but the smoothing is done with a fitting technique instead of the PDE method. This way there are no systematic uncertainties originating from fluctuations in the likelihood curve, and at the same time there is a high sensitivity to the top quark mass, as the signal probability density is three-dimensional, not just two-dimensional as in the Maximum Method.

5.8 Analysis of the 1.05 fb^{-1} Data Set

In winter 2007 the top quark mass has been measured with a data set of 1.05 fb^{-1} in all three dilepton final states. The following subsection describes the modeling of the signal and background probability densities $f_s(\text{mean}, \text{rms}|\text{m}_{\text{top}})/\text{f}_\text{b}(\text{mean}, \text{rms})$ by a three/two-dimensional fit.

5.8.1 Fitting of Probability Densities

Three-dimensional Signal Probability Density. The signal probability density function $f_s(\text{mean}, \text{rms}|\text{m}_{\text{top}})$ is modeled by a fit to the three-dimensional histogram of the mean, rms, and m_{top} variables. An applicable three-dimensional fit function is found empirically. It fulfills Equation 5.11 and is given by Equations 5.25-5.27:

$$m := p_0 + p_1(\text{rms} - 36\ \text{GeV}) + \text{p}_2(\text{m}_{\text{top}} - 175\ \text{GeV}) \tag{5.25}$$

$$\sigma := p_3 + p_4(\text{rms} - 36\ \text{GeV}) + \text{p}_5(\text{m}_{\text{top}} - 175\ \text{GeV}) \tag{5.26}$$

$$
\begin{aligned}
f_s(\text{mean}, \text{rms}, \text{m}_{\text{top}}) = {} & p_6 \cdot (\text{rms} + \text{p}_{14})^{\text{p}_7} \exp(-\text{p}_8(\text{rms} + \text{p}_{14})^{\text{p}_9}) \\
& \times \left[(1 - p_{10}) \frac{1}{\sigma\sqrt{2\pi}} \exp(-\frac{(\text{mean} - \text{m})^2}{2\sigma^2}) \right. \\
& + p_{10} \cdot \frac{p_{12}^{1+p_{13}}}{\Gamma(1 + p_{13})} (\text{mean} - \frac{\text{m}}{\text{p}_{11}})^{\text{p}_{13}} \exp(-\text{p}_{12}(\text{mean} - \frac{\text{m}}{\text{p}_{11}})) \\
& \left. \times \Theta(\text{mean} - \frac{\text{m}}{\text{p}_{11}}) \right] \\
& \times \left[\int_{p_{14}}^{\infty} p_6 \cdot \text{r}^{\text{p}_7} \exp(-\text{p}_8 \text{r}^{\text{p}_9}) \text{dr} \right]^{-1}
\end{aligned}
\tag{5.27}
$$

Equations 5.25 and 5.26 express the correlations between the three variables. The first line of Equation 5.27 parametrizes the dependency on the rms-variable. The second and third line, a Gaussian plus the first derivative of the Γ-function ($d\Gamma$), describe the dependency on the mean variable. The core is described by the Gaussian, and the right tail by the $d\Gamma$ function. The mean of the Gaussian is correlated to the root of the $d\Gamma$ function via the parameter p_{11}. The Heaviside function Θ sets $d\Gamma = 0$ left of its root. To fulfill the normalization constraint, the one-dimensional integral given by the last line of Equation 5.27 has to be evaluated. This is done numerically while fitting.
It turned out that this choice of parametrization can be applied to all three dilepton channels. The obtained parameters are summarized in Table 5.9. The parameter p_6 could have been omitted, as it has no effect on the shape or normalization. The small value of p_{14} is a consequence of the small value of p_6. A non-vanishing value of p_{14} is important to allow the function to be greater than zero for rms equals zero.

The uncertainties of the 15 fit parameters suggest that a fit function with less parameters could be found. However, the fits are stable and the uncertainties on the fit parameters do not enter the analysis. A possible bias on the measured top quark mass due to the choice of the parametrization of f_s will be measured and calibrated using ensemble tests as discussed in Section 5.6. In Appendix C, D, and E many two-dimensional views of the fit result can be found for the $e\mu$, ee, and $\mu\mu$ channels, respectively. The smoothing by the fit performs very well, as can be seen in the examples of one-dimensional slices of f_s shown in Figure 5.19. Plot (a) and (b) show the dependence on the mean at a constant rms and m_{top}, and plot (c) and (d) show the dependence on m_{top} at a constant mean and rms. The fluctuations that can be seen in (c) and (d) can only be smoothed by the fitting technique and not by the PDE method, as explained before.

Two-dimensional Background Probability Density. The background probability density function $f_b(\text{mean}, \text{rms})$ is obtained by filling the available statistics of simulated background events into a two dimensional histogram (mean versus rms). A relative weight for background events of a certain process is given by the fractional yield of the

	$e\mu$			ee			$\mu\mu$		
p_0	194.5	±	0.15	196.5	±	0.27	196.4	±	0.0048
p_1	1.234	±	0.0059	1.185	±	0.0098	1.332	±	3.2e-05
p_2	0.6315	±	0.005	0.7079	±	0.0084	0.6386	±	0.00033
p_3	22.96	±	0.092	25.03	±	0.19	24.29	±	0.0049
p_4	0.1703	±	0.0045	0.1833	±	0.0083	0.2168	±	0.00025
p_5	0.1942	±	0.0043	0.1839	±	0.0069	0.1521	±	0.00039
p_6	-2.167e-09	±	6.6e-09	-4.979e-08	±	8.9e-08	-8.537e-10	±	1.5e-08
p_7	0.489	±	0.0068	0.238	±	0.013	0.839	±	0.00036
p_8	0.0002903	±	2.2e-05	0.001489	±	0.00019	0.002092	±	5.6e-07
p_9	2.321	±	0.018	1.911	±	0.03	1.879	±	6.7e-05
p_{10}	0.284	±	0.0066	0.2227	±	0.0099	0.1606	±	0.00025
p_{11}	1.423	±	0.0086	1.387	±	0.012	1.321	±	4.6e-07
p_{12}	0.05286	±	0.0011	0.0371	±	0.0018	0.02618	±	2.3e-05
p_{13}	2.286	±	0.098	1.442	±	0.13	0.585	±	0.0012
p_{14}	3.816e-09	±	6.3e-07	0.0008152	±	0.00057	1.037e-06	±	1.6e-06

Table 5.9: Fitted parameters for the three dilepton channels for the signal probability functions f_s.

total expected background yield, given by Equation 5.13. The histogram is normalized and f_b is smoothed by a two-dimensional fit. Figures 5.20, 5.21, and 5.22 show the histograms on the left-hand side and the fit results on the right-hand side for the three channels. The modeling of the background probability density function is limited by the available amount of simulated background events passing all selection criteria.
A simple background fit function is chosen for all three dilepton channels. It allows a linear transformation of the mean and rms variables and then fits a two-dimensional Gaussian to the transformed variables:

$$f_b(\text{mean},\text{rms}) = \frac{\exp\left(-\frac{(\mathrm{p_4 mean} + \mathrm{p_5 rms} - \mathrm{p_0})^2}{2\mathrm{p_1^2}} - \frac{(\mathrm{p_6 mean} + \mathrm{p_7 rms} - \mathrm{p_2})^2}{2\mathrm{p_3^2}}\right)}{\int_0^\infty \int_0^\infty \exp\left(-\frac{(\mathrm{p_4 m} + \mathrm{p_5 r} - \mathrm{p_0})^2}{2\mathrm{p_1^2}} - \frac{(\mathrm{p_6 m} + \mathrm{p_7 r} - \mathrm{p_2})^2}{2\mathrm{p_3^2}}\right) \mathrm{dm\,dr}} \tag{5.28}$$

The normalization given by Equation 5.12 is ensured by numerically calculating the integral over the allowed physical region. Table 5.10 lists all fit parameters.
The uncertainties in the modeling of f_b is a source of systematics.

5.8.2 Ensemble Tests and Calibration

As for the previous approaches, ensemble tests are performed to obtain the calibration. Each dilepton channel is calibrated separately. The combination of all three dilepton channels is done by maximizing the product of the likelihoods of the three channels as described by Equation 5.19. A combined ensemble consists of an $e\mu$, ee, and $\mu\mu$ ensem-

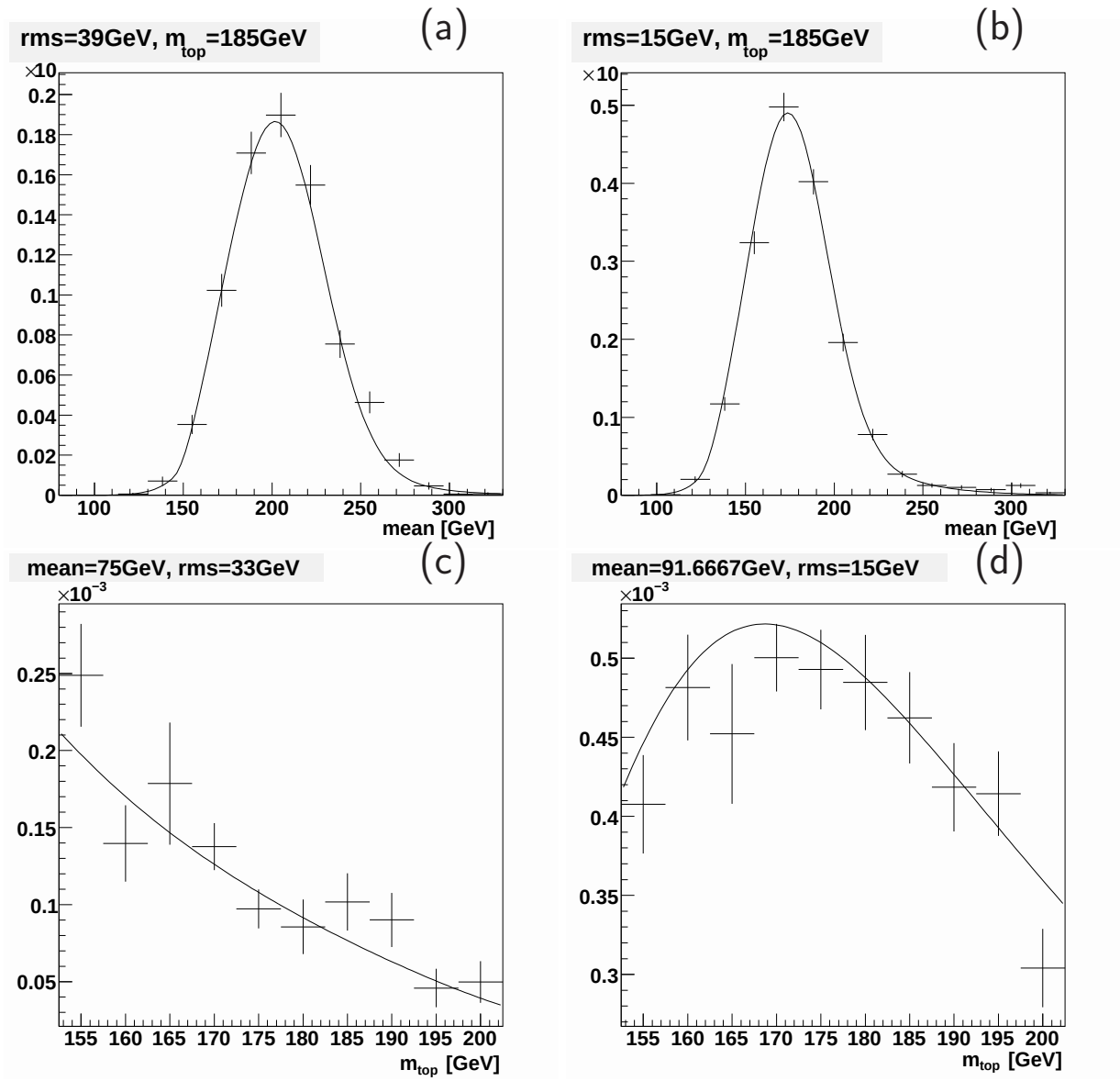

Figure 5.19: One-dimensional slices of the three-dimensional probability density function: $f_s(\text{mean})|_{\text{rms=39 GeV,m}_{\text{top}}\text{=185 GeV}}$ (a), $f_s(\text{mean})|_{\text{rms=15 GeV,m}_{\text{top}}\text{=185 GeV}}$ (b), $f_s(m_{\text{top}})|_{\text{mean=75 GeV,rms=33 GeV}}$ (c), $f_s(m_{\text{top}})|_{\text{mean=91.7 GeV,rms=15 GeV}}$ (d).

ble yielding a combined top quark mass measurement. 300 ensembles are formed for each dilepton channel and the combination. The $-\log\mathcal{L}$ functions are minimized in one step by MINUIT as described in Section 5.5. The Z production background is modeled by ALPGEN including the MLM-matching. Signal events and diboson production are simulated by PYTHIA as in the previous analyzes.
The calibration curves for each dilepton channel are given in Figure 5.23 on the left-hand side. Slopes and offsets of the fitted linear curves are summarized in Table 5.11. The

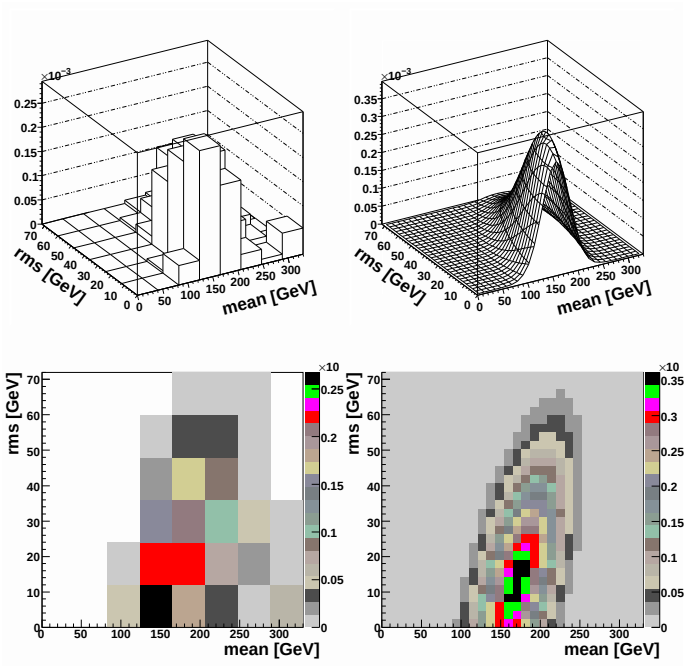

Figure 5.20: Background probability density function $f_b(\text{mean}, \text{rms})$ for the $e\mu$ channel. The histogram is shown on the left and the 2-d fit is shown on the right.

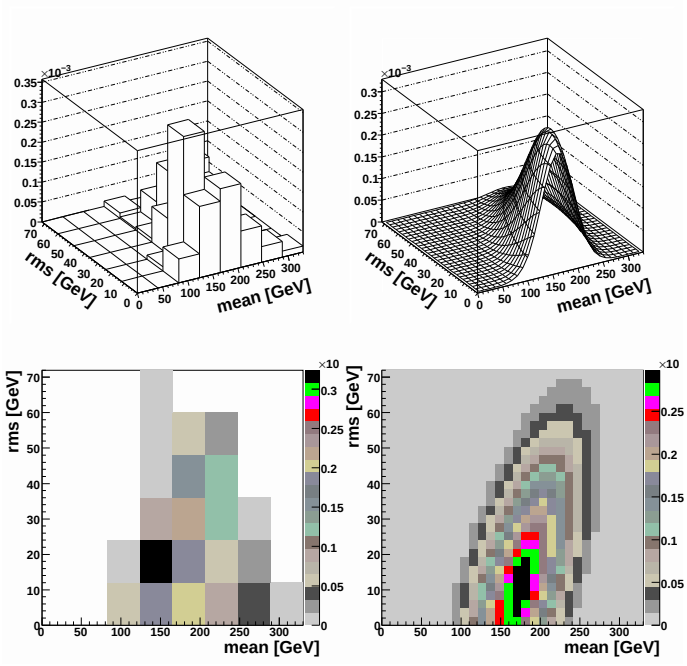

Figure 5.21: Background probability density function $f_b(\text{mean}, \text{rms})$ for the ee channel. The histogram is shown on the left and the 2-d fit is shown on the right.

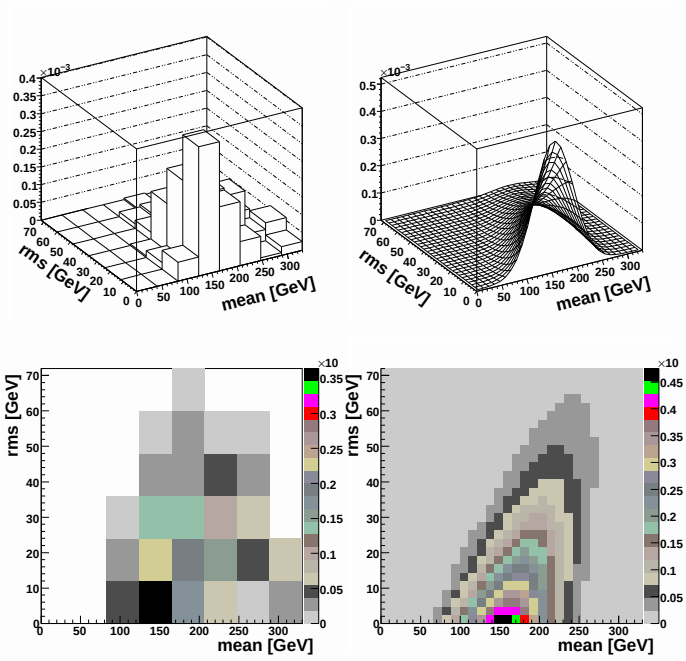

Figure 5.22: Background probability density function $f_b(\text{mean}, \text{rms})$ for the $\mu\mu$ channel. The histogram is shown on the left and the 2-d fit is shown on the right.

	$e\mu$			ee			$\mu\mu$		
p_0	174.4	$\pm$	15.9	174.7	$\pm$	28.2	273.6	$\pm$	34.2
p_1	30.9	$\pm$	3.0	35.5	$\pm$	6.2	26.6	$\pm$	2.3
p_2	5	$\pm$	13	7	$\pm$	25	281.1	$\pm$	93.6
p_3	18.5	$\pm$	7.2	20.2	$\pm$	14.9	61.7	$\pm$	5.5
p_4	1.1	$\pm$	0.1	1.1	$\pm$	0.2	0.55	$\pm$	0.08
p_5	-0.8	$\pm$	0.2	-0.93	$\pm$	0.49	-1.1	$\pm$	0.2
p_6	-0.10	$\pm$	0.08	0.10	$\pm$	0.15	-1.2	$\pm$	0.1
p_7	-0.9	$\pm$	0.3	-1.0	$\pm$	0.6	2.2	$\pm$	0.4

Table 5.10: Fitted parameters for the three dilepton channels for the background probability functions f_b.

slopes are consistent with unity and the offsets are small. The offsets of the dielectron and dimuon channel are of the order 1 GeV and reflect the effects of the modeling of f_s. But since f_s is smooth, the offset can be corrected for and there is no systematic uncertainty on the top quark mass arising from the modeling of f_s. In principal, any smooth probability density function with a dependency on m_{top} and without local minima could be used to measure the top quark mass, as long as the top quark mass estimate is calibrated accordingly. However, corrections larger than the statistical uncertainty are undesired and a bad modeling of f_s leads to a loss in sensitivity, i.e. a larger statistical

Channel	slope	offset [GeV]	⟨pull width⟩	$\langle\sigma_{m_{\mathrm{top}}}\rangle$ [GeV]
$e\mu$ **channel**	0.99 ± 0.02	-0.08 ± 0.18	1.05 ± 0.02	8.4
ee **channel**	0.96 ± 0.02	-1.19 ± 0.24	1.02 ± 0.02	10.7
$\mu\mu$ **channel**	1.08 ± 0.04	1.23 ± 0.50	1.15 ± 0.02	16.0
Combined channel	1.02 ± 0.01	0.12 ± 0.13	1.02 ± 0.02	6.0

Table 5.11: Slope and offset of the calibration curves in Figure 5.23, the pull width after calibration, and the mean value of the statistical uncertainty after calibration and correction for the pull width for the three channels and the combination.

uncertainty of m_{top}.
The right-hand side of Figure 5.23 shows the pull width as a function of the top quark mass for the three dilepton channels. Figure 5.24 shows the calibration curve and the pull width versus m_{top} for the combined channel. The average pull widths are consistent with unity, i.e. the fitted probability density functions lead to a good estimate of the statistical uncertainties. The pull width is slightly too high only for the dimuon channel that has the lowest statistics. All channels and the combination are calibrated to account for the calibration curves and the non-unit pull widths.

5.8.3 Results

The top quark mass is measured with 57 candidate events selected in a data set of 1.05 fb^{-1}. The fully calibrated results for the individual dilepton channels and the combination are:

$$\boldsymbol{e\mu}: \quad m_{\mathrm{top}} = 170.6 \pm 8.6\ (\mathrm{stat.})\ \mathrm{GeV} \tag{5.29}$$

$$\boldsymbol{ee}: \quad m_{\mathrm{top}} = 173.9 \pm 9.3\ (\mathrm{stat.})\ \mathrm{GeV} \tag{5.30}$$

$$\boldsymbol{\mu\mu}: \quad m_{\mathrm{top}} = 179.7 \pm 15.5\ (\mathrm{stat.})\ \mathrm{GeV} \tag{5.31}$$

$$\textbf{combined}: \quad m_{\mathrm{top}} = 172.5 \pm 5.8\ (\mathrm{stat.})\ \mathrm{GeV} \tag{5.32}$$

The results agree within the statistical uncertainties. Figure 5.25 compares the observed statistical uncertainties with the expected ones. The mean of the distribution of uncertainties of the 300 ensembles is a measure for the expected uncertainties $< \sigma_{m_{\mathrm{top}}} >$. The observed uncertainties in the experimental data are marked by an arrow. Table 5.11 includes the $< \sigma_{m_{\mathrm{top}}} >$ of all channels. A one-dimensional slice of the combined seven-dimensional negative logarithmic likelihood distribution as a function of the top quark mass is shown in Figure 5.26. The curve has the shape of a parabola as expected. The minimum indicates the uncalibrated top quark mass estimate. In the next section the systematic uncertainties of all measurements are discussed.

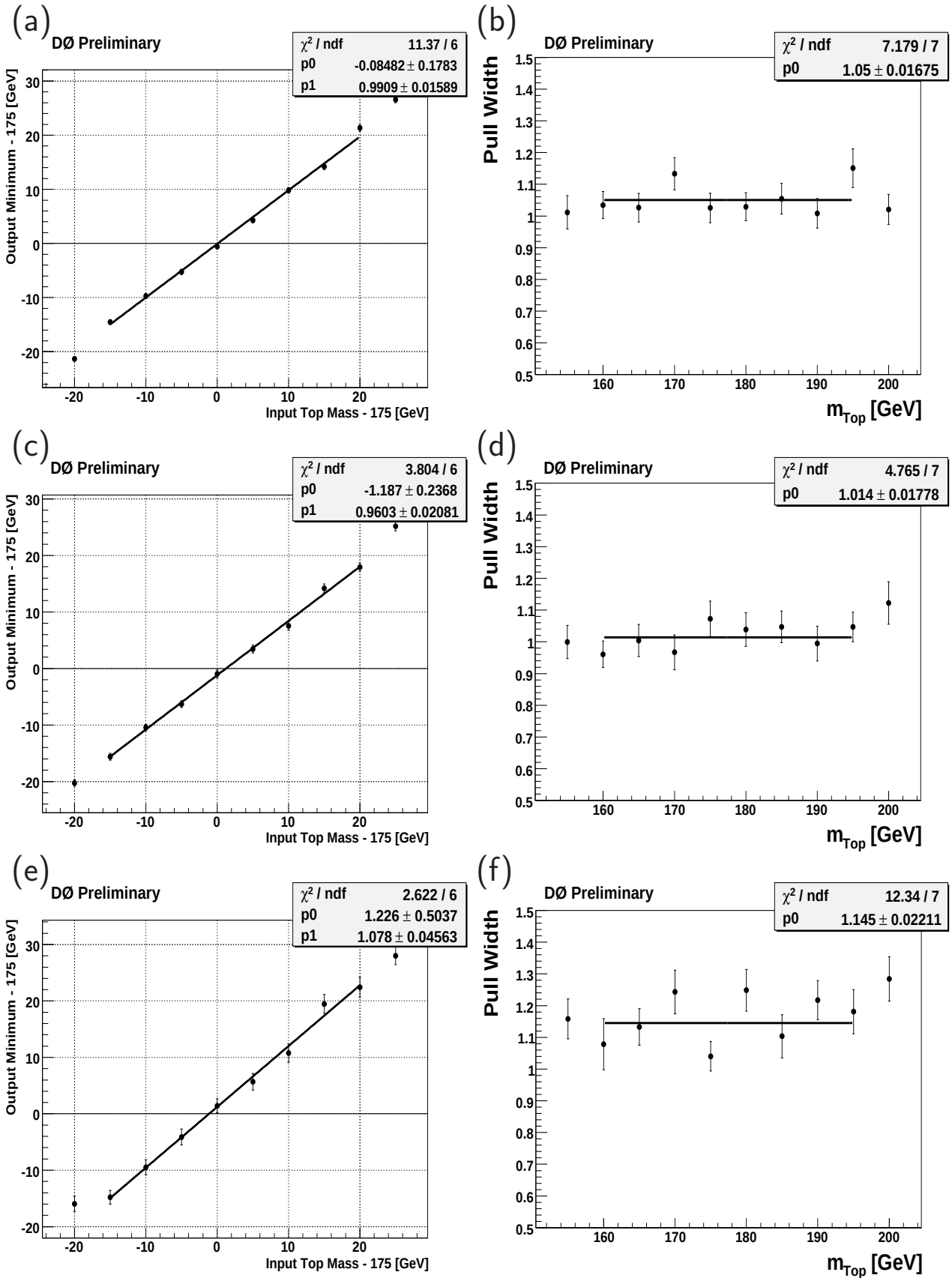

Figure 5.23: Calibration curves: Top quark mass estimate as function of generated input top quark mass for the $e\mu$ (a), ee (c), a nd $\mu\mu$ (e) channels. Pull width distributions for the $e\mu$ (b), ee (d), and $\mu\mu$ (f) channels.

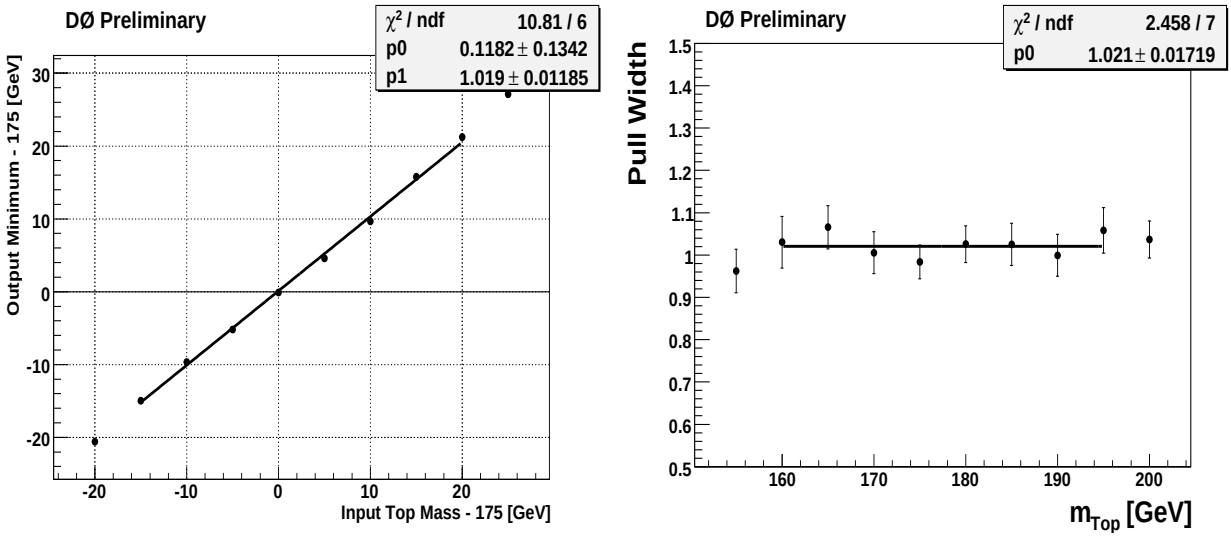

Figure 5.24: Calibration curve: Top quark mass estimate as function of generated input top quark mass for the combination of all three dilepton channels (left). Pull width distributions for the combination (right).

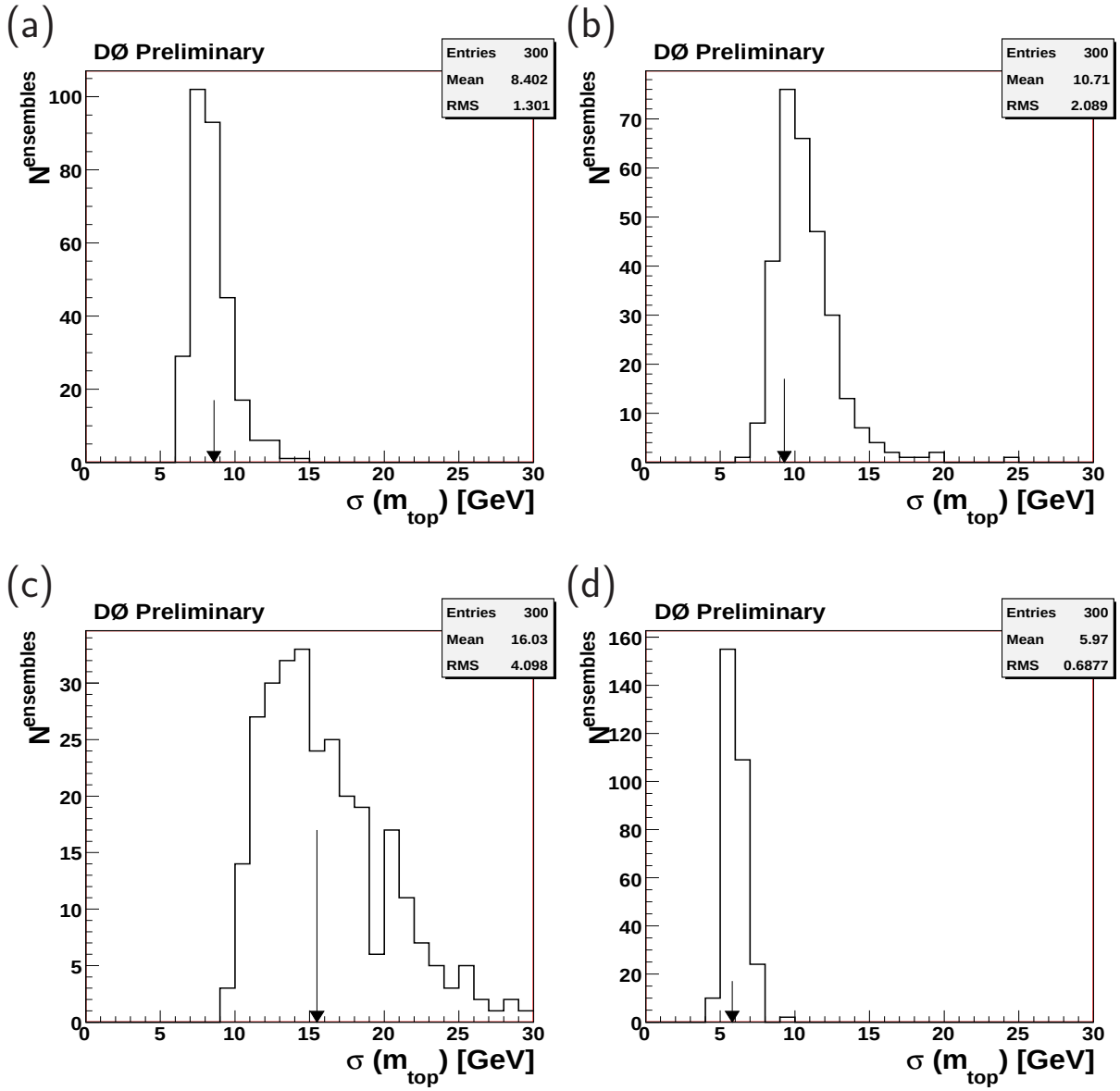

Figure 5.25: Distribution of statistical uncertainties after correcting for the pull width for $m_{\mathrm{top}}^{\mathrm{MC}}$=170 GeV. Results are shown for the $e\mu$ (a), the ee (b), the $\mu\mu$ (c), and the combined (d) channels. The arrows mark the observed uncertainties in data.

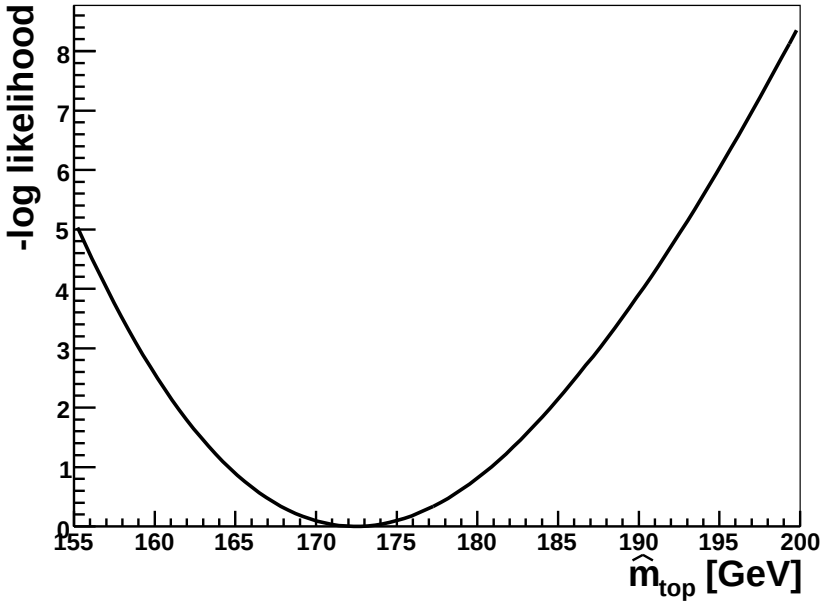

Figure 5.26: Negative logarithmic likelihood curve of the data measurement for the combination of all three dilepton channel as a function of m_{top}.

5.9 Systematic Uncertainties

The following paragraphs discuss the sources of systematic uncertainties. The individual uncertainties are assumed to be uncorrelated and are added in quadrature to obtain the total systematic uncertainty. The systematics that apply to each of the three dilepton channels are found to be the same. Since the systematics on the jet energy scale dominates the total systematic uncertainty, a few systematic uncertainties are conservatively estimated by taking the results from the preliminary measurement for the winter conferences 2006 [79].

Jet Energy Scale Uncertainty. As expected, the main systematic uncertainty arises from the uncertainty in the jet energy scale. The momenta of the b-jets are highly correlated with the top quark mass. For this reason, systematically miscalibrated jets can produce substantial shifts in the observed top quark mass. They are estimated by repeating the ensemble testing with simulated events, where the jet energy scale has been raised and lowered by one sigma. The total uncertainty on the jet energy scale is calculated from the statistical and systematic uncertainty on the jet energy scale in data and in simulated events:

$$\sigma^{\mathrm{jes}}_{\mathrm{total}} = \sigma^{\mathrm{sim\,jes}}_{\mathrm{stat}} \oplus \sigma^{\mathrm{sim\,jes}}_{\mathrm{syst}} \oplus \sigma^{\mathrm{data\,jes}}_{\mathrm{stat}} \oplus \sigma^{\mathrm{data\,jes}}_{\mathrm{syst}} \tag{5.33}$$

The jet energy scale of the events used to estimate the probability density functions remain unshifted. Figure 5.27 (a)-(c) show the calibration curves before and after the shift of the jet energy scale for the Binned Method, the Moments Method, and the 3d-Fit Method. The uncertainties on the top quark mass measurements are found to be $\pm$ 3 to 5 GeV. It is known that an uncertainty of ± 5 $rmGeV$ overestimates the effect of the jet energy scale and recent studies indicate that a better understanding of this uncertainty will reduce it by about a factor of two.

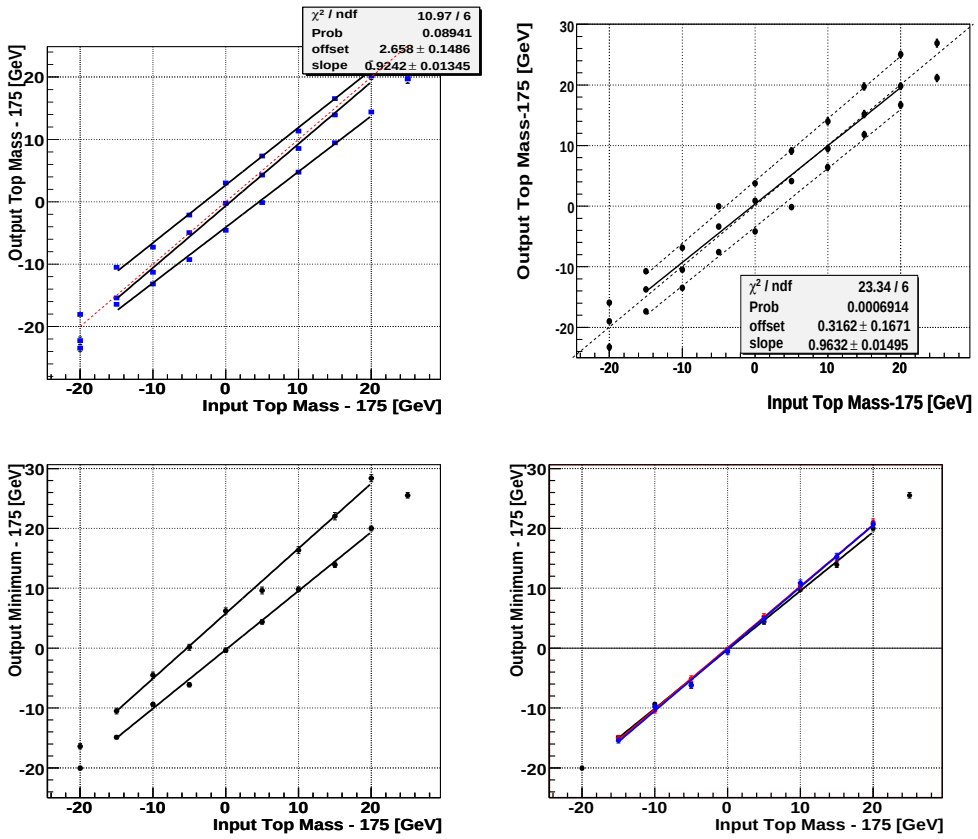

Figure 5.27: Calibration curve after shifting the JES up and down by one sigma and nominal calibration for the Binned Method, Maximum Method, and 3d-Fit Method. Calibration curve after variation of jet energy resolution (bottom right).

***b*-Jet Energy Scale.** The jet energy scale has been derived for inclusive jet flavors. Applying it to b-jets only leads to an additional 1.5% uncertainty in the jet energies. This yields an uncertainty of $\pm$2.0 GeV for the top quark mass.

Jet Resolution Uncertainty. The jet resolution of simulated events is described in Section 4.4.1. A shifting, smearing and removal of simulated jets is performed. To estimate the systematics of this procedure, the resolution of simulated signal events is

shifted up and down by its uncertainty. The ensemble testing is repeated with the shifted events, but with the nominal probability density functions. The obtained calibration curves are shown in Figure 5.27 (d). It can be seen that the effect is of the same order as the statistical uncertainties of the calibration. The jet resolution uncertainty is found to be ± 0.3 GeV for the three 3d-Fit Method. The other results take the estimate of ± 0.4 GeV from [79].

Uncertainty in Radiation of extra Jets. The presence of extra jets in top quark events for example arising from gluon radiation is a source of systematics. The jet multiplicity of the selected events is modeled by the simulation within the statistical uncertainties. However, the ratio of events with exactly two jets and events with more than two jets is 0.26 for simulated events and 0.14 in data. To account for this difference, the simulated events are reweighted such that this ratio is the same. Ensemble test are performed with the reweighted events and a difference in the top quark mass of 0.14 GeV is observed.
This uncertainty was found to be 2 GeV in the earlier version of the analysis [79]. It was estimated not by reweighting the events, but by using a statistically independent sample to simulate a different composition of jet multiplicities. This introduced a large statistical uncertainty for the estimate of the systematics.

Color Recombination. There is a systematic effect due to the modeling of the underlying event and color recombination. The simulated PYTHIA events used in this analysis use the so-called TUNE A. TUNE A is a set of parameters for the PYTHIA generator associated with initial and final state radiation, underlying event, and hadronization that was tuned to reproduce distributions from the low-bias data acquired by the CDF collaboration. TUNE DW is an update to this set of parameters incorporating high p_T jet data from the DØ collaboration (azimuthal decorrelations in dijet events) and the Z p_T spectrum measured by CDF. TUNE DW has significantly less initial state radiation than TUNE A and corresponding increases in the other parameters to maintain agreement with the low-bias CDF data. To estimate the effect of the choice of the tune, ensemble tests are performed using PYTHIA events with TUNE DW. A calibration curve in the range between 160 GeV and 185 GeV is obtained and the difference in the measured top quark mass is found to be 0.13 GeV.

Muon Resolution. The effect of the muon resolution on the top quark measurements is studied by smearing the muon momenta by $\pm 1\sigma$ of their resolution. Ensemble tests with signal events with $m_{\top} = 175$ GeV yield an uncertainty of ± 0.4 GeV [79].

Statistics of Background Simulation and Background Shape. The modeling of the background probability density functions is limited by the available amount of simulated background events, both for the PDE method and the fitting technique. However, the top quark mass measurement is not very sensitive to the background modeling, because the expected signal fraction in the selected data samples is high. The effect is

studied in two ways. The available background samples are split in independent sub-samples and the deviation of the results obtained from each sub-sample of ± 0.9 GeV is taken as estimate of the uncertainty. In addition a larger sample of background events is generated using the fast simulation PMCS. Comparisons with the background shape of events modeled with GEANT yield an uncertainty of ± 0.3 GeV [79]. As the size of background samples has been increased, this is a conservative estimate of the uncertainty for the subsequent analyzes.

Proton Density Functions. Uncertainties in the proton density functions propagate to an uncertainty of the top quark mass. The variations of the PDF lead an uncertainty of ± 0.7 GeV [79].

Background Yields. The uncertainty on the yield for background leads to an systematic uncertainty on m_{top}. This is particularly of concern for the analyses of the 835 pb^{-1} data sets in the $e\mu$ channel given that the cross-section analysis observes discrepancies in the number of events with zero jets and one jet. To conservatively estimate this uncertainty, ensemble tests assuming nominal background yields and then double the dominant background yield ($Z \to \tau\tau$) are performed. The difference in expectations was taken as the systematic uncertainty and found to be ± 1.0 GeV. The discrepancies were studied and the trigger turn-on curves were remeasured resulting in the improved $e\mu$ selection applied to the 1.05 fb^{-1} data set [59]. This is why there is no uncertainty for the background yield assigned to the measurements with the 3d-Fit Method.

Table 5.12 summarizes all systematic uncertainties of the Binned, Moments, and Maximum Method. With a total uncertainty of about 5 GeV, the top quark mass measurement in the dilepton channel is still limited by the statistical uncertainty. The systematic uncertainties of the measurement with 1 fb^{-1} with the 3d-Fit Method in all three dilepton channels are summarized in Table 5.13. The total uncertainty of 5.5 GeV is of the order of the statistical uncertainty of 5.8 GeV. Future versions of the analysis will benefit from the efforts to reduce the uncertainty of the jet energy scale. While finishing this thesis an improved release of the jet energy scale passed the first stage of approval [80].

5.10 Top Quark Mass World Average

The determination of the top quark mass with a dataset of 1046 pb^{-1} is at present the most precise measurement of the DØ experiment in the dilepton final states. The result $m_{\text{top}} = 172.5 \pm 5.8$ (stat.) $\pm$ 5.5 (syst.) GeV is consistent with top quark mass measurements using other methods, decay channels, and with results from the CDF experiment. It is combined with other results by the Tevatron Electroweak Working Group yielding the top quark mass world average of March 2007 [12]:

$$m_{\text{top}} = 170.9 \pm 1.1 \text{ (stat.)} \pm 1.5 \text{ (syst.) GeV}. \tag{5.34}$$

Source	Uncertainty (GeV)
Jet Energy Scale (**Moments** and **Binned Method**)	$^{+4.4}_{-3.0}$
Jet Energy Scale (**Maximum Method**)	$^{+3.6}_{-3.9}$
Jet Resolution	± 0.4
Muon Resolution	± 0.4
$t\bar{t}$ + jets	± 2.0
PDF variation	± 0.7
Background Template Shape	± 0.3
Background Yields	± 1.0
Template fit statistics	± 0.9
Total Systematics (**Moments** and **Binned Method**)	$^{+5.1}_{-4.0}$
Total Systematics (**Maximum Method**)	$^{+4.4}_{-4.7}$

Table 5.12: Summary of systematic uncertainties for measurement of m_{top} with the Binned, Moments, and Maximum Method with 835 pb^{-1}. measurement.

Source	Uncertainty (GeV)
Jet Energy Scale	± 5.0
b-Jet Energy Scale	± 2.0
Jet Resolution	± 0.3
Muon Resolution	± 0.4
$t\bar{t}$ + jets	± 0.14
PDF variation	± 0.7
Background Template Shape	± 0.3
Template fit statistics	± 0.9
Underlying event	± 0.13
Total Systematic Uncertainty	± 5.5

Table 5.13: Summary of systematic uncertainties for measurement of m_{top} with the 3d-Fit Method with 1.05 fb^{-1}.

Figure 5.28 contains all measurements entering the world average combination. The BLUE method is applied for the statistical combination of the measurements [81, 82]. A weight is assigned to each measurement depending on the statistical and systematic uncertainty, and the correlations between the uncertainties of all measurements. The weights are summarized in Table 5.14. The pulls are also given, indicating good agreement among all results. The most precise results are obtained in the lepton + jets channel. The total uncertainty of 1.1% is limited by the systematics that mainly arise from the jet energy scale.

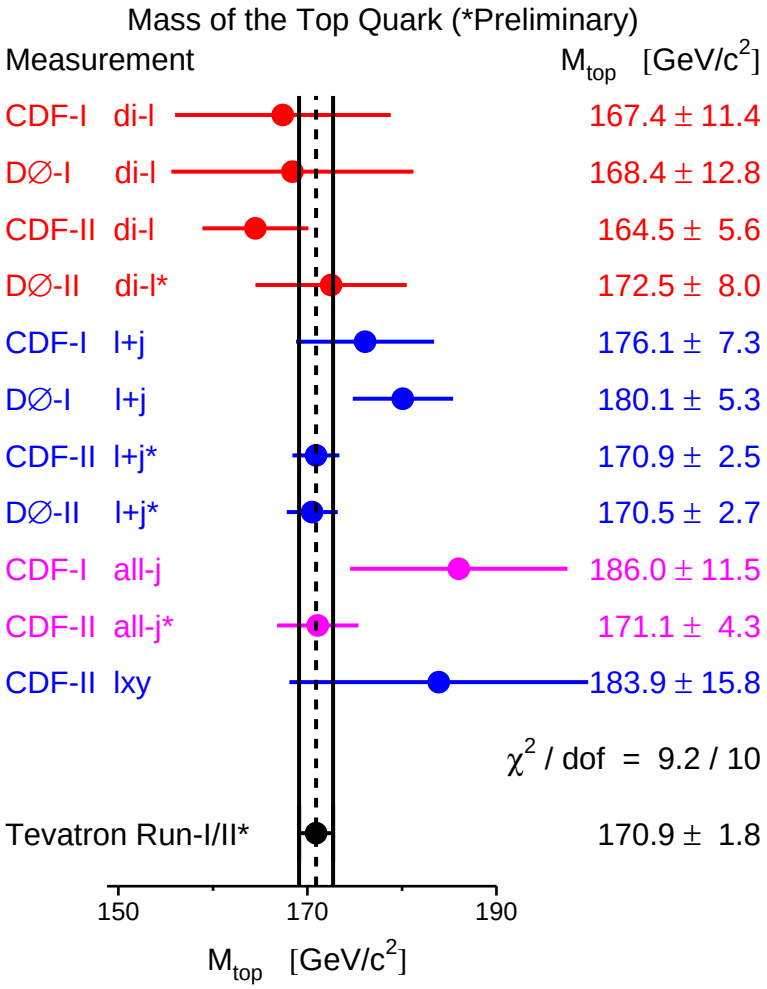

Figure 5.28: A summary of the input measurements and the resulting world average mass of the top quark.

Run I published					Run II preliminary					
CDF			DØ		CDF				DØ	
l+j	di-l	all-j	l+j	di-l	l+j	di-l	all-j	lxy	l+j	di-l
+0.73	−0.31	+1.33	+1.84	−0.20	−0.03	−1.22	+0.05	+0.83	−0.22	+0.20
−1.3	−0.4	−0.3	+6.1	+0.4	+39.3	+6.4	+11.0	+0.5	+39.7	−1.9

Table 5.14: The pull (first row) and weight in % (second row) for each of the inputs used to determine the world average mass of the top quark [12]. See Reference [81] for a discussion of negative weights.

Chapter 6

Conclusion

6.1 Summary of the Results

Several measurements of the top quark mass in the dilepton final states with the DØ experiment were presented. The presence of two high p_T charged leptons, two b-jets, and missing transverse energy are a clear signature of the dilepton channel. However, the small branching ratio and the overwhelming background originating from Z production pose a challenge for the separation of signal events. The top quark mass cannot be extracted directly from the measured physics objects in the event, because the kinematics is underconstraint by one degree of freedom. The Neutrino Weighting makes assumptions on the neutrino rapidities according to the Standard Model expectations to make the kinematics solvable. Signal and background probability density functions are modeled with the help of simulated events to measure the top quark mass by maximizing a likelihood function. Several choices of sensitive variables provided by the Neutrino Weighting were studied and compared, and two smoothing techniques were optimized and enhanced with the aim to increase the sensitivity to m_{top} and to keep the systematic uncertainties low.
In a dataset of 835 pb^{-1} integrated luminosity 28 $e\mu$ candidate events are found. The top quark mass is measured with three different approaches, yielding:

$$\textbf{Binned Method :} \quad m_{\text{top}} = 173.6 \pm 6.7 \text{ (stat.) } ^{+5.1}_{-4.0} \text{ (syst.) GeV} \tag{6.1}$$

$$\textbf{Moments Method :} \quad m_{\text{top}} = 171.6 \pm 7.9 \text{ (stat.) } ^{+5.1}_{-4.0} \text{ (syst.) GeV} \tag{6.2}$$

$$\textbf{Maximum Method :} \quad m_{\text{top}} = 165.7 \pm 9.7 \text{ (stat.) } ^{+4.4}_{-4.7} \text{ (syst.) GeV.} \tag{6.3}$$

The results were presented at the international summer conferences 2006. They were the first public results on the top quark after the reprocessing of the DØ data in 2005 and the introduction of the new analysis framework CAFE.
The studies of all three approaches led to a new approach. The systematic errors originating from a lack of smoothing by the PDE method are avoided by smoothing the probability density functions with a multidimensional fit. The three-dimensional signal probability density function provides high sensitivity to the top quark mass. The development of the three-dimensional fit for all three dilepton channels is a key element of

this new approach.
The improvement of the $e\mu$ selection and the development of selections for the dielectron and dimuon channel allows to measure the top quark mass in all three dilepton channels. A dataset of 1.05 fb^{-1} integrated luminosity with 57 candidate events was analyzed for the international winter conferences 2007. The results for the individual channels and the combination reads:

$$\boldsymbol{e\mu}: \quad m_{\text{top}} = 170.6 \pm 8.6\ (\text{stat.}) \pm 5.5\ (\text{syst.})\ \text{GeV} \tag{6.4}$$
$$\boldsymbol{ee}: \quad m_{\text{top}} = 173.9 \pm 9.3\ (\text{stat.}) \pm 5.5\ (\text{syst.})\ \text{GeV} \tag{6.5}$$
$$\boldsymbol{\mu\mu}: \quad m_{\text{top}} = 179.7 \pm 15.5\ (\text{stat.}) \pm 5.5\ (\text{syst.})\ \text{GeV} \tag{6.6}$$
$$\textbf{combined}: \quad m_{\text{top}} = 172.5 \pm 5.8\ (\text{stat.}) \pm 5.5\ (\text{syst.})\ \text{GeV}. \tag{6.7}$$

The combined result is presently the best measurement of the DØ experiment in the dilepton final states. It entered the combination of the top quark mass world average in March 2007:

$$\textbf{world average}: \quad m_{\text{top}} = 170.9 \pm 1.1\ (\text{stat.}) \pm 1.5\ (\text{syst.})\ \text{GeV}. \tag{6.8}$$

All measurements are consistent with each other, and with top quark measurements with other method, other decay channels, and results from the CDF experiment. There are no hints for an inconsistency of the Standard Model. While the results in the dilepton channel still have a larger statistical than systematic uncertainty, the world average is limited by the systematic uncertainty. A precision of 1.1% for the top quark mass has been reached.

6.2 Outlook

The aim of the Tevatron experiments is to reduce the uncertainty of the top quark mass to about 2 GeV per experiment. A main focus will the reduction of the jet energy scale uncertainty. The precision of top quark mass measurements in the dilepton channel will be increased by analyzing larger datasets. The number of candidates will also be increased by including the so-called lepton plus track channel. These are dilepton events with only one identified lepton and one high p_T isolated track. Properties measurements in the dilepton channel are not only restricted to the top quark mass. The helicity of the W bosons origination from top decays, spin correlations between the top pairs, and many more interesting analyses are possible.
The dilepton channel will be of special interest at experiments at the Large Hadron Collider as it has the cleanest signature among all $t\bar{t}$ decay channels. Since measurements will only be limited by systematic uncertainties this is an important advantage.
There are still open questions about the physics of the top quark that will be answered in the near future by interesting searches and results!

Appendix A

Kinematic Reconstruction of Dilepton Events

$t\bar{t} \rightarrow W^+ b W^- \bar{b} \rightarrow l^+ \nu l^- \bar{\nu}$

- Particles in final state:

b-quark:	p^b	$=$	$(E^b, \vec{p}^{\,b})$	$=$	$(E^b, p_x^b, p_y^b, p_z^b)$,	m^b	$=$	4.3 GeV/c^2
$\bar{b}$-quark:	$p^{\bar{b}}$	$=$	$(E^{\bar{b}}, \vec{p}^{\,\bar{b}})$	$=$	$(E^{\bar{b}}, p_x^{\bar{b}}, p_y^{\bar{b}}, p_z^{\bar{b}})$,	$m^{\bar{b}}$	$=$	4.3 GeV/c^2
lepton:	p^{l^-}	$=$	$(E^{l^-}, \vec{p}^{\,l^-})$	$=$	$(E^{l^-}, p_x^{l^-}, p_y^{l^-}, p_z^{l^-})$,	m^{l^-}	$\approx$	0 GeV/c^2
antilepton:	p^{l^+}	$=$	$(E^{l^+}, \vec{p}^{\,l^+})$	$=$	$(E^{l^+}, p_x^{l^+}, p_y^{l^+}, p_z^{l^+})$,	m^{l^+}	$\approx$	0 GeV/c^2
neurino:	p^{ν}	$=$	$(E^{\nu}, \vec{p}^{\,\nu})$	$=$	$(E^{\nu}, p_x^{\nu}, p_y^{\nu}, p_z^{\nu})$,	m^{ν}	$\approx$	0 GeV/c^2
antineurino:	$p^{\bar{\nu}}$	$=$	$(E^{\bar{\nu}}, \vec{p}^{\,\bar{\nu}})$	$=$	$(E^{\bar{\nu}}, p_x^{\bar{\nu}}, p_y^{\bar{\nu}}, p_z^{\bar{\nu}})$,	$m^{\bar{\nu}}$	$\approx$	0 GeV/c^2

- Kinematic constraints:

$$m^{W\,2} = (p^l + p^\nu)^2 \tag{A.1}$$

$$m^{t\,2} = (p^l + p^\nu + p^b)^2 \tag{A.2}$$

- Measured: $p^b, p^{\bar{b}}, p^{l^+}, p^{l^-}$

- Assume: $m^t, m^W = 80.4\ GeV, \eta^\nu, \eta^{\bar{\nu}}$

Use measurements, assumptions, and equations A.1 and A.2 to completely reconstruct the $t\bar{t}$ event, i.e. to calculate p^ν and $p^{\bar{\nu}}$:

From equation A.1 it follows:

$$m^{W\,2} = (E^l + E^\nu)^2 - (\vec{p}^{\,l} + \vec{p}^{\,\nu})^2 = E^{l\,2} + E^{\nu 2} + 2E^l E^\nu - \vec{p}^{\,l^2} - \vec{p}^{\,\nu^2} - 2\vec{p}^{\,l}\vec{p}^{\,\nu}$$

$$= 2(E^l E^\nu - \vec{p}^{\,l}\vec{p}^{\,\nu})$$

$$\Leftrightarrow E^\nu = |\vec{p}^{\,\nu}| = \frac{1}{E^l}(\frac{m^{W\,2}}{2} + \vec{p}^{\,l}\vec{p}^{\,\nu}) \tag{A.3}$$

From equation A.2 it follows:

$$m^{t\,2} = (E^l + E^\nu + E^b)^2 - (\vec{p}^{\,l} + \vec{p}^{\,\nu} + \vec{p}^{\,b})^2$$

$$= m^{W\,2} + m^{b\,2} + 2(E^l E^b + E^\nu E^b - \vec{p}^{\,l}\vec{p}^{\,b} - \vec{p}^{\,\nu}\vec{p}^{\,b})$$

$$\Leftrightarrow E^\nu = |\vec{p}^{\,\nu}| = \frac{m^{t\,2} - m^{W\,2} - m^{b\,2} - 2p^l p^b}{2E^b} + \frac{\vec{p}^{\,\nu}\vec{p}^{\,b}}{E^b} \tag{A.4}$$

The Lorentz transformation L boosts in z-direction into the system with $p_z^\nu = 0$ GeV:

$$L = \begin{pmatrix} \cosh\eta^\nu & 0 & 0 & -\sinh\eta^\nu \\ 0 & 1 & 0 & 0 \\ 0 & 0 & 1 & 0 \\ -\sinh\eta^\nu & 0 & 0 & \cosh\eta^\nu \end{pmatrix} \tag{A.5}$$

Applying L to equation A.3 yields:

$$p_T^\nu = \frac{m^{W\,2}}{2E^{l'}} + \frac{p_x^l p_x^\nu}{E^{l'}} + \frac{p_y^l p_y^\nu}{E^{l'}}, \tag{A.6}$$

where

$$E^{l'} = E^l \cosh\eta^\nu - p_z^l \sinh\eta^\nu \tag{A.7}$$

Applying L to equation A.4 yields:

$$p_T^\nu = \frac{m^{t\,2} - m^{W\,2} - m^{b\,2} - 2p^l p^b}{2E^{b'}} + \frac{p_x^\nu p_x^b + p_y^\nu p_y^b}{E^{b'}}, \tag{A.8}$$

where

$$E^{b'} = E^b \cosh\eta^\nu - p_z^b \sinh\eta^\nu \tag{A.9}$$

Equation A.6 equals equation A.8. After solving for p_x^ν one obtains a linear equation:

$$p_x^\nu = a p_y^\nu + b, \tag{A.10}$$

where

$$a \equiv \frac{p_y^l E^{b'} - p_y^b E^{l'}}{p_x^b E^{l'} - p_x^l E^{b'}} \tag{A.11}$$

$$b \equiv \frac{E^{l'}(m^{t\,2} - m^{W\,2} - m^{b\,2} - 2p^l p^b) - E^{b'} m^{W\,2}}{2(p_x^l E^{b'} - p_x^b E^{l'})} \tag{A.12}$$

Eliminating p_x^ν in equation A.6 using $p_T^\nu = \sqrt{p_x^{\nu 2} + p_y^{\nu 2}}$ and equation A.10 gives:

$$\sqrt{(a^2+1)p_y^\nu + 2abp_y^\nu + b^2} = \frac{m^{W\,2}}{2E^{l'}} + \frac{p_x^l}{E^{l'}}(ap_y^\nu + b) + \frac{p_y^l}{E^{l'}}p_y^\nu \tag{A.13}$$

Squaring equation A.13 leads to a quadratic equation in p_y^ν of the form

$$cp_y^{\nu 2} + dp_y^\nu + f = 0, \tag{A.14}$$

with

$$c \equiv a^2 + 1 - \left(\frac{p_x^l}{E^{l'}}a + \frac{p_y^l}{E^{l'}}\right)^2 \tag{A.15}$$

$$d \equiv 2ab - 2\left(\frac{m^{W\,2}}{2E^{l'}} + \frac{p_x^l}{E^{l'}}b\right)\left(\frac{p_x^l}{E^{l'}}a + \frac{p_y^l}{E^{l'}}\right) \tag{A.16}$$

$$f \equiv b^2 - \left(\frac{m^{W\,2}}{2E^{l'}} + \frac{p_x^l}{E^{l'}}b\right)^2 \tag{A.17}$$

Equation A.14 has zero, one or two real solutions:

$$p_{y\,1/2}^\nu = -\frac{d}{2c} \pm \frac{1}{2c}\sqrt{d^2 - 4cf} \tag{A.18}$$

p_x^ν can be obtained by plugging in the solution of p_y^ν in equation A.10.
p_z^ν can be calculated with:

$$p_z^\nu = p_T^\nu \sinh \eta^\nu \tag{A.19}$$

- There are up to two solutions for each neutrino, since equation A.14 has to be solved for the neutrino and antineutrino. This leads to a fourfold ambiguity of the reconstructed event kinematics.
- Another twofold ambiguity originates from the two possibilities of assigning the b jets to the charged leptons.
- Alltogether, there are between zero and eight solutions for the neutrino momenta.

Appendix B

Control Plots

Control plots for the $t\bar{t} \rightarrow e\mu + \text{jets}$ channel with a data set of 835 pb^{-1}.

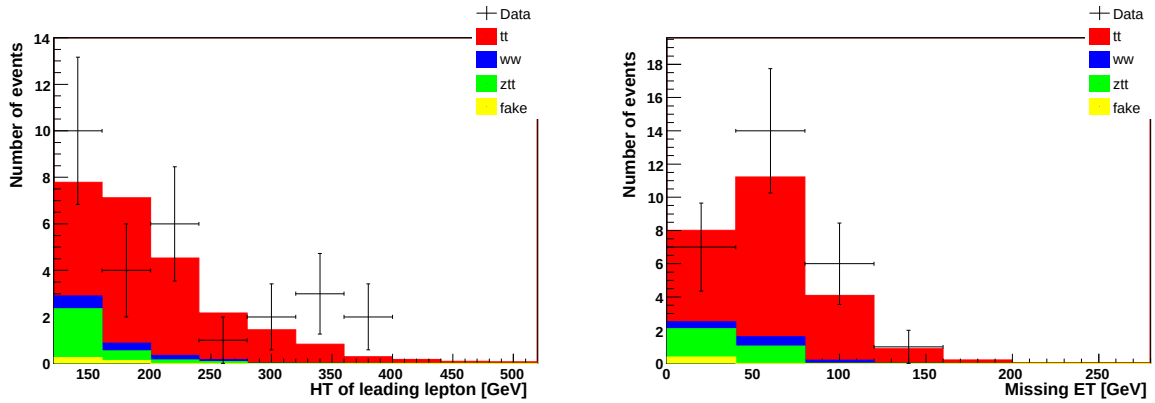

Figure B.1: H_T^l and $\not{E}_T$ distributions.

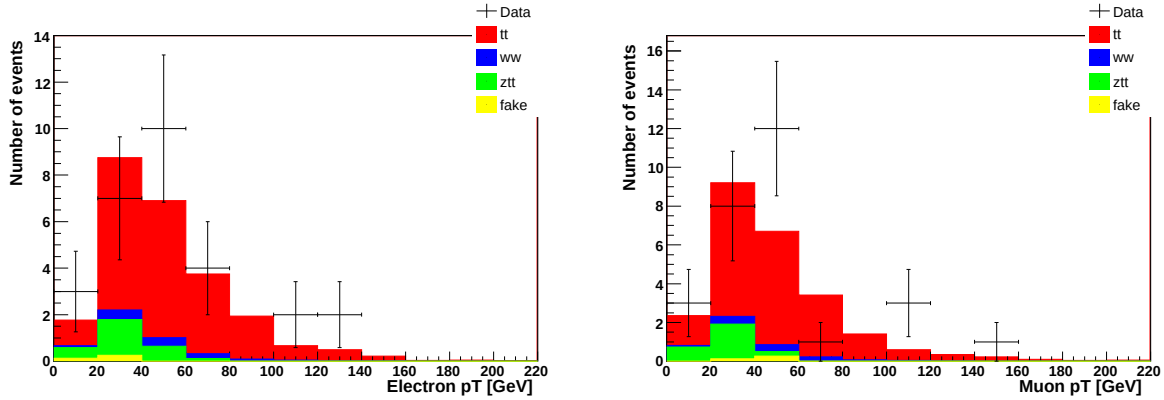

Figure B.2: Electron p_T and muon p_T distributions.

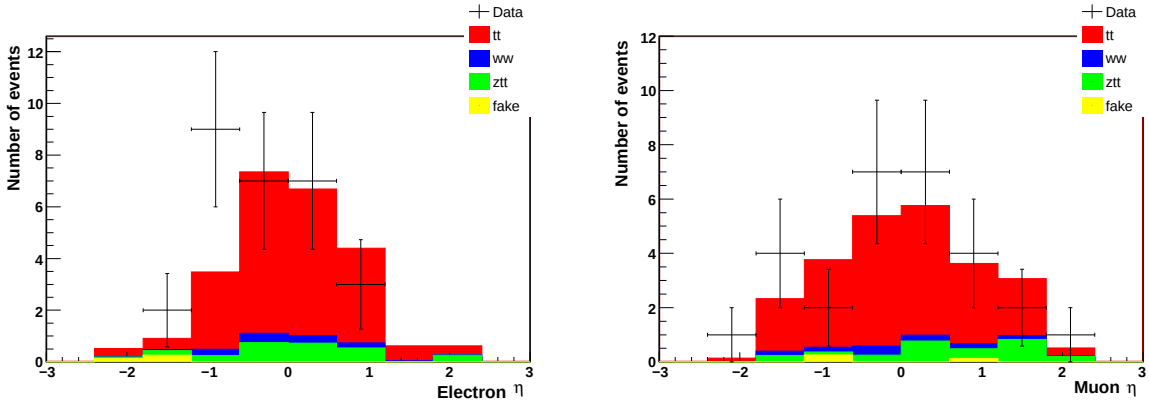

Figure B.3: Electron η and muon η distributions.

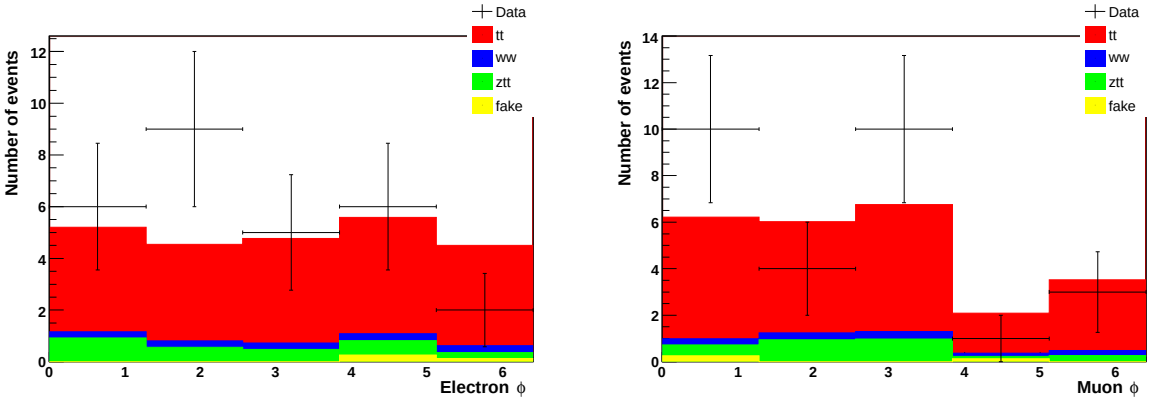

Figure B.4: Electron φ and muon φ distributions.

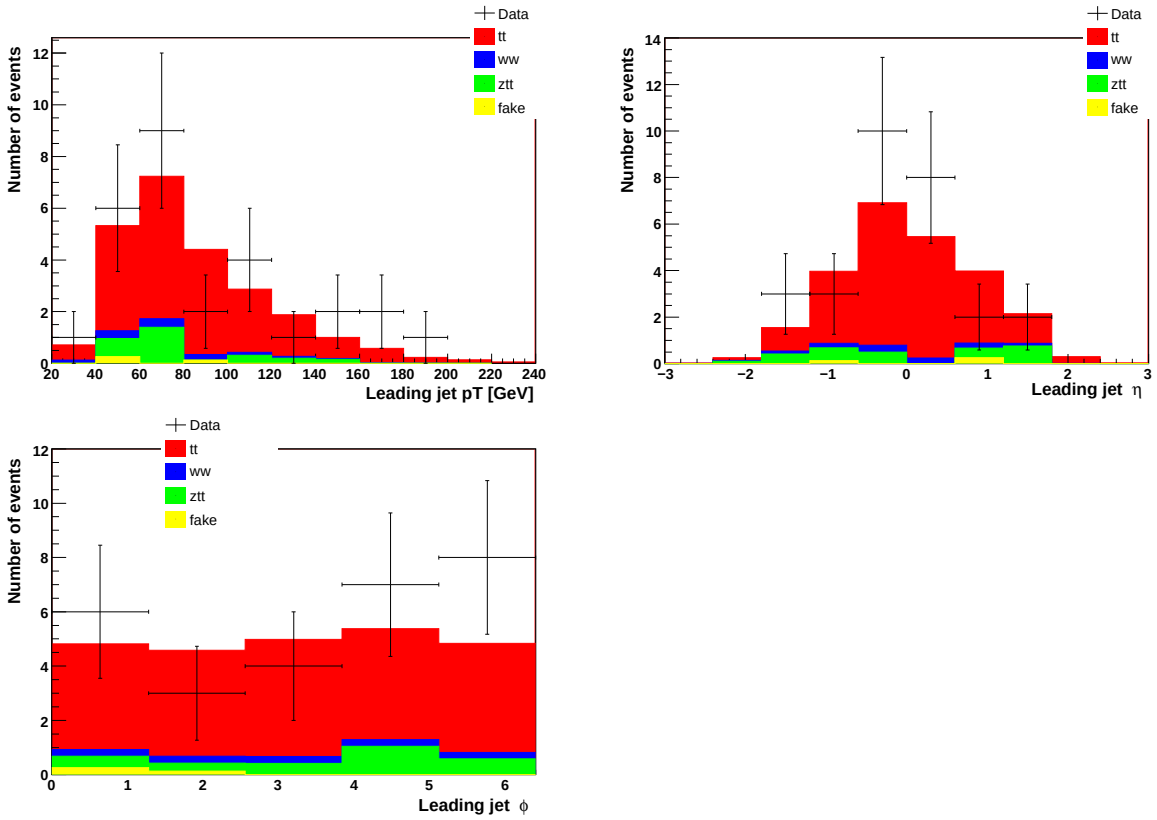

Figure B.5: Leading Jet p_T, η and ϕ distributions.

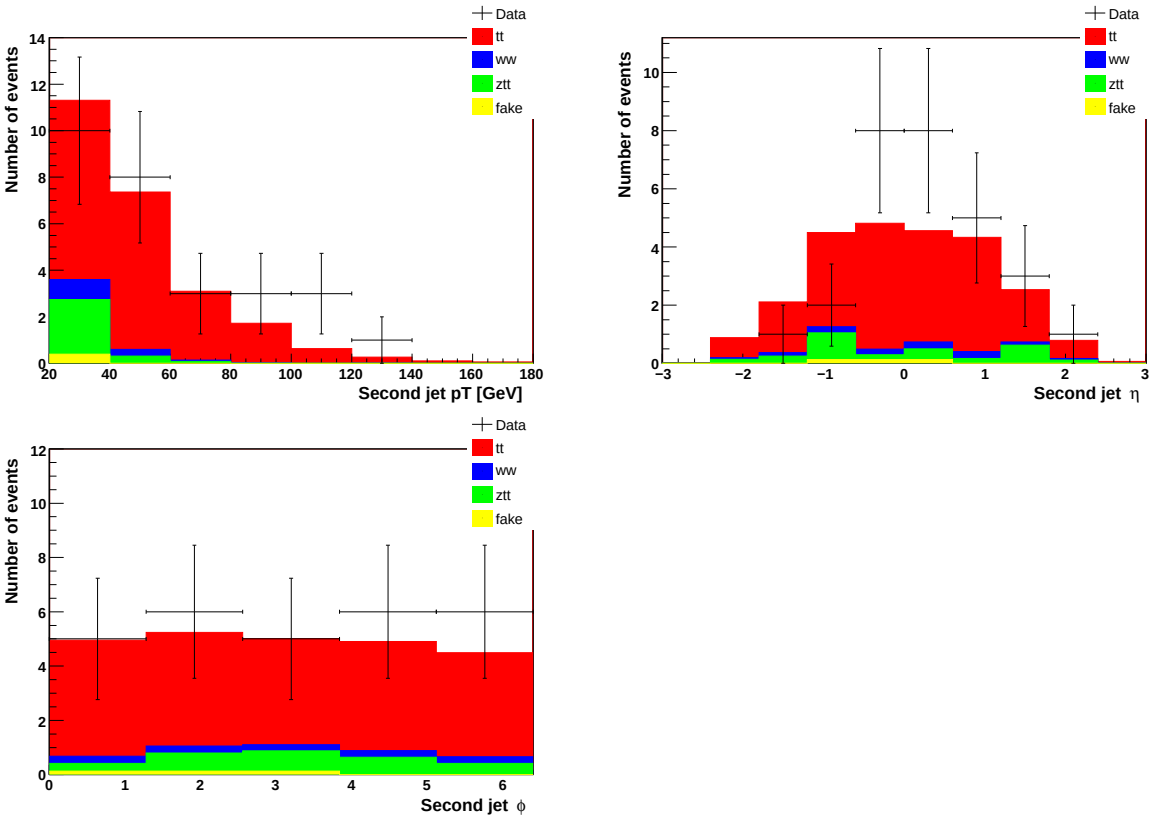

Figure B.6: Second Jet p_T, η and ϕ distributions.

Appendix C

Signal Probability Density Function for the Electron-Muon Channel

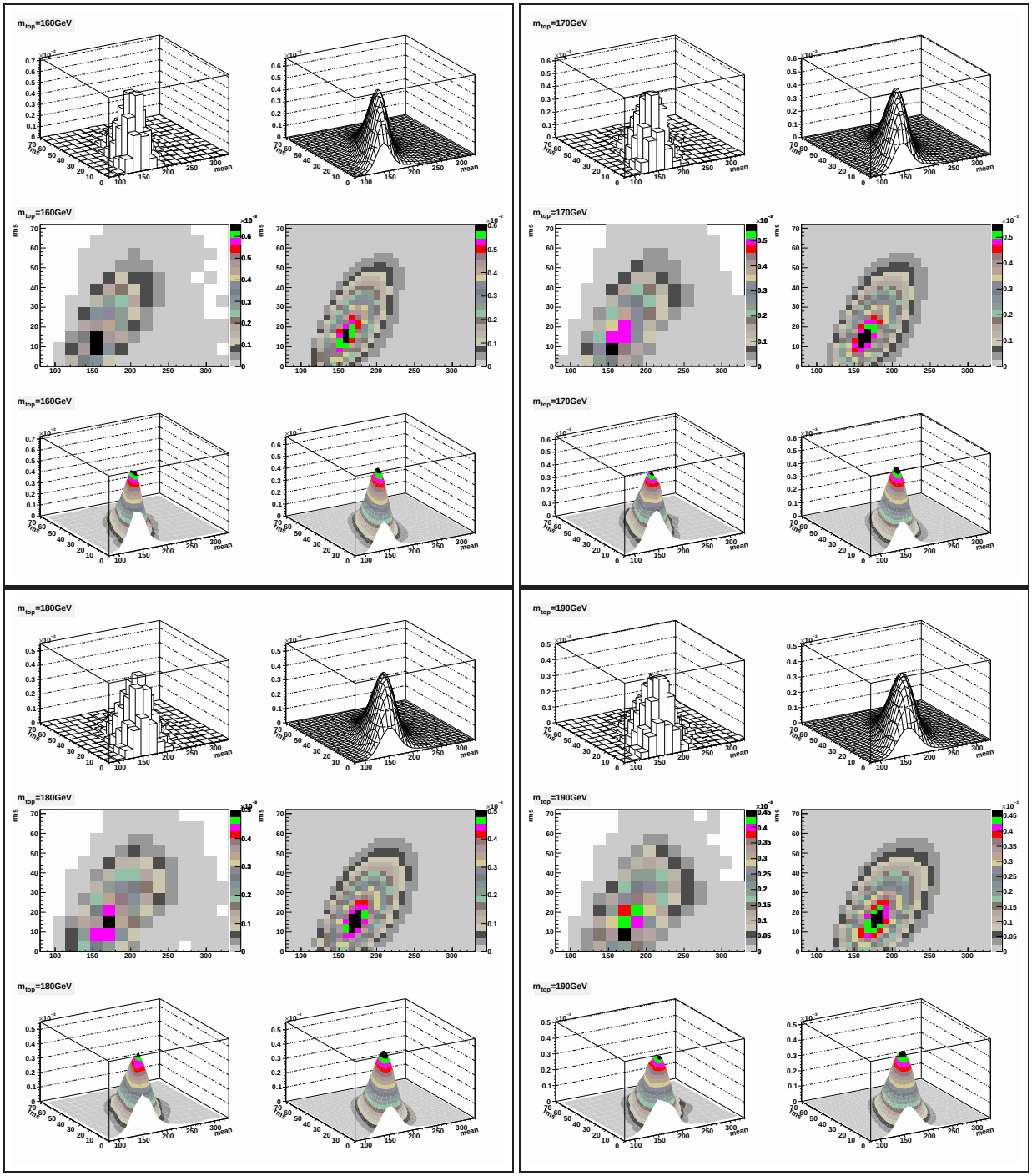

Figure C.1: $e\mu$: The first and third column show the histogram mean vs. rms at a constant m_{top}. The second and fourth column show the corresponding view of the 3d-fit result. m_{top} = 160 GeV, 170 GeV, 180 GeV, and 190 GeV for the upper left, upper right, lower left, and lower right quarter, respectively.

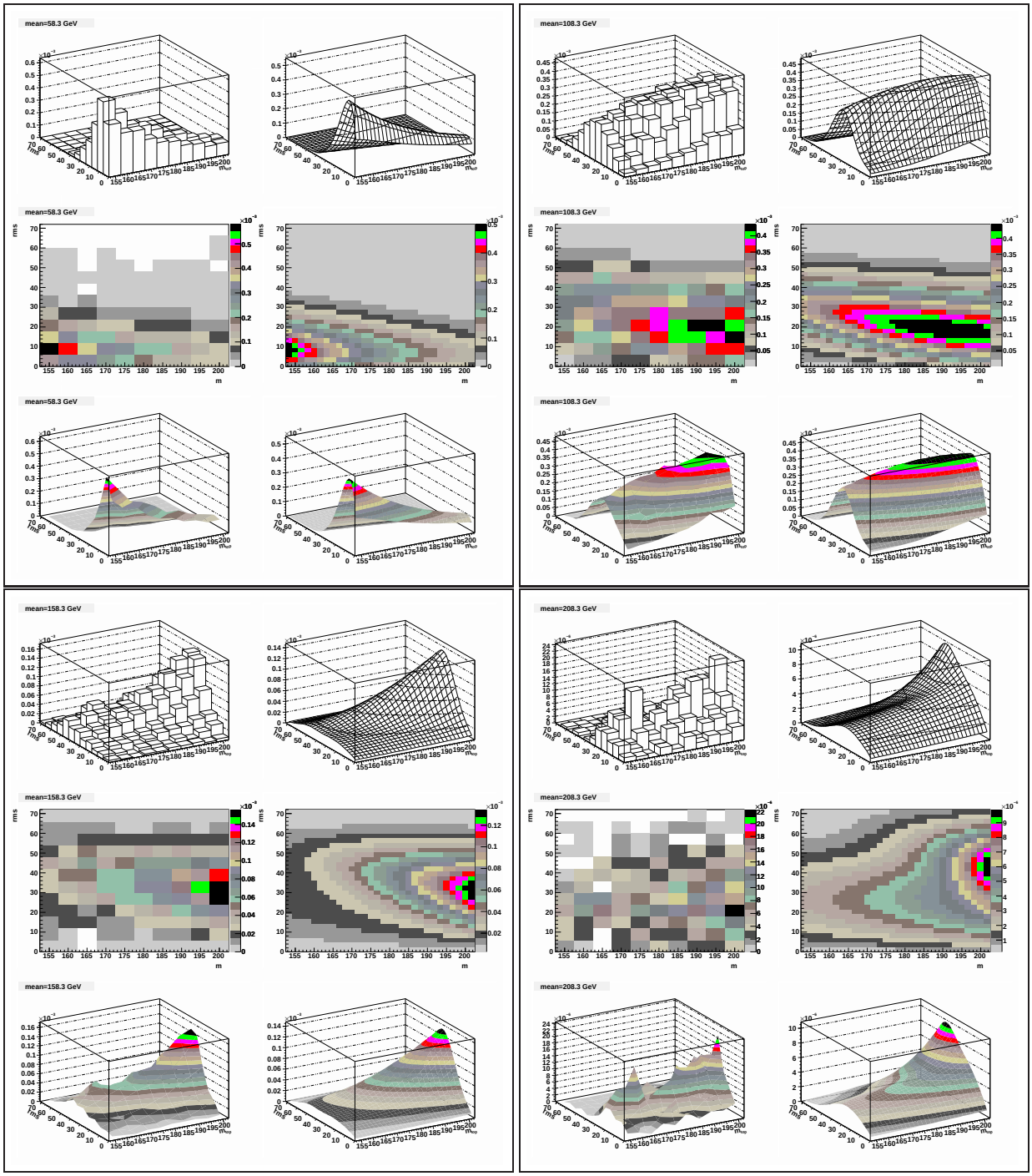

Figure C.2: $e\mu$: The first and third column show the histogram m_{top} vs. rms at a constant mean. The second and fourth column show the corresponding view of the 3d-fit result. mean = 58.3 GeV, 108.3 GeV, 158.3 GeV, and 208.3 GeV for the upper left, upper right, lower left, and lower right quarter, respectively.

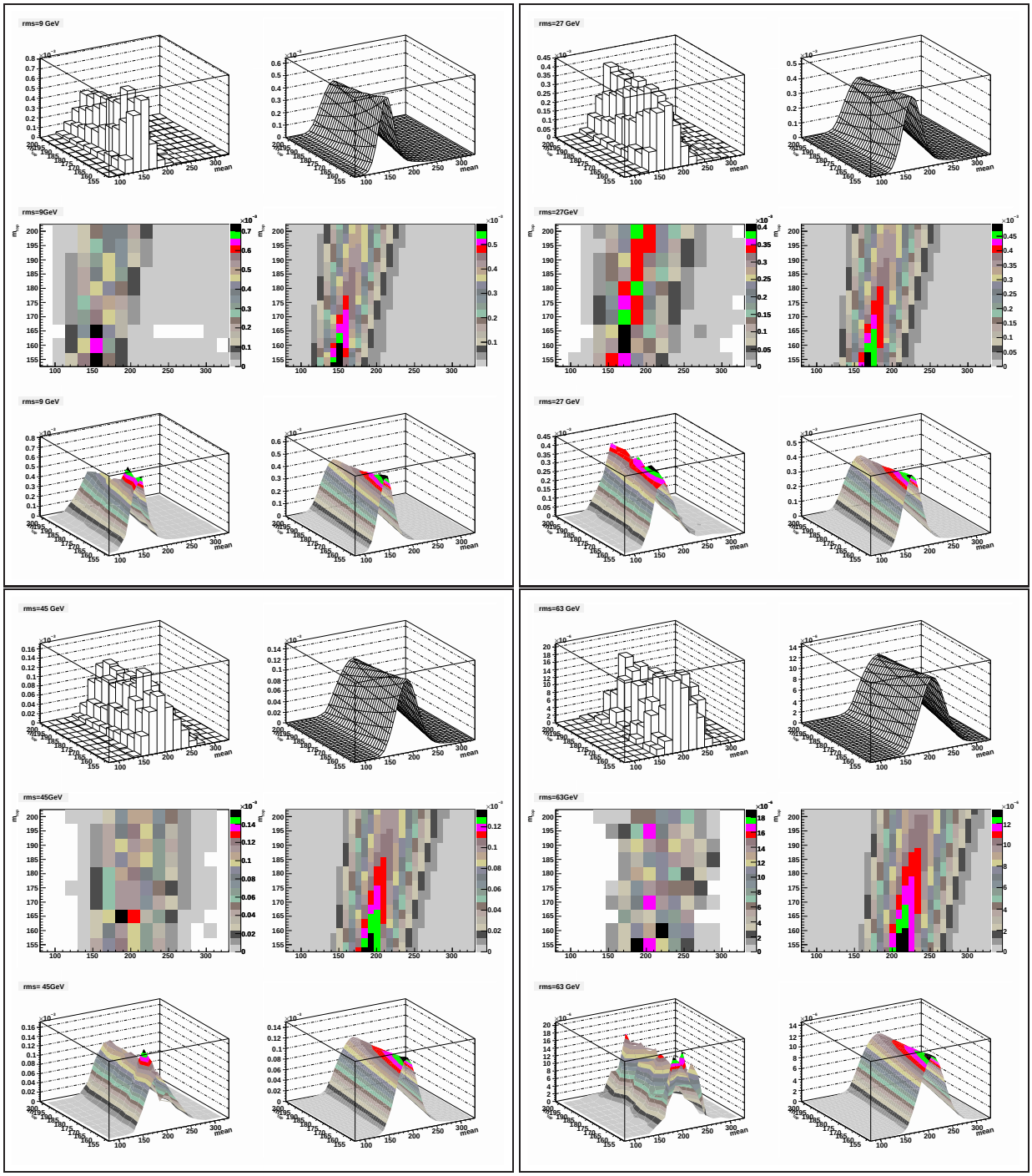

Figure C.3: $e\mu$: The first and third column show the histogram mean vs. m_{top} a constant rms. The second and fourth column show the corresponding view of the 3d-fit result. rms = 9 GeV, 27 GeV, 45 GeV, and 63 GeV for the upper left, upper right, lower left, and lower right quarter, respectively.

Appendix D

Signal Probability Density Function for the Dielectron Channel

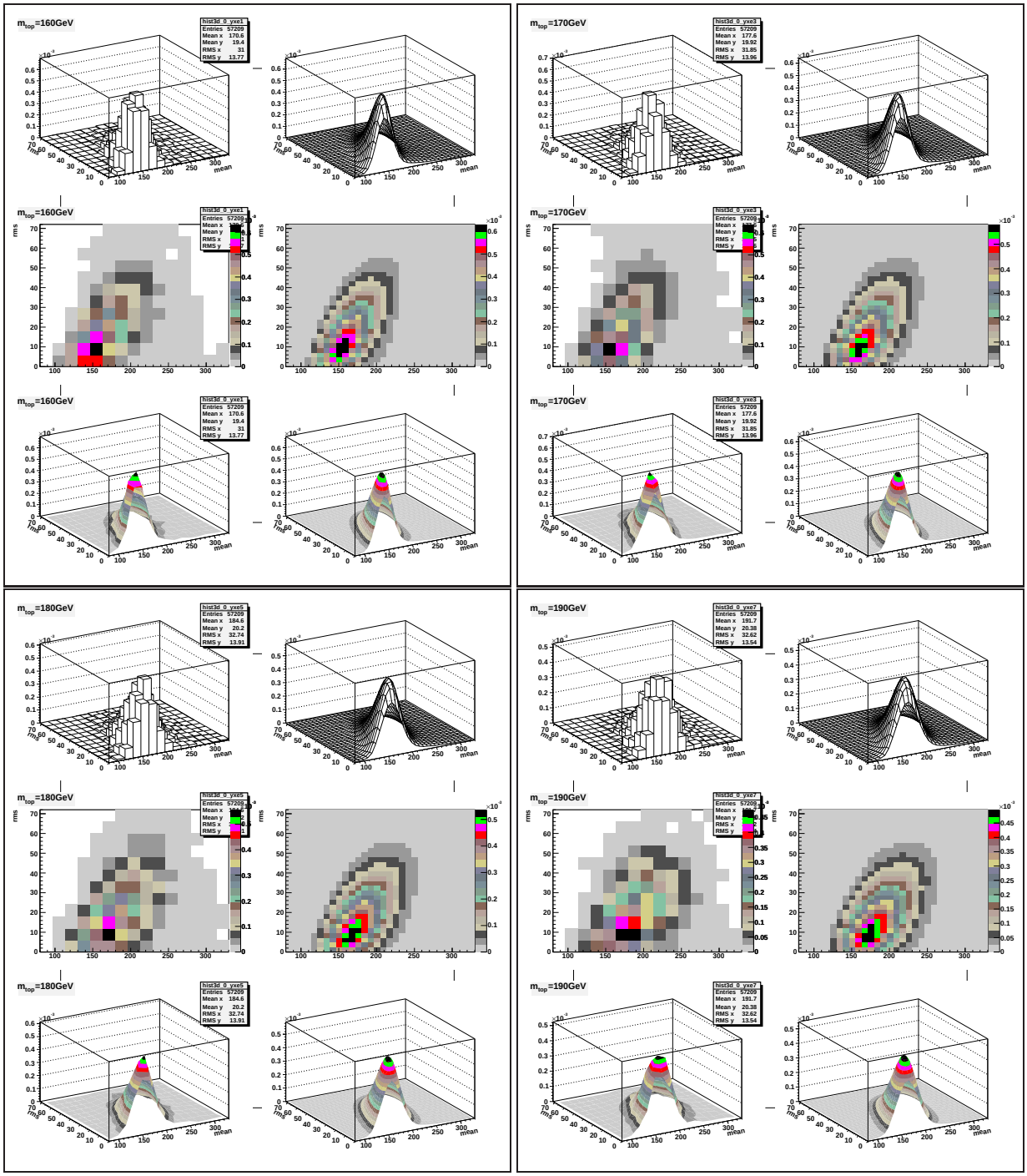

Figure D.1: *ee* : The first and third column show the histogram mean vs. rms at a constant m_{top}. The second and fourth column show the corresponding view of the 3d-fit result. m_{top} = 160 GeV, 170 GeV, 180 GeV, and 190 GeV for the upper left, upper right, lower left, and lower right quarter, respectively.

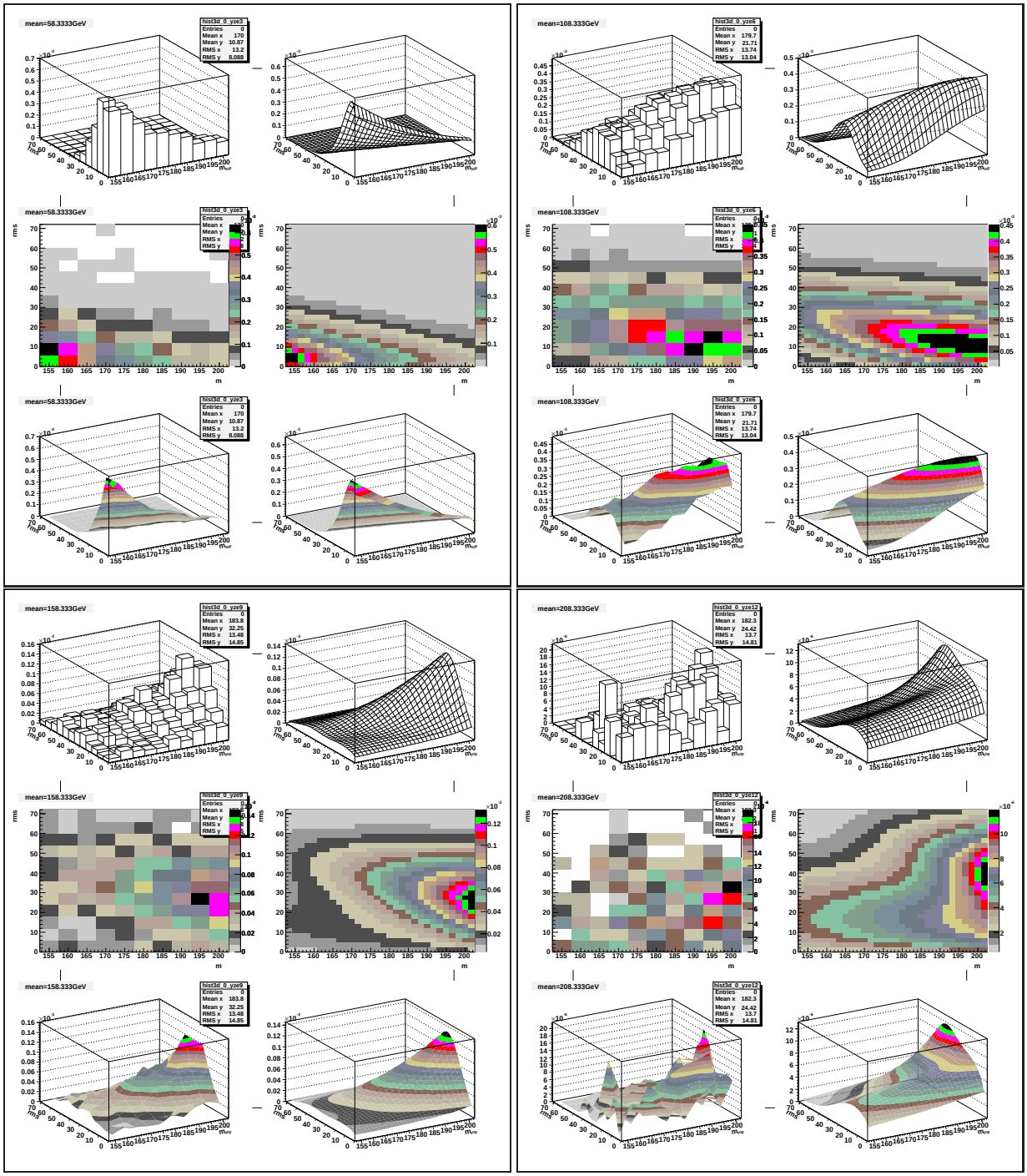

Figure D.2: *ee* : The first and third column show the histogram m_{top} vs. rms at a constant mean. The second and fourth column show the corresponding view of the 3d-fit result. mean = 58.3 GeV, 108.3 GeV, 158.3 GeV, and 208.3 GeV for the upper left, upper right, lower left, and lower right quarter, respectively.

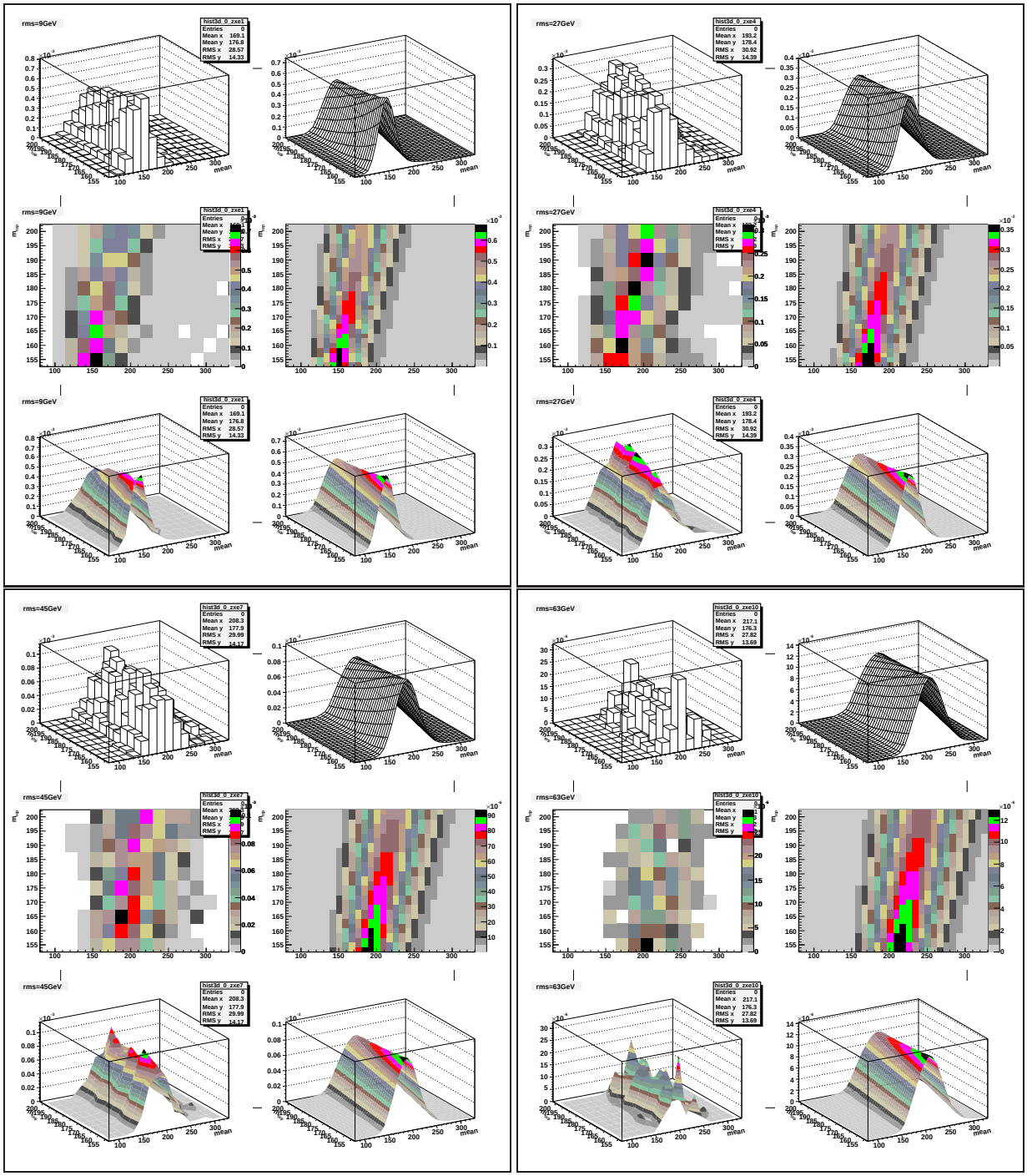

Figure D.3: *ee* : The first and third column show the histogram mean vs. m_{top} a constant rms. The second and fourth column show the corresponding view of the 3d-fit result. rms = 9 GeV, 27 GeV, 45 GeV, and 63 GeV for the upper left, upper right, lower left, and lower right quarter, respectively.

Appendix E

Signal Probability Density Function for the Dimuon Channel

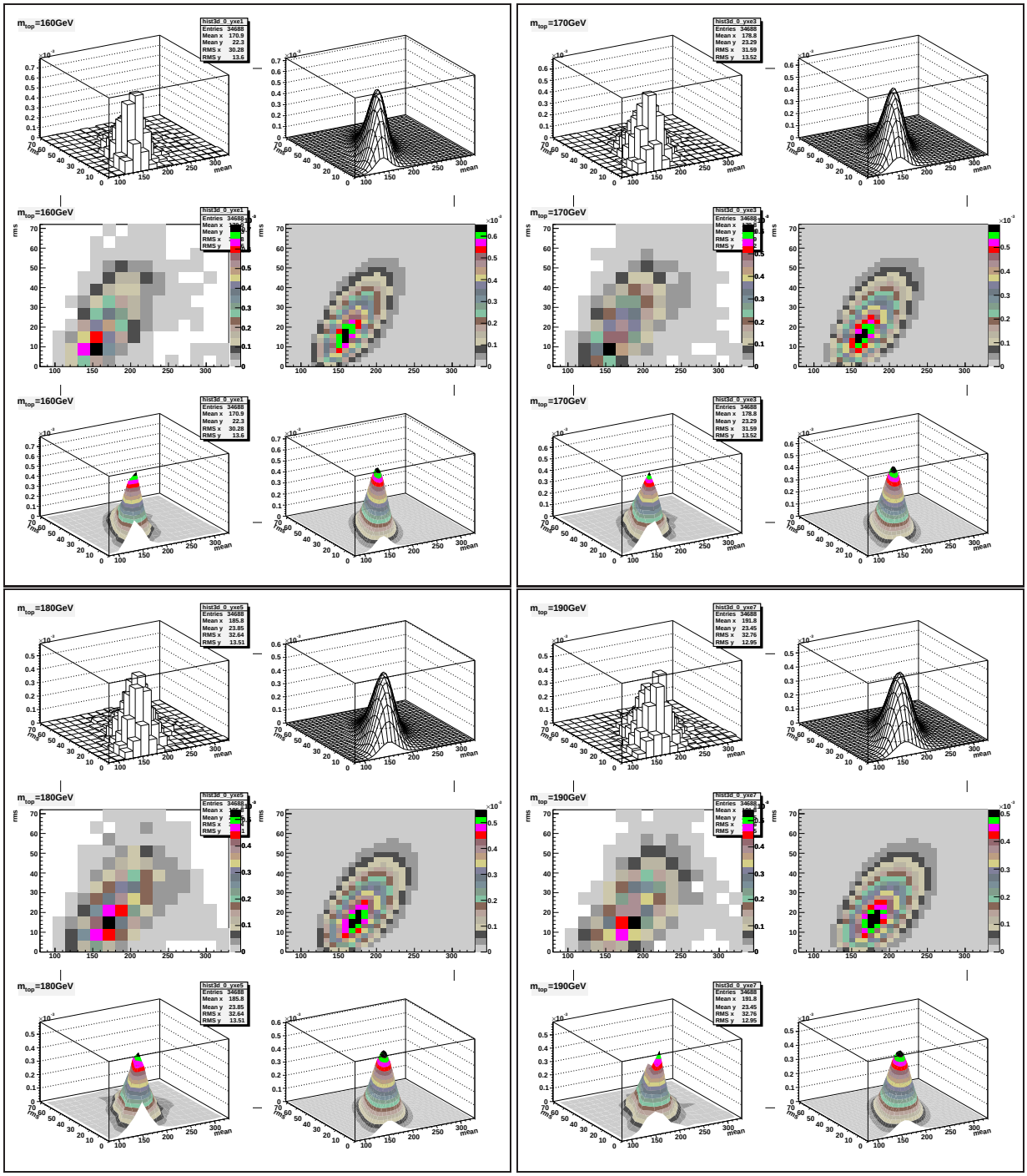

Figure E.1: $\mu\mu$: The first and third column show the histogram mean vs. rms at a constant m_{top}. The second and fourth column show the corresponding view of the 3d-fit result. m_{top} = 160 GeV, 170 GeV, 180 GeV, and 190 GeV for the upper left, upper right, lower left, and lower right quarter, respectively.

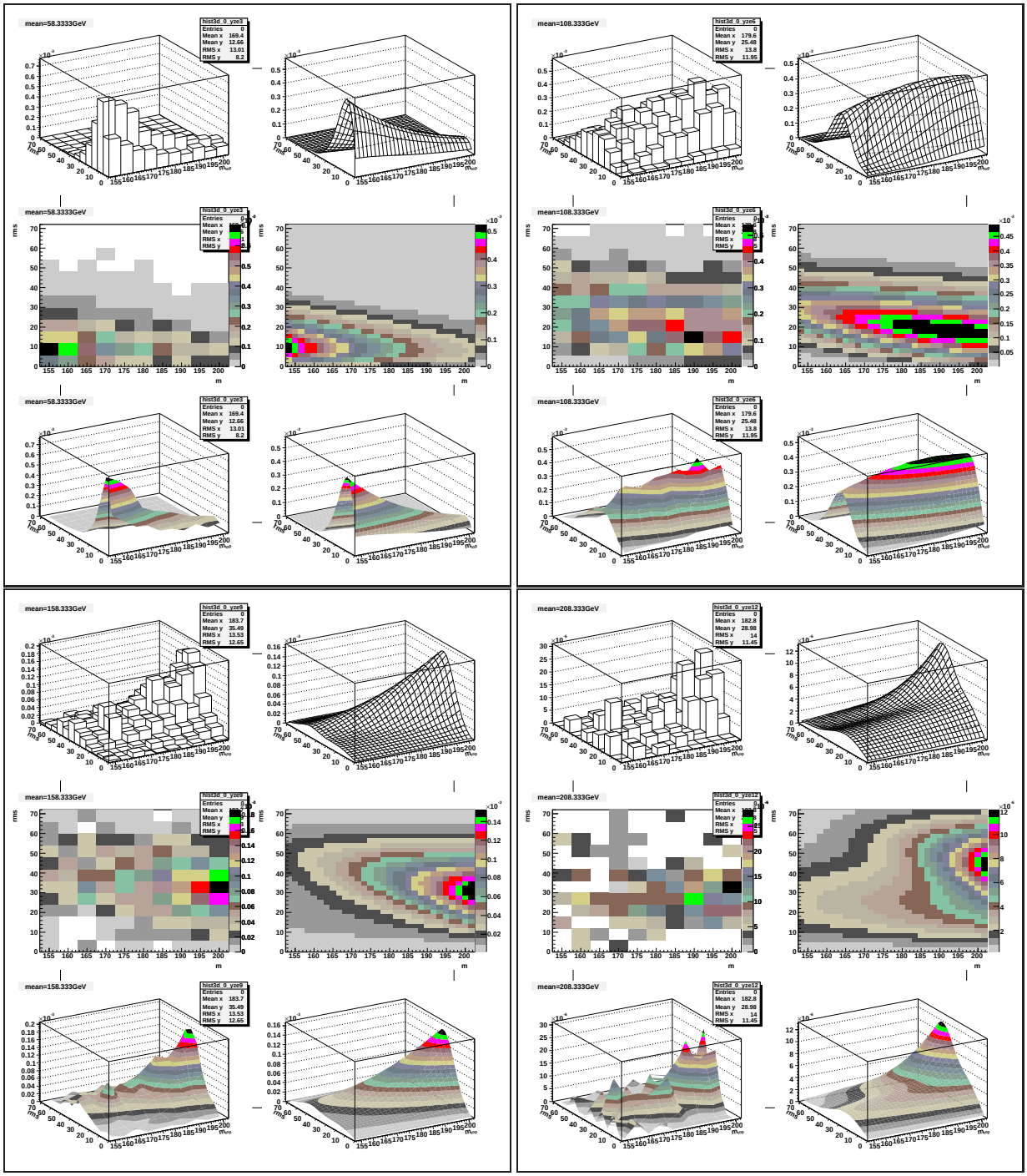

Figure E.2: $\mu\mu$: The first and third column show the histogram m_{top} vs. rms at a constant mean. The second and fourth column show the corresponding view of the 3d-fit result. mean = 58.3 GeV, 108.3 GeV, 158.3 GeV, and 208.3 GeV for the upper left, upper right, lower left, and lower right quarter, respectively.

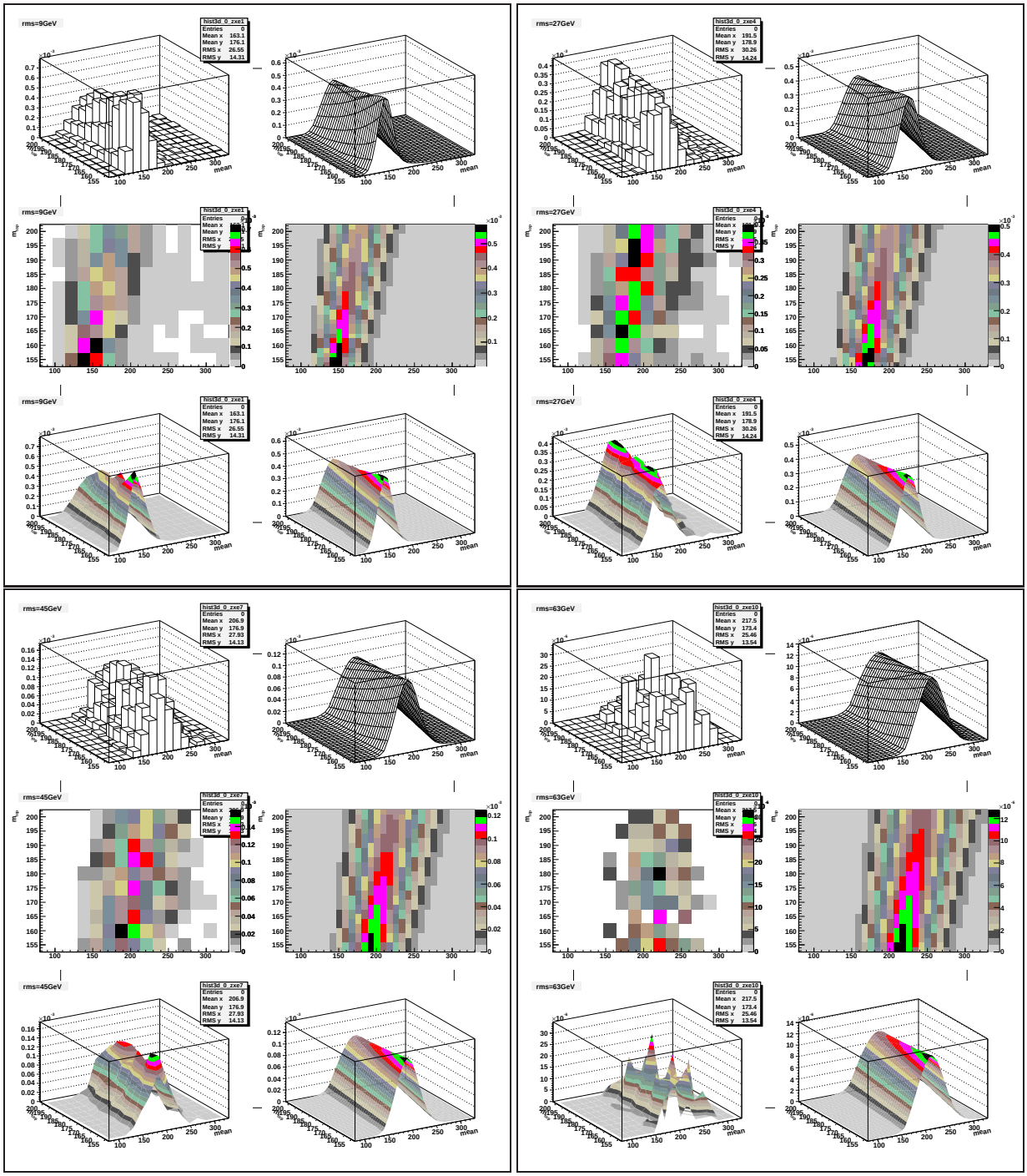

Figure E.3: $\mu\mu$: The first and third column show the histogram mean vs. m_{top} a constant rms. The second and fourth column show the corresponding view of the 3d-fit result. rms = 9 GeV, 27 GeV, 45 GeV, and 63 GeV for the upper left, upper right, lower left, and lower right quarter, respectively.

Bibliography

[1] S. L. Glashow, "Partial Symmetries of Weak Interactions," *Nucl. Phys.* **22** (1961) 579–588.

[2] S. Weinberg, "A Model of Leptons," *Phys. Rev. Lett.* **19** (1967) 1264–1266.

[3] A. Salam, "Elementary Particle Physics." N. Svartholm, ed., Nobel Symposium No. 8, Almqvist & Wiksell, Stockholm, 1968.

[4] P. W. Higgs, "Broken Symmetries, Massless Particles and Gauge Fields," *Phys. Lett.* **12** (1964) 132–133.

[5] F. Englert and R. Brout, "Broken Symmetry and the Mass of Gauge Vector Mesons," *Phys. Rev. Lett.* **13** (1964) 321–322.

[6] F. Halzen, A. D. Martin, *Quarks and Leptons: an Introductory Course in Modern Particle Physics*. Addison Wesley Press.

[7] G. 't Hooft and M. J. G. Veltman, "Scalar one loop integrals," *Nucl. Phys.* **B153** (1979) 365–401.

[8] J. C. Collins, D. E. Soper, and G. Sterman, "Heavy particle production in high-energy hadron collisions," *Nucl. Phys.* **B263** (1986) 37.

[9] **CDF** Collaboration, F. Abe *et al.*, "Observation of Top Quark Production in $p\bar{p}$ Collisions with the Collider Detector at Fermilab," *Phys. Rev. Lett.* **74** (1995) 2626–2631, `hep-ex/9503002`.

[10] **D0** Collaboration, S. Abachi *et al.*, "Observation of the Top Quark," *Phys. Rev. Lett.* **74** (1995) 2632–2637, `hep-ex/9503003`.

[11] **CDF** Collaboration, P. Azzi *et al.*, "Combination of CDF and D0 results on the top-quark mass," `hep-ex/0404010`.

[12] **CDF** Collaboration, "A combination of CDF and D0 results on the mass of the top quark," `hep-ex/0703034`.

[13] **D0** Collaboration, V. M. Abazov *et al.*, "Experimental discrimination between charge $2e/3$ top quark and charge 4e/3 exotic quark production scenarios," *Phys. Rev. Lett.* **98** (2007) 041801, `hep-ex/0608044`.

[14] S. Willenbrock, "Studying the Top Quark," *Rev. Mod. Phys.* **72** (2000) 1141–1148, hep-ph/0008189.

[15] N. Kidonakis and R. Vogt, "Next-to-next-to-leading order soft-gluon corrections in top quark hadroproduction," *Phys. Rev.* **D68** (2003) 114014, hep-ph/0308222.

[16] M. Cacciari, S. Frixione, M. L. Mangano, P. Nason, and G. Ridolfi, "The t anti-t cross-section at 1.8-tev and 1.96-tev: A study of the systematics due to parton densities and scale dependence," *JHEP* **04** (2004) 068, hep-ph/0303085.

[17] **D0** Collaboration, V. M. Abazov *et al.*, "Evidence for production of single top quarks and first direct measurement of |Vtb|," *Phys. Rev. Lett.* **98** (2007) 181802, hep-ex/0612052.

[18] N. Kidonakis, "Single top production at the tevatron: Threshold resummation and finite-order soft gluon corrections," *Phys. Rev.* **D74** (2006) 114012, hep-ph/0609287.

[19] W.-M. *et al.*. Yao, "Review of Particle Physics," *Journal of Physics G* **33** (2006) 1+.

[20] M. J. G. Veltman, "Second Threshold in Weak Interactions," *Acta Phys. Polon.* **B8** (1977) 475.

[21] **LEP** Collaboration, "Electroweak Parameters of the Z0 Resonance and the Standard Model: the LEP Collaborations," *Phys. Lett.* **B276** (1992) 247–253.

[22] The ALEPH, DELPHI, L3, OPAL and SLD Collaborations, the LEP-Electroweak Working Group, the SLD Electroweak and Heavy Flavour Groups, "A Combination of Preliminary Electroweak Measurements and Constraints on the Standard Model," *updated for the Winter 2007 conferences,* http://www.cern.ch/LEPEWWG (2007).

[23] **LEP Working Group for Higgs boson searches** Collaboration, R. Barate *et al.*, "Search for the standard model higgs boson at lep," *Phys. Lett.* **B565** (2003) 61–75, hep-ex/0306033.

[24] H. P. Nilles, "Supersymmetry, supergravity and particle physics," *Phys. Rept.* **110** (1984) 1.

[25] G. L. Kane and S. Mrenna, "Do about half the top quarks at fnal come from gluino decays?," *Phys. Rev. Lett.* **77** (1996) 3502–3505, hep-ph/9605351.

[26] F. B. Division, "RunII Handbook." Fermilab Beams Division RunII Webpage, http://www-bd.fnal.gov/runII/index.html.

[27] Fermilab Accelarator Division, http://www-bd.fnal.gov/pplot/index.html.

[28] **D0** Collaboration, V. A. *et al.*, "The Upgraded DØ Detector," *Nucl. Instrum. Methods Phys. Res. A* **565** (2006) 463, `physics/0507191`.

[29] K. Hanagaki, "D0 layer 0 innermost layer of silicon microstrip tracker," *Nucl. Instrum. Meth.* **A569** (2006) 8–11.

[30] **D0** Collaboration, S. Abachi *et al.*, "Beam tests of the D0 uranium liquid argon end calorimeters," *Nucl. Instrum. Meth.* **A324** (1993) 53–76.

[31] **D0** Collaboration, B. Abbott *et al.*, "A measurement of the w boson mass," *Phys. Rev.* **D58** (1998) 092003, `hep-ex/9712029`.

[32] P. Calfayan *et al.*, "Muon Identification Certification for `p17` data." DØ-Note 5157, June, 2006.

[33] Sjöstrand, Torbjörn and others, "PYTHIA 6.2 Physics and Manual," *Comp. Phys. Comm.* **135** (2001) 238, `hep-ph/0108264`.

[34] M. L. Mangano, M. Moretti, F. Piccinini, R. Pittau, and A. D. Polosa, "ALPGEN, a Generator for Hard Multiparton Processes in Hadronic Collisions," *JHEP* **07** (2003) 001, `hep-ph/0206293`.

[35] M. L. Mangano and others *Nucl. Phys. B* **632** (2002) 343–362, `hep-ph/0108069`.

[36] T. Sjöstrand, "High-Energy Physics Event Generation with PYTHIA 5.7 and JETSET 7.4," *Comp. Phys. Comm.* **82** (1994) 74.

[37] W. J. Fisyak Y., "D0gstar D0 GEANT Simulation of the Total Apparatus Response." DØ-Note 3191, April, 1997.

[38] R. Brun and others, "GEANT – Detector Description and Simulation Tool," *CERN Program Library Vers. 3.21* **W5013** (1993).

[39] S. Eno *et al.*, "Status of the Fast Simulatin PMCS, v01-96-00." DØ-Note 4097, February, 2003.

[40] DØ Monte Carlo Production Group, "PMCS Documentation," `http://www-d0.fnal.gov/computing/MonteCarlo/pmcs/pmcs_doc/pmcs.html`.

[41] Common Sample Group, http://www-d0.fnal.gov/Run2Physics/cs/.

[42] R. Brun, F. Rademakers, and S. Panacek, "Root, an object oriented data analysis framework,". Prepared for CERN School of Computing (CSC 2000), Marathon, Greece, 17-30 Sep 2000.

[43] M. Wetstein, J. Stark, and M. Verzocchi, "Gain Calibration for the EM Calorimeter in Run II." DØ-Note 5004, September, 2006.

[44] A. Baranovski *et al.*, "The sam-grid project: Architecture and plan," *Nucl. Instrum. Meth.* **A502** (2003) 423–425.

[45] Condor, http://www.cs.wisc.edu/condor/.

[46] Globus, http://www.globus.org.

[47] SAM project, http://d0db.fnal.gov/sam/.

[48] Grid Computing Center Karlsruhe (GridKa), http://grid.fzk.de/.

[49] G. C. Blazey *et al.*, "Run ii jet physics," `hep-ex/0005012`.

[50] G. Blazey *et al.*, "Run II Jet Physics." DØ-Note 3750, April, 2002.

[51] A. Harel, "Jet ID Optimization." DØ-Note 4919, September, 2005.

[52] A. Harel and W. Robert, "Improved L1 Confirmation." DØ-Note 4932, September, 2005.

[53] Nikola Makovec, Jean-François Grivaz, "Shifting, Smearing, and Removing Simulated Jets." DØ-Note 4914, August, 2005.

[54] Hays, J. *et al.*, "Electron Likelihood Study." DØ-Note 4769, March, 2005.

[55] Hays, J. *et al.*, "Single Electron Efficiencies in p17 Data and Monte-Carlo Using d0correct from Release p18.05.00." DØ-Note 5105, May, 2006.

[56] Raja, R. *et al.*, "Reconstruction and Analysis: Tracking Packages, CalorimeterPackages." DØ-Note 1006, July, 1990.

[57] Raja, R., "H Matrix anlaysis of top → lepton + jets – McPhysics Workshop II." DØ-Note 1192, September, 1991.

[58] S. Trincaz-Duvoid and P. Verdier, "Missing ET Reconstruction in p17." DØ-Note 4474, June, 2004.

[59] M. Arthaud, M. Besancon, S. Chakrabarti, F. Deliot, E. Shabalina, and V. Sharyy, "Measurement of the ttbar Production Cross-section at sqrts=1.96 TeV in Electron Muon Final States using p17 data set." DØ-Note 5360, March, 2007.

[60] B. Martin, Y. Arnoud, G. Sajot, and E. Shabalina, "Measurement of the ttbar production cross section at sqrt(s)= 1.96 TeV in the ee final state using p17 data set." DØ-Note 5386, April, 2007.

[61] U. Bassler, J. Konrath, and C. Schwanenberger, "Measurement of the ttbar Production Cross-section at sqrt(s)=1.96 TeV in the Dimuon Final State Using p17 Data Set." DØ-Note 5350, February, 2007.

[62] **D0** Collaboration, B. Abbott *et al.*, "Measurement of the top quark mass using dilepton events. dø collaboration," *Phys. Rev. Lett.* **80** (1998) 2063–2068, `hep-ex/9706014`.

[63] **D0** Collaboration, B. Abbott *et al.*, "Measurement of the top quark mass in the dilepton channel," *Phys. Rev.* **D60** (1999) 052001, `hep-ex/9808029`.

[64] E. W. Varnes, "Measurement of the top quark mass,". FERMILAB-THESIS-1997-28.

[65] P. Schieferdecker and M. Wang, "Jet Transfer Functions derived from p17 ttbar Monte Carlo." DØ-Note 5136, March, 2006.

[66] L. Wang, S. Eno, M. Sanders, and J. Zhu, "Measurement of Z boson transverse momentum at $\sqrt{s}$=1.96 TeV." DØ-Note 5187, July, 2006.

[67] P. Haefner and F. Fiedler, "Muon transfer function parameters for p17 MC." DØ-Note 5214, August, 2006.

[68] O. Brandt, R. Kehoe, J. Meyer, A. Quadt, P. Renkel, and C. Schwanenberger, "Measurement of the Top Quark Mass in Dilepton Events with Neutrino Weighting." DØ-Note 5346, February, 2007.

[69] O. Brandt, R. Kehoe, J. Meyer, A. Quadt, P. Renkel, C. Schwanenberger, and J. Temple, "Measurement of m_top in e-mu Events with Neutrino Weighting." DØ-Note 5162, June, 2006.

[70] L. Holmström, S. R. Sain, H. E. Miettinen,, "A New Multivariate Technique for Top Quark Search," *Comput. Phys. Commun.* **88** (1995) 195–210.

[71] O. Brandt, "Measurement of the mass of the top quark in dilepton final states with the D0 detector,". FERMILAB-MASTERS-2006-03.

[72] K. S. Cranmer, "Kernel estimation in high-energy physics," *Comput. Phys. Commun.* **136** (2001) 198–207, `hep-ex/0011057`.

[73] R. Barlow, *Statistics: a Guide to the Use of Statistical Methods in the Physical Sciences*. The Manchester Physics Series, New York, Wiley, 1989.

[74] F. James and M. Roos, "Minuit: A system for function minimization and analysis of the parameter errors and correlations," *Comput. Phys. Commun.* **10** (1975) 343–367.

[75] R. Barlow, "SLUO Lectures on Statistics and Numerical Methods in HEP, Lecture 6: Resampling and the Bootstrap." http://www.hep.man.ac.uk/u/roger/sluo6.ps, August, 2000.

[76] J. Kozminski, *Measurement of the Top Quark Mass in Dilepton Events Using Neutrino Constraints*. Ph.D. thesis, Michigan State University, 2005.

[77] J. W. Temple, "Measurement of m_{top} via neutrino weighting in the dilepton decay channels at D0,". UMI-32-37809.

[78] **D0** Collaboration, V. M. Abazov *et al.*, "Measurement of the top quark mass in the dilepton channel," `hep-ex/0609056`.

[79] S. Anderson, R. Kehoe, J. Kozminski, J. Meyer, A. Quadt, P. Renkel, and C. Schwanenberger, "Measurement of m_top in Dilepton Events with Neutrino Weighting." DØ-Note 5047-CONF, March, 2006.

[80] J. Group, "Jet Energy Scale Determination at D0 Run II (final p17 version)." DØ-Note 5382, 2007.

[81] L. Lyons, D. Gibaut, and P. Clifford, "How to combine correlated estimates of a single physical quantity," *Nucl. Instrum. Meth.* **A270** (1988) 110.

[82] A. Valassi, "Combining correlated measurements of several different physical quantities," *Nucl. Instrum. Meth.* **A500** (2003) 391–405.